

# **Integration of Solution Processed Novel Graphenaceous Materials as Functional Layers in Dye Sensitized and Polymer Solar Cells**

*A thesis submitted by*

**Nagavolu Charanadhar**

*in the partial fulfilment of the requirement for the award of the degree of*

**Doctor of Philosophy**

*in*

**Nano Science and Technology**

*Under the supervision of*

**Dr.-Ing. V. V. S. S. Srikanth**



School of Engineering Sciences and Technology  
University of Hyderabad  
Central University (P.O.)  
Hyderabad 500046  
India

**April 2019**

---

## **Declaration**

I, **Nagavolu Charanadhar**, declare that this thesis work entitled “**Integration of Solution Processed Novel Graphenaceous Materials as Functional Layers in Dye Sensitized and Polymer Solar Cells**”, submitted in partial fulfillment of the requirement for the award of **Doctor of Philosophy (in Nano Science and Technology)** in the School of Engineering Sciences and Technology, University of Hyderabad is completely my own work except for those referenced. This work was done under the supervision of **Dr.-Ing. V. V. S. S. Srikanth**. This report is a record of the bonafide research work carried out by me and the results incorporated in it have not been reproduced/copied from any source. This work has not been submitted to any other University or Institution for the award of any other degree or equivalent.

**Nagavolu Charanadhar**

Reg. No.: 11ENPT01

School of Engineering Sciences and Technology

University of Hyderabad



## **CERTIFICATE**

This is to certify that the thesis entitled Integration of Solution Processed Novel Graphenaceous Materials as Functional Layers in Dye Sensitized and Polymer Solar Cells Submitted by Nagavolu Charanadhar bearing registration number 11ENPT01 (Int. M.Tech./Ph.D. (Nano Science and Technology)) in partial fulfillment of the requirements for award of Doctor of Philosophy in the School of Engineering Sciences and Technology is a bonafide work carried out by him under my supervision and guidance.

This thesis is free from plagiarism and has not been submitted previously in part or in full to this or any other University or Institution for award of any degree or diploma.

Parts of this thesis have been:

A. published in the following publications:

1. *Solar Energy* 137, 143-147 (2016) (ISSN: 0038-092X)
2. *Bulletin of Materials Science* 41:62, 1-19 (2018) (ISSN number: 0250-4707)

and

B. presented in the following conferences:

1. *Symposium on frontiers in Nanoscience and Technology -2018 (National)*
2. *NMEA-2017 (National)*
3. *STS Forum - 2016 (International)*
4. *AEM - 2016 (International)*

Further, the student has passed the following courses towards fulfilment of coursework requirement for Ph.D.

Course Code	Name	Credits	Pass/Fail
MT601	Research Methodology	4	Pass

and was exempted from doing coursework (recommended by Doctoral Committee) on the basis of the following courses passed during his M.Tech. program (in Int. M.Tech./Ph.D. program) and the M.Tech. degree was awarded:

Course Code	Name	Credits	Pass/Fail
NT401	Thermodynamics and Phase Equilibria	4	Pass
NT402	Concepts of Materials Science	4	Pass
NT403	Characterization of Materials	4	Pass
NT404	Seminar	2	Pass
NT405	Advanced Engineering Mathematics	2	Pass
NT406	Materials Processing and Characterization Laboratory	4	Pass
NT407	Concepts of Nano Science and Technology	4	Pass
NT408	Synthesis and Applications of Nanomaterials	4	Pass
NT451	Nano Biotechnology	4	Pass
NT452	Mechanical Behavior of Nanomaterials	4	Pass
NT453	Modeling and Simulation	4	Pass
NT454	MEMS AND NEMS Nanofabrication Technologies	4	Pass
NT455	Surface Engineering	4	Pass
NT456	Polymer Science and Technology	2	Pass
NT457	Laboratory	4	Pass
NT458	Seminar	2	Pass
NT550	Dissertation	18	Pass

**Supervisor**

**Dean of School**

---

## **Acknowledgements**

I would like to express my special thanks to my project supervisor Dr.-Ing. Vadali V. V. S. Srikanth for giving me an opportunity to work with him. I appreciate his encouragement, guidance and the constant support he has provided throughout the course of my research work. I have learned a lot from his suggestions, comments and discussions. Special thanks to my DRC members Prof. M Ghanashyam Krishna and Dr. Koteswararao V. Rajulapati for their valuable suggestions during my doctoral committee meetings. I would also like to take this opportunity to sincerely thank Prof. Ravi Silva for providing lab facilities and guidance in carrying out experiments under DST-UKIERI project at University of Surrey. I thank DST for providing fellowship and travel expenses under DST-UKIERI project to travel to Surrey to carry out experiments. I would like to express my gratitude to the present Dean and past Deans, faculty members, office staff, and lab assistants of School of Engineering Sciences and Technology, University of Hyderabad for their support. I am also thankful to Dr. Ahamed, and Mr. Muvva D Prasad for helping me in carrying out Raman spectroscopy and transmission electron microscopy experiments, respectively. This work and my education would have been the way it is without the moral support and love of family members, whom I sincerely acknowledge.

**Nagavolu Charanadhar**

---

# Table of Contents

<b>Abstract</b> .....	iii
<b>Chapter 1 Introduction</b> .....	5
<b>1.1 General Background</b> .....	5
<b>1.2 Importance of New Solar PV Technologies</b> .....	8
<b>1.3 Problem Definition</b> .....	8
<b>1.4 Overview of the Thesis</b> .....	10
<b>Chapter 2 Literature Review</b> .....	11
<b>2.1 Current Status of the Solar PV Technology</b> .....	11
<b>2.2 Materials for Solar PV Technology</b> .....	12
2.2.1 <i>Materials in conventional Si-based solar cells</i> .....	13
2.2.2 <i>Materials in thin films-based solar cells</i> .....	15
2.2.3 <i>Nano- materials and science in solar PV technology</i> .....	18
<b>2.3 Development of Fundamentals</b> .....	19
2.3.1 <i>Dye sensitized solar cells</i> .....	19
2.3.2 <i>Organic photovoltaic</i> .....	20
2.3.3 <i>Electrical characteristics of PV devices</i> .....	25
2.3.4 <i>Interfacial layers for OPV devices</i> .....	33
<b>2.4 Device Architectures</b> .....	38
2.4.1 <i>DSSC architecture</i> .....	38
2.4.2 <i>OPV device architecture</i> .....	39
<b>2.5 Graphenaceous Materials as Counter Electrodes in DSSC</b> .....	40
<b>2.6 Graphenaceous Materials as Electron Transport Layers in OPV Devices</b> .....	43
<b>Chapter 3 Experimental Procedure</b> .....	50
<b>3.1 Synthesis of Graphenaceous Materials</b> .....	50
<b>3.2 Deposition of Active Layers</b> .....	52
3.2.1 <i>Spray coating</i> .....	52
3.2.2 <i>Spin coating</i> .....	53
3.2.3 <i>Vacuum-thermal evaporation technique</i> .....	53
<b>3.3 Fabrication of DSSC Device</b> .....	53
3.3.1 <i>Preparation of nanocrystalline TiO<sub>2</sub> photo-anode</i> .....	53
3.3.2 <i>Fabrication of GO and SRGO counter electrodes</i> .....	54

---

3.3.3 <i>Fabrication of the device</i> .....	55
<b>3.4 Fabrication of OPV devices</b> .....	55
<b>3.5 Characterization of Materials</b> .....	56
<b>3.6 Device Characterization and Testing</b> .....	57
3.6.1 <i>Electrochemical characterization of DSSC devices</i> .....	57
3.6.2 <i>I-V characteristics of the solar cells</i> .....	57
3.6.3 <i>External quantum efficiency of OPV devices</i> .....	58
<b>Chapter 4 Results and Discussion</b> .....	59
<b>4.1 Morphology and Composition of Graphenaceous Materials</b> .....	59
<b>4.2 Electrochemical Analysis of DSSC Devices</b> .....	62
<b>4.3 Photovoltaic Performance of DSSC Devices</b> .....	64
<b>4.4 Photovoltaic Performance of OPV Devices</b> .....	65
<b>Chapter 5 Conclusions and Future Aspects</b> .....	75
<b>5.1 Conclusions</b> .....	75
<b>5.2 Future Aspects</b> .....	75
<b>References</b> .....	77
<b>Appendix 1</b> .....	97
<b>Appendix 2</b> .....	98
<b>Appendix 3</b> .....	99
<b>Appendix 4</b> .....	100

---

## Abstract

Harnessing renewable solar energy through different technologies is greatly dependent on the advancement of solar grade materials' science and engineering. Worldwide, scientists and engineers are focusing on developing novel solar cell designs which can be easily manufactured at low cost. In this context, 3<sup>rd</sup> generation (3G) solar energy technologies namely Gratzel cells or Dye Sensitized Solar Cells (DSSCs) and Bulk heterojunction organic photovoltaics (BHJ OPV) are expected to challenge the performance of Si based solar cells and compete for a significant market share in the field of next generation solar cells. These technologies gained prominence due to their low cost, light weight construction and printable nature over large area flexible substrates. This thesis work demonstrates an integration of inexpensive novel Graphenaceous Materials solution, for the above mentioned solar technologies energy harvesting, explore selection of suitable material for their energy efficient utilization and fabrication method. Initially, Graphene oxide (GO) was synthesized using a modified Hummers method and was reduced by using focused sunlight to obtain solar reduced graphene oxide (SRGO). GO and SRGO are then used as Pt free counter electrode materials in dye sensitized solar cells (DSSCs). GO and SRGO counter electrodes were prepared by a simple spray coating method to produce homogeneous electrode layers. The DSSCs with GO and SRGO counter electrodes exhibited an overall power conversion efficiencies of ~3.4 and ~4%, respectively. Cyclic voltammetry and electrochemical impedance spectroscopy reveal that the DSSC with SRGO counter electrode exhibits higher electro-catalytic activity and lower charge transfer resistance at the electrode/electrolyte interface (in comparison to the DSSC with GO) resulting in higher conversion efficiency. Moreover, the microstructural features of SRGO are found to be suitable for its improved interaction with the liquid electrolyte and the enhanced electro-catalytic activity at its surface.

---

A BHJ OPV typically consists of a blend of two polymers, consisting of an electron donating conjugated polymer and functionalized nano-sized carbon allotrope molecule as an electron acceptor. Generation of the excitons and their subsequent dissociation takes place at the donor–acceptor interface when light shines on the BHJ blend. To facilitate transport of these dissociated free charges towards the contacts, and to generate useful power by extracting these charges at the contacts, interfacial layers are an important components in OPV structure. These interfacial layers significantly enhance device performance, mainly due to their selective charge extraction nature to transport charge to the contacts. In this work, six different Reduced Graphene oxide (RGO) derived materials are used as electron transport layers, for improving charge extraction in the OPV, and their performance compared. An efficiency around 7% is obtained for the PCDTBT/PC<sub>70</sub>BM devices over relatively large areas upon optimization.

### Chapter 1 Introduction

#### 1.1 General Background

At present, harnessing ‘renewable energy’ is one of the most sought-after objectives in the world. Ever increasing worldwide energy demand for terrestrial applications is going to deplete the conventional energy resources in a very short time [1][2]. In order to challenge and meet the growing demand particularly in some of the emerging and developing countries where per capita energy availability is less than needed for quality life—scientists, engineers and technologists have been developing economically viable and sustainable energy solutions, which offer clean, continuous and reliable energy on a large-scale [3]. In this context, recently, a wide-ranging plan named ‘Wind, Water and Solar (WWS)’ power has been outlined [4]. WWS power plan does not involve the use of any non-renewable energy resources. Owing to the exponential increase in technology, it is anticipated that by 2030, WWS power would satisfy all the energy demands in the world and by 2050, all contemporary energy resources could be appropriately transformed to WWS power. However, it was discerned that the only constraints for the proper implementation of WWS power plan would be of only social and political nature. It was also discerned that the energy costs in the WWS powered world would be similar to that of the present day’s energy costs.

Energy Information Administration (EIA), U.S. Department of Energy and International Energy Outlook, has projected that by 2030, the entire world requires a total usable power of  $\sim 17$  TW. However, such a requirement cannot be met with the depleting fossil fuels and hence it was recognized that the WWS power systems are the only means to supply sustainable energy. Amongst all the identified WWS technologies such as wind, wave, geothermal, hydroelectric, tidal, concentrated solar power (CSP) and solar photovoltaic (PV) technologies, solar PV technology was found to be the dominant one, owing to obvious advantages it brings-in. The primary advantage is in the incidence of solar radiation equivalent to  $\sim 6500$  TW on the land and ocean surfaces together [5]. Practically, a total terrestrial solar power of  $\sim 340$  TW (which is  $\sim 20$  times greater than the required end-use power) is deliverable using solar PV technology alone [5]. Furthermore, other WWS technologies can be set-up at places where wind, wave and hydrothermal sources are abundant as compared to the solar radiation to supplement solar PV energy supply. It is worth mentioning that as solar PV technology advances, the energy costs decrease, which is another pertinent advantage.

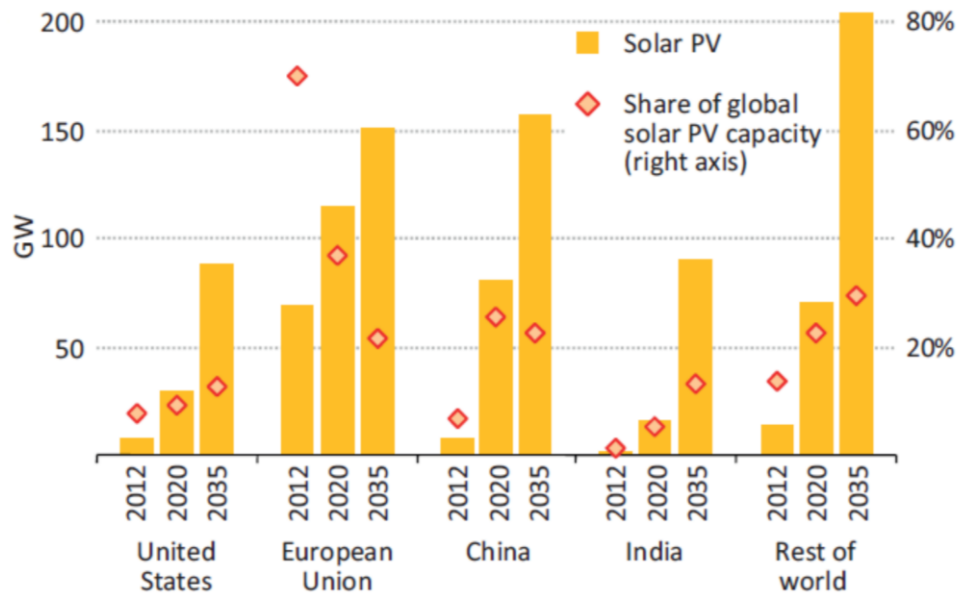


**Figure 1.1: Installed solar PV capacity by region in 2035. The need for electricity worldwide leads to an electricity production of 950 TWh in 2035 [6].**

The world population is constantly increasing. With current growth rate of around 1.14% per year, it is expected to rise from 7 billion in 2011 to 8 billion people in 2024 [7]. Added to improving standards of life in developing countries, the world demand for electricity will increase by up to two-thirds by 2035. According to the “World Energy Outlook 2013” published by the “International Energy Agency” (IEA), fossil fuels currently remain the main energy sources for exploitation. However, the share of oil, gas and coal in the global energy mix is expected to decrease from 68% in 2011 to 57% by 2035. On the other hand, the share of renewables as a power generation source will rise from 20% in 2011 to 31% in 2035 and will approach coal as the leading energy source by 2035 [6]. Furthermore, renewables are becoming more competitive due to reducing CO<sub>2</sub> emissions and enhancing energy security while encouraging economic development. As a consequence, a rapid expansion of renewable power, generated using solar photovoltaics (PV) systems, has been observed. The worldwide total installed capacity of solar PV increased by 43% in 2013 and is expected to reach 690 GW in 2035 as depicted in Fig. 1.1.

Given the requirement for sustainable energy solutions, PV systems have been recognized by many countries. For instance, Germany dedicated 22.9 B to the construction of renewable energy plants in 2011; 15.0 B in the solar energy sector [3]. However, investments in the PV sector are mainly spent on development of solar cells made of inorganic materials such as silicon. Depending on the type of silicon, efficiencies between 10.1% and 25% can be obtained (for amorphous and crystalline silicon, respectively) [4]. However, the fabrication process of

## Introduction

---

silicon PV is complex and energy consuming leading to expensive solar panels compared to energy sources from fossil fuels like coal, natural gas and hydro power, etc. Furthermore, the fabrication process limits the silicon solar cells size and thus, no large area silicon solar cell can be easily processed [5].

As a result, research in to alternative materials for solar energy harvesting has been carried over the past decades. The first report on an polymer solar cell (PSC) was made in 1959, but the reported device efficiency was extremely low [7]. It took more than 25 years before the first organic photovoltaics (OPV) solar cell with efficiency approaching 1% was reported [6]. Since then, extensive study has been dedicated to research on this field and nowadays the OPV technology is seen as one of the most promising future solar PV technologies, being expected to become a key player of the energy market in the coming years [8]. This belief is supported by various advantages of the organic PV over their inorganic counterparts. The organic solar cell (OSC) fabrication can be accomplished at temperatures below 150°C, much lower than usual fabrication temperatures for inorganic solar cells. These low fabrication temperatures allow the utilization of cheap organic semiconductors, which are also solution processable. Indeed, the first completely solution processed OSC was reported in 1995 by Yu et al [9]. Furthermore, the solution processability at low temperatures enables an easy up scaling of the SCs areas using classic printing techniques, e.g. so called roll-to-roll printing techniques (Fig. 1.2(a)) on top of flexible, low weight plastic substrates. One could also tune the molecular structure design of the organic semiconductors and modify their color appearance. This combined with a high absorbance coefficient [10] and a possible semi-transparency of the OSCs promises their integration in windows of buildings, as depicted in Fig. 1.2.



**Figure 1.2: (Left) Roll of OPV solar cells processed by Frederic Krebs group [11], (Middle) Integration in windows of buildings, and (Right) Swiss convention centre with DSSC Glass.**

### 1.2 Importance of New Solar PV Technologies

With the advent of nano science and technology, it is postulated that nano materials can revolutionize solar PV technology. In other words, cost-effective solar PV technology with high solar energy conversion efficiencies is possible with nano materials [12]. It has been observed that nano materials exhibit enhanced photon absorption and photo-carrier collection efficiencies [13] and the enhanced solar PV output is based on novel PV mechanisms [14] because nano materials characteristics like quantum confinement, band gap, work function, etc. are intrinsic in nature and can be controlled to deliver enhanced solar energy conversion efficiencies by easy synthesis/processing procedures. If not for the constraint laid by availability of feedstock of materials and materials processing technologies to meet the production rate of solar PV modules, achieving Giga watts (GW) level of power through solar PV in the near future may not be an impossible reality. As mentioned in the next chapter (Section 2.2) the fabrication of solar PV modules and integrated systems depends greatly on the availability of common materials (used in fabrication of different segments other than the actual power generating segments of a typical solar PV system), such as Ag, Cu, plastics and polymers, glass materials, steels, construction materials (such as cement and concrete) etc., and also unique materials such as Si, In, Te, Se etc., depending on the type of solar PV being developed. In order to meet the materials demand in fabrication of solar PV systems, there should be an increase in the production of the above mentioned materials and their availability to meet the huge demand [15]. For example, in the case of CIGS and CdTe-based solar PV systems, the development is hindered by the limited availability of In and Te. Therefore, there is a need for the development of efficient methods to refine primary ores of In and Te. In the case of Te, its extraction from Mn nodules on the seabed has to be rigorously taken up. At the same time, there is also a need to simultaneously enhance Zn and Cu extraction. Improvement in solar PV technology could also be mainly driven by:

- (1) Technologies that could use thinner layers than those used today
- (2) Recovering and using materials that are lost during layer fabrication and
- (3) Finding substitution (for example, indium) for elements such as gallium or aluminum.

### 1.3 Problem Definition

Even though the efficiencies of DSSCs with graphene related materials (such as graphene obtained through electrophoretic deposition [16] and graphene with incorporation of SiO<sub>2</sub> nanoparticles [17] as CE materials are high (5.9% [16] and 4.04% [17]), the fabrication of such

## Introduction

---

devices involves complex process steps and therefore requires optimization of a number of process parameters. In another important work [18] the efficiency of DSSC with photo thermal reduced graphene oxide (P-rGO) as CE was 7.62%. However, the method used for fabricating the final CE may not be suitable for realizing large area CEs. In the case of graphene based composites as CE materials in DSSCs, it is difficult to understand and control the electrochemical activity at the electrode/electrolyte interface. However, graphene ink [19] spray coated on FTO substrates was used as a CE in fabricating large-area DSSC modules. In this case, the electrochemical activity at the electrode/electrolyte interface could be easily explained. Additionally, using a CE composed of graphene nano platelets (GNP), in the structure FTO/Au/GNP, produced a DSSC with a record efficiency of over 14% [20], outperforming a similar FTO/Pt CE DSSC. In both cases, the electrolyte was a cobalt(III/II) tris(1,10-phenanthroline) complex ( $[\text{Co}(\text{phen})_3^{3+/2+}]$ ) transition metal redox couple system with  $\text{TiO}_2$  electrodes co-photo sensitized with a strongly anchored alkoxy-silyl- dye (ADEKA-1) and a carboxy- organic dye (LEG4). Owing to the innate nature of the CE materials used in this thesis work, the electrochemical activity at the electrode/electrolyte interface attains importance. Also the motivation is to replace Pt with a suitable graphenaceous CE material. In the case of PSC technology, 5% to beyond 9% of power conversion efficiencies were reported in single junction polymer solar cells by using solution processable methods. Typically Ca is used as ETL while Al or Ag is used as electrode [21]. However, there are several issues associated with the use of Ca as the ETL. Due to its low work function of 2.87eV, Ca is air and water sensitive making it only suitable for processing in an inert atmosphere [22]. Instead of Ca, thin layers of n-type organic materials ( $\sim 5$  nm) such as BCP can be used. However, in both cases an expensive and time consuming thermal-vacuum evaporation process is required for the ETL deposition, which in turn degrades the performance of the PSCs due to diffusion of depositing material into the active layer during the process [23]. Alternatively, solution processed metal oxides such as  $\text{TiO}_2$ ,  $\text{TiO}_x$  or ZnO are used as ETLs, due to several benefits over thermally evaporated counterparts [24][25][26]. However, it is worth noting, that solution processed metal oxides commonly require additional annealing after deposition, which could induce alterations to the underlying device photoactive layers and degrade the device performance. While in conventional 3G generation polymer solar cells, the device performance as well as longevity was improved by judicious design and selection of donor/acceptor polymers, the incorporation of carbon nanotubes, graphene and its derivatives in the device architectures. To date, the most efficient organic photovoltaic cells (OPVs) was first proposed by Yu et al., was based on the bulk hetero junction (BHJ) concept [27]. This involves formation of localized

## Introduction

---

nano hetero junctions which assist in spontaneous dissociation of the photo generated excitons at the interface between fullerene derivative and exciton generating polymer [28]. For efficient exciton generation the phase separation should happen in a manner such that there exists a nano heterojunction within the exciton dissociation length of the organic material. Furthermore, the phase separation should proceed such that each phase forms a percolation pathway to the respective electrode such that charges are extracted with minimum recombination [29]. Therefore, in this thesis work, new ETL materials and easy processing steps have been planned such that the device degradation is negligible. The ETL materials used in this work are spin coated on the photosensitive BHJ layer by mixing them in methanol, which allowed the ETL deposition at room temperature i.e., without the need for further thermal treatment like in the case of conventional metal oxide precursors used to deposit metal oxides as ETLs.

### 1.4 Overview of the Thesis

In Chapter 1 introductory discussion about the issues in present day solar grade materials' science and engineering utilized to harness renewable solar energy through different technologies (more specifically the 3G solar cells namely DSSCs and OPVs). In Chapter 2 detailed review on aspects related to various solar grade materials, and influence of the use of solution processable chemically modified graphenaceous materials on enhancement of solar energy harvesting are presented. Graphene based materials and composites used as CE materials for DSSCs and ETL layers in OPVs and other relevant issues to this thesis are presented. In Chapter 3 detailed experimental work related to the fabrication and testing of DSSC with SRGO as CE and OPVs with different graphenaceous materials as ETLs is presented. It should be noted that Chapter 3 is an important chapter (along with Chapter 4) in this thesis work because novel materials, materials' processing methods and solar cell fabrication methods have been introduced for the first time as far as DSSCs and OPVs are concerned. In Chapter 4 results obtained in this work and the related discussion is included. In Chapter 5 conclusions of the thesis work and immediate future scope of this research work are presented. All the references that have been cited in the thesis are arranged and numbered in the order they appear in the main text under the heading 'References' at the end of the thesis.

---

## Chapter 2 Literature Review

### 2.1 Current Status of the Solar PV Technology

In solar PV technology, solar radiation is directly converted into electrical energy by a solar cell, which is typically made of a solar grade semiconducting material (like Si, GaAs, CdTe, Cu(In,Ga,S) Se<sub>2</sub>(CIGS) and/or other suitable semiconductors), which gets exposed to sunlight to generate electric power, the amount of which depends typically on solar radiation's intensity, solar cell's active surface area, the type of solar grade material with which the solar cell is fabricated, and the ambient temperature. Solar PV cells are typically p–n junction-based devices, which are constituted by materials in the form of thick (few hundreds of microns) or thin films (few microns) in single as well as multi-layered configurations such that they absorb solar radiation. The principle of solar PV technology is as follows: the semiconducting material with which the solar cell is fabricated absorbs solar radiation (i.e., photons) and generates electron–hole pairs, which dissociate through the p–n junction or equivalent interfaces in the solar cell, and finally the charge carriers are collected at the conducting contacts of the cell.

However, there are limitations with respect to the conversion efficiencies of p–n junction based PV solar cells. For example, for a PV solar cell based on a p–n junction made of a single solar grade semiconducting material, the conversion efficiency is dependent on the band gap of the semiconductor. The conversion efficiency of only ~30% can be achieved using materials with their band gaps in the range 1.2–1.5 eV. In this case, the maximum photo-voltage ( $V_{\max}$ ) is given by  $V_{\max} = (E_g/e)$ , where  $E_g$  is the band gap of the solar grade material and  $e$  is the charge on the electron. Therefore, the conversion efficiency is limited for a particular band gap because the photons of energy less than the band gap energy are not absorbed and do not contribute to the conversion efficiency. However, with time the solar PV technology has improved from high cost and high efficiency 1<sup>st</sup> generation (1G) thick crystalline Si/GaAs wafer based solar cells to low-cost and low-efficiency 2<sup>nd</sup> generation (2G) amorphous or polycrystalline Si, CdTe and CIGS thin film based solar cells. Further improvement in the understanding of materials science and development of novel materials' processing techniques has resulted in inexpensive and highly efficient 3<sup>rd</sup> generation (3G) solar cells, which are based on nano crystalline thin films, quantum dots and tandem or stacked multilayers of inorganic materials based on III–V compounds. 3G solar cells' family also consists of organic (or polymer) solar cells and dye-sensitized solar cell (DSSC) or semiconductor-sensitized solar cells, which work on hot carriers concept. At present, low-cost and high-efficient 4<sup>th</sup> generation (4G) solar PV technology, which

is based on flexible polymer thin films, is still under research and development stage [30]. The timeline of 1G–4G solar cells is shown in Fig. 2.1.

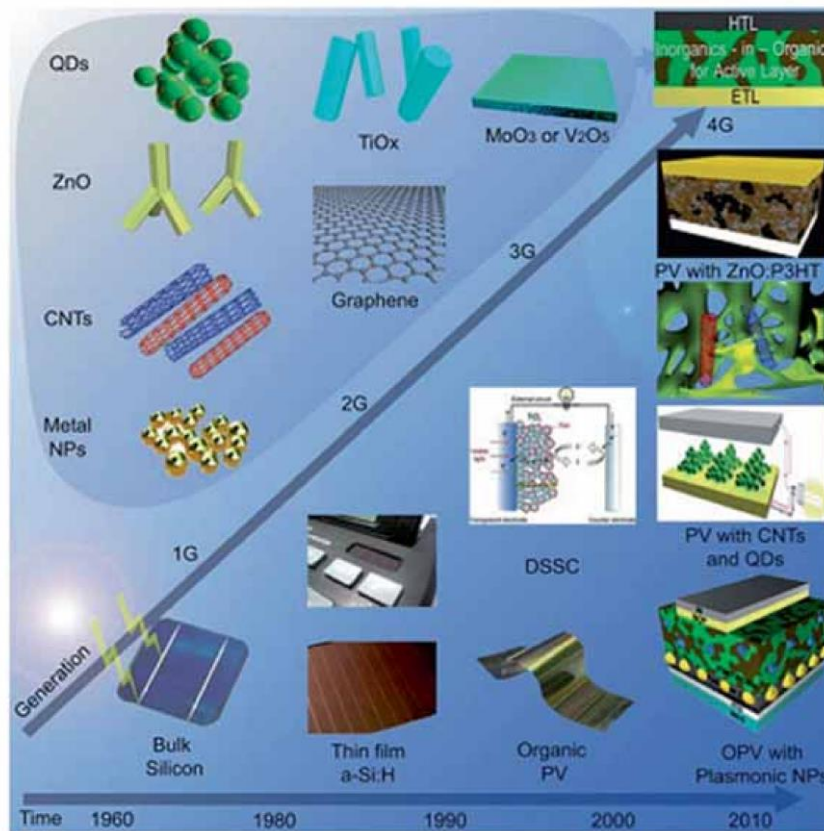


**Figure 2.1: Timeline of different generations of solar cells [30].**

## 2.2 Materials for Solar PV Technology

All emerging solar energy harvesting technologies are greatly dependent on the availability of natural solar grade materials (as shown in Fig. 2.2 in the next page) and/or on the advancement of materials engineering and understanding of science at small length scales (i.e., phenomena associated with solar grade nano materials). Si is the most abundant element, therefore Si-based solar PV technology is now operational [31]. The highest conversion efficiency for Si-based solar cells reported until date is 25.6% [32]. Solar PV cells are typically made from polycrystalline Si or poly-Si wafers. Poly-Si wafers (which are either mono-crystalline or polycrystalline) are made from metallurgical grade Si. Nearly 90% of solar PV technology is based on Poly-Si, while silver is used for electrical front contact grids. In the following subsections, materials used in conventional Si-based solar cells, materials in thin-film based solar cells and the novel nanomaterials and nano science used in the modern era of solar energy conversion are presented.

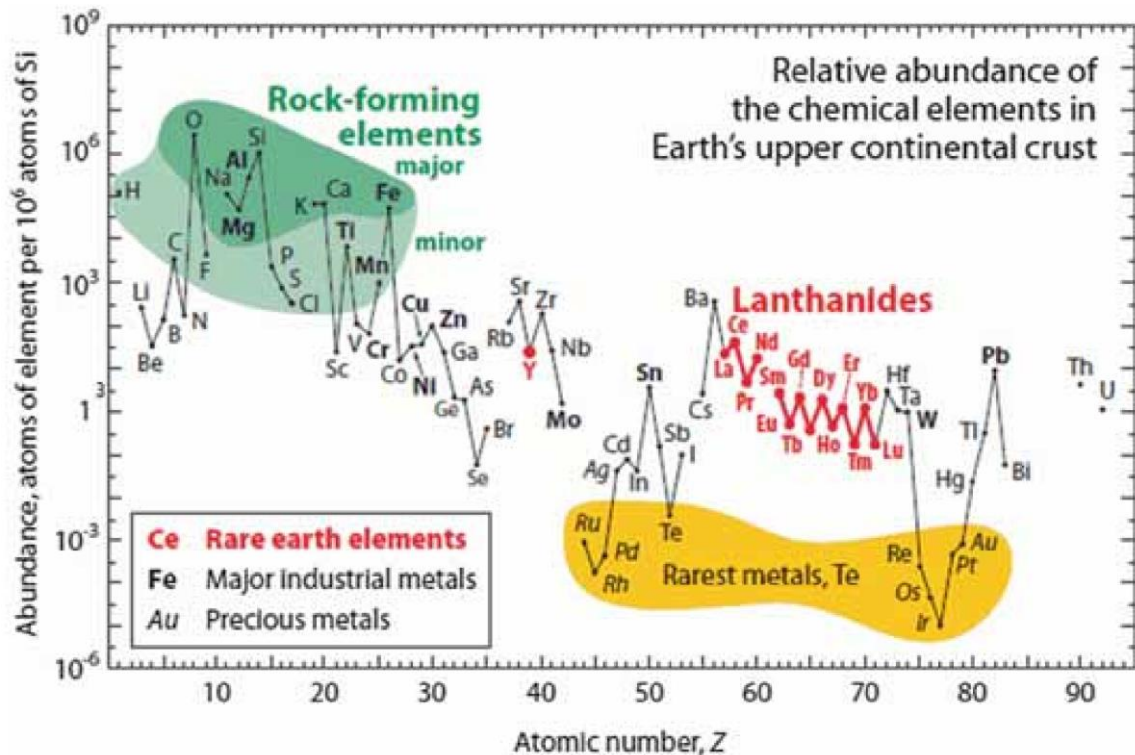


**Figure 2.2: Abundance of various elements in Earth's upper continental crust. Si is one among the most abundant elements [31].**

### 2.2.1 Materials in conventional Si-based solar cells

The conventional Si-based p–n junction solar cell configuration, the p-region is B-doped Si wafer, while n-region is P-doped Si. The front electrical contacts are usually made of Ag and are used to collect the photoelectrons. The back electrical contact is typically made of Al, which is screen printed on the entire B-doped Si wafer's back surface. The back contact is used to collect the holes. Light absorption losses due to reflection at the front surface are minimized (in other words, light absorption by the solar cell is enhanced) by chemically texturing the front surface of P-doped Si and applying a suitable antireflection coating. The conventional amorphous Si (a-Si) thin film solar cell configuration, the p–n junction is formed by sandwiching thick intrinsic a-Si layer between thin p- and n-type a-Si regions. The front and back contacts are typically transparent conductive SnO<sub>2</sub> and Ag layers, respectively. Enhancing light trapping, which is discussed in the following paragraphs, is an important aspect in these cells. The highest conversion efficiency for Si-based solar cells reported till date is 25.6%, which is for a hetero junction (with-intrinsic-layer inter digitated back contact) solar cell [32]. The high efficiency of this cell is a result of excellent surface passivation, indicated by high open-circuit voltage ( $V_{oc}$ ) of 740 mV in combination with excellent light trapping indicated by high short-circuit current density ( $J_{sc}$ ) of 42.7 mA cm<sup>-2</sup> and that too on a cell of thickness less

than 100  $\mu\text{m}$ . Conventionally, light trapping is made effective (i.e., to achieve high  $J_{\text{sc}}$  on unmetallized front surfaces) in commercial cells by chemically texturing (with a feature size in the range 3–10  $\mu\text{m}$ ) the front surface and applying a suitable anti-reflection coating of thickness less than 100 nm [33]. However, this concept is not suitable for thinner cells owing to the large feature size on the textured front surface and moreover chemical texturing and applying anti-reflection coating do not render a cost-effective solar cell. In this context, it was found out that nano structuring (light management through design) could be used to enhance light trapping and improving the conversion efficiency of the solar cells. It is known that small metallic and dielectric particles can strongly scatter light owing to their optical resonances [34], namely surface plasmon and Mie resonances, respectively; this aspect was utilized not only to couple but also to efficiently trap light at the front surface of Si-based solar cells [35]. Moreover, the resonant small metallic and dielectric particles exhibit light scattering cross sections that are much larger than the geometrical areas of the scattering particles themselves; this aspect permits enhanced interaction of the small particles with the incident light even when these cover less than 30% of the front surface area [36]. Further, the scattered light by the resonant particles prefers to travel towards nearby materials with high density of optical states, i.e., materials with high refractive index [37]; this aspect helped to augment the light absorption in solar cells fabricated using materials with high refractive index. The strong light scattering allowed enhancement of light absorption by the solar cell and thereby the enhancement in number of photoelectrons per unit area (i.e.,  $J_{\text{sc}}$ ). Smoother the front-end surface (anti-reflection coating), lesser is the surface recombination of charge carriers and thereby enhancement in  $V_{\text{oc}}$ ; this is what exactly happens when nano structuring/nano patterning is used [38]. Additionally, metal particles can also be inter connected and used as an electrode in the solar cell. It has been shown that transparent Ag nanowire networks [39] can be formed as a conductive electrode, which can replace  $\text{SnO}_2$  or in general transparent conductive oxides used as front contacts. This approach renders photocurrent extraction more effective, decreases the series resistance, and thereby enhances the fill factor of the solar cell. In the case of small dielectric particles, at resonance, the light is confined in well defined geometrical modes (Mie resonances) inside the resonant particles [34], which are used to couple the strongly scattered light (due to Mie resonance) preferentially into the high refractive index possessing crystalline Si. It is important to also make a note that the small metallic and dielectric particles can be used on not only the front [40] and backsides [41] of the cell but also inside [42] the active material of the solar cell. As mentioned before, the crystalline Si-based solar cell with the highest efficiency ever is a hetero junction inter digitated back contact (IBC)-back-junction, which implies that the

junction and the conductive contacts are at the backside of the cell, which has inter digitated finger configuration constituted by alternating highly p-doped Si regions forming the junction with highly n-doped regions forming back surface fields to repel minority charge carriers.

The front side of the cell can either be textured or flat, the later reduces the surface recombination of charges. In a flat front side configuration, a thin  $\text{Al}_2\text{O}_3$ /intrinsic a-Si:H passivation layer is used (when n-type Si is the active material) to create an inversion near the front surface where holes become majority charge carriers [43]. On the passivation layer,  $\text{TiO}_2$  Mie resonant layer is applied for anti-reflection and light trapping purposes. Owing to the above-described design, shadowing/ recombination is nullified at the front side of the cell while light absorption is enhanced due to the mediation of Mie coating, which is now overlapped with the active layer and decoupled from the highly doped emitter region, which is at the backside in the present configuration. Materials, namely Ag (surface plasmonic type) [44] and Si and  $\text{TiO}_2$  (Mie type) ,[45]have been considered as resonant particles for anti-reflection, light trapping and surface passivation purposes and to minimize parasitic losses.  $\text{TiO}_2$  has rendered excellent results in terms of enhancing the conversion efficiency of the solar cell in comparison to Si and Ag used for the same purposes. Ethyl vinyl acetate which is a typical material used as an encapsulation on the solar cell's front side against weathering has also enhanced the anti-reflection effect in the Si-based solar cells integrated with Mie resonant coatings than with surface plasmon resonant particles [46].

### *2.2.2 Materials in thin films-based solar cells*

Due to the decreasing availability of crystalline Si and back contact materials such as Ag, and brittleness of Si, thin film based solar PV technologies were developed as alternatives to Si-based technologies. Thin film based solar cells are fabricated by depositing thin films of solar grade materials (mainly CdTe, CIGS, GaAs and amorphous Si) on low-cost and easily available substrates such as glass, stainless steel, plastic and so on. Thin film solar cells work on the same principle to that of p–n junction Si-based solar cells except that the cells are much thinner, the active p- and n-type materials are different and the front and back contacts are different. CdS is the most common n-type material used to form p–n junction with the other p-type active materials mentioned above. Multiple junction solar cells can also be fabricated with the same set of materials. At present, the record conversion efficiency is greater than 46% for the multi-junction solar cell based on GaAs, and it is between 22.1 and 25.6% for single junction cells (Si, CIGS, CdTe), while it is between 13 and 21% for recently developed solar cells such as

DSSC [32], organic solar cell and quantum dots solar cell. Of late, hybrid organic inorganic solar cells based on perovskite materials have exhibited record efficiencies (as high as ~22%). Organic–inorganic halide perovskite materials have also gained importance owing to their high power conversion efficiency (PCE) values and their cost effectiveness compared to conventional Si solar cells. These materials are typically represented by the chemical formula  $AMX_3$  (A and M being cations while X being anion; Aorganic, M-divalent metal ions, X-halide). Structurally, A and M cations are at the eight corners and body centre position, respectively, of the cubic unit cell, while M is bonded by six X anions situated at the face centre position. Usually  $CH_3NH_3^+$ ,  $C_2H_5NH_3^+$ ,  $HC(NH_2)^{2+}$  etc. are used as A cations, while  $Pb^{2+}$ ,  $Sn^{2+}$ ,  $Eu^{2+}$ ,  $Cu^{2+}$  etc. are used as M cations and  $Cl^-$ ,  $Br^-$  and  $I^-$  are used as X anions. In this context,  $CH_3NH_3PbI_3$  is an excellent example of organic–inorganic halide perovskite [47]. In 2009, perovskite-sensitized solar cell ( $CH_3NH_3PbI_3$  is the light absorber coated on  $TiO_2$  mesoporous layers and electrolytes are halides) with a significant PCE of 3.81% was fabricated [48]. Moreover, the cell exhibited an excellent photo-voltage of 0.96 V when  $CH_3NH_3PbBr_3$  was used as the light absorber. However, instability of the liquid electrolyte and dissolution of the perovskites in the liquid electrolyte were the drawbacks. Later, PCE and stability of the cell was improved by using spiro-OMeTAD as a solid-state hole transporter and  $CH_3NH_3PbI_3$  and  $CH_3NH_3PbI_{3-x}Cl_x$  as light absorbers. It should be noted that the fabrication of organic–inorganic perovskite solar cells is easy and cost-effective compared to the conventional Si-based solar cells. The fabrication involves firstly the deposition of a  $TiO_2$  hole-blocking layer on a typical FTO substrate. Then, a layer of n-type  $TiO_2$  (which is mesoporous in nature) is either screen-printed or spin-coated using a paste of  $TiO_2$  nanoparticles/polymer binder. As a next step, annealing is done to remove the binder. On top of the mesoporous  $TiO_2$  layer, perovskite film is deposited from solvents such as  $\gamma$ -butyrolactone or N, Ndimethylformamide by spin-coating. To further improve the conductivity, a hole transporter layer such as spiro-OMeTAD is applied on the perovskite. Finally, a transparent metal electrode is deposited as the top most layer to enable most of the incoming solar radiation to reach the active material and thereby resulting in the generation of charge carriers. Moreover, the coloured perovskite- and dye-sensitized solar cells with transparent electrodes enhance the aesthetic value of the buildings, in which these solar cells are integrated into the architectural glass. Based on this basic multi-layered configuration, different experiments were conducted by manipulating the materials' characteristics in each layer to improve the conversion efficiencies with better  $V_{oc}$  values. Out of all the manipulations, the thickness of mesoporous  $TiO_2$  was found to greatly affect the PCE values of the cell [49][50][51]. On the other hand, similar configuration without

the hole transporter showed a conversion efficiency of 5.5% [52][53]. The conversion efficiency was enhanced to 8% by varying the perovskite layer thickness. Later, meso-structured solar cell configuration (in which an  $\text{Al}_2\text{O}_3$  layer (which is both mesoporous and insulating in nature)) is deposited on the top of the  $\text{TiO}_2$  [54][55][56][57].  $\text{Al}_2\text{O}_3$  layer acted as a scaffold that aided loading of the active perovskite material (mostly  $\text{CH}_3\text{NH}_3\text{PbI}_{3-x}\text{Cl}_x$ ) in it [54][55][56][57]. It was observed that the electron transport occurs within the perovskite unlike in the case of mesoporous  $\text{TiO}_2$  perovskite configuration and this leads to increase in  $V_{oc}$  values of the cell due to accumulation of charge in the perovskite. Recently, phase stable  $\text{CsPbI}_3$  perovskite-based solar cell with conversion efficiency of 10.77% and  $V_{oc}$  of 1.23 V (equivalent to e.m.f. of a battery) has been fabricated [58]. In another study, mesoscopic  $\text{CH}_3\text{NH}_3\text{PbI}_3/\text{TiO}_2$  heterojunction with a double layer of  $\text{TiO}_2$  and  $\text{ZrO}_2$  as scaffold and carbon as back contact was shown to deliver a power conversion efficiency (PCE) of 12.8% and exhibit long-term stability [59]. Further uniform crystal growth of perovskite material was obtained using a two-step process, in which, first  $\text{PbI}_2$  was spin coated from dimethylformamide onto the mesoporous  $\text{TiO}_2$  film and then exposed to  $\text{CH}_3\text{NH}_3\text{I}$  in isopropanol to form the final perovskite pigment that penetrated the mesoporous  $\text{TiO}_2$ . This configuration increased the PCE to 15% with an excellent reproducibility.[60] Recently, PCE of 17.01% was achieved by spin coating  $\text{CH}_3\text{NH}_3\text{PbI}_3$  cuboids [61]. Recently, Prof Grazel's research team has achieved a record PCE of 21.1% with Ce containing first triple cation perovskite mixture. These films are more heat stable and less affected by experimental environment, and a PCE of 18% was also observed ever after 250 h exposure to operational conditions [62]. Apart from the above presented advantages, stability and toxicity are major challenges for commercializing perovskite solar cells. To overcome the toxicity issue, lead-free perovskite solar cells with Sn replacement were proposed. These cells exhibited conversion efficiencies of ~6% [63][64]. CdTe cells made by First Solar Inc., Arizona, USA, and CdSe cells made by Bloo Solar Inc., California, USA, have unique layered structures. These cells have shown good results. CIGS cells are relatively new amongst the thin film based metal-semiconductor solar cells. CIGS cells not only exhibit higher conversion efficiencies but are also less costly. Unfortunately, CIGS cells are very sensitive to moisture. This drawback has hindered their full commercialization. The commercialized CIGS cells exhibit efficiency of ~15%, whilst the developmental CIGS cells exhibit efficiency up to ~20%. In India, for example, ARCI (an autonomous DST Research Centre), Hyderabad, is developing the large area CIGS thin film-based solar cells. An interesting aspect of solar cells with CIGS technology is that the optical

band gap can be graded by varying the dopant (III A group elements like Ga (from 1.0 to 1.7 eV) or Al (from 1.0 to 2.7 eV)). They can also be fabricated by wet chemical route. For better junction, Al doped ZnO as an electron donor layer for CIGSe active layer with Al contacts showed a good external quantum efficiency of around 35% [65]. Parallel to the development of metal and semiconductor-based thin-film solar cells, organic thin-film solar cells are also being developed. These solar cells are fabricated by dissolving organic semiconductors in solvents or inks, which are either printed or coated onto plastic substrates in a continuous roll-to-roll process. In this context, knife over-edge, slot die and gravure coating methods are well practiced [66][67], as they give an idea about ink parameters in correlation to the interaction between the ink and the surface that is to be coated, which is very important for manufacturing high volume solar modules in quick time. The use of nano materials in these cells has been observed to trap enhanced energy [68]. Commercial triple junction thin-film solar cells made by Emcore Photovoltaics and Spectrolab exhibited efficiency of ~38%. At the same time, there is still a great scope for all the advancements that are at present limited to laboratories. Another interesting set of modules are the flexible thin-film modules with plastic front sheets, which are mostly the transparent monolayer fluoropolymer films such as ETFE or its derivatives. Rowland Technologies Inc., Wallingford, made front sheet named Rowlar (using Arkema's Kynar PVDF), which shows light transmission greater than 93% and haze less than 9%. However, India is lagging behind in research and development related to organic thin-film-based solar cells. As discussed in the previous section, preferential light scattering by resonant particles can also be used to enhance light trapping and coupling into GaAs, CdTe or CIGS thin-film-based solar cells. For enhanced light trapping, surface plasmon resonant particle can be embedded in low refractive index materials such as perovskites and organic materials used in thin film solar cells [42].

### *2.2.3 Nano- materials and science in solar PV technology*

Even though Shockley-Queisser (SQ) limit was surpassed by multi-junction solar cells, commercialization of these solar cells is yet to be realized. By utilizing the science at small length scales (i.e., using nano materials and the related novel physics) too, SQ limit can be surpassed. One of the earliest solar cells which used 'interpenetrated junctions' or 'bulk hetero junctions' are DSSCs, whose mechanism was explained in the previous section. These cells worked on 'geometric confinement effect' at a small length scale, namely the 'nanoscale'. Unlike in the conventional PV solar cell, the incident light absorption volume was made less than the charge carriers' diffusion length. The thickness of the absorbing material was made a

few nm to a few tens of nm. Donor and acceptor nano materials (both organic and inorganic nanowires and nano rods) occupied the space between n and p regions of the solar cell. By geometrically confining the active material domains, effective separation of charge carriers was possible. P3HT and PCBM mixture was the most used organic material in polymer bulk hetero junction solar cells. The highest efficiency using the concept of geometric confinement was 11.7% [69]. However, transport of charges to the electrodes is poor in these cells. One way to overcome this problem is to have vertical donor material nanowires (with diameter in the order of the exciton diffusion length and length equivalent to the carriers' diffusion length to the electrodes) embedded in an acceptor material matrix in such a way that the nanowires act as percolation paths to the electrodes.

Another way to augment solar cells' conversion efficiency is by using nanostructures (dots, wires, tubes etc.) that exhibit quantum confinement effect, which renders wave-like behaviour to electrons and the carrier transport is strongly confined in a given dimension. The nanostructures are embedded in a material, in which the electron wave functions do not overlap. In the case of Si, Ge, PbS etc., the nanostructures are embedded in the matrix of an insulating material such that the transfer of electrons takes place from one nanostructure to the other in the matrix through the tunneling effect owing to the wave nature of the electron. The quantum effect in nanoparticles increases the band gap of the material, i.e., the band gap of Si quantum dots can be varied from 1.3 to 3 eV by decreasing their size from 5 to 1.2 nm. Theoretically, it was predicted that for all-Si tandem cell, which utilizes the quantum effects of Si nanostructures there will be an enormous increase in  $V_{oc}$  (owing to larger band gap in Si nanostructures) and thereby an efficiency solely based on quantum effects can be as high as 29% [70].

### 2.3 Development of Fundamentals

#### 2.3.1 Dye sensitized solar cells

Gratzel cells or Dye Sensitized Solar Cells (DSSCs) [71], [72], are expected to challenge the performance of Si based solar cells and compete for a significant market share in next generation solar cells. This is owing to their good performance even under diffuse light [73], lower production costs, innate solution processability which allows easy fabrication of large area cells, and excellent unit price per performance metric which allows them to gain grid parity. A DSSC typically consists of a photoanode, an electrolyte with redox species (such as iodide/triiodide ( $I^-/I_3^-$ ) in an organic solvent), and a counter electrode (CE). The anode consists of a transparent conducting oxide (TCO) coated glass substrate with a layer of

mesoporous network of wide band gap metal oxide semiconductor, such as TiO<sub>2</sub>, which is sensitized with a suitable dye. The redox couple in the electrolyte works as a mediator which transfers electrons from the cathode to the oxidized dye molecules [74]. I<sup>-</sup> ions reduce the sensitizer and oxidize to I<sub>3</sub><sup>-</sup> ions while the monovalent I<sup>-</sup> ions are recovered at the cathode.

Commonly, platinum coated TCO glass substrate is used as the CE because of platinum's high catalytic activity and resistance to corrosion due to the electrolyte. However, due to platinum's high cost and low corrosion resistance to the iodide based electrolytes [75][76], scientists have investigated alternative CEs and redox couple electrolytes other than iodide/triiodide (I<sup>-</sup>/I<sub>3</sub><sup>-</sup>). These alternative electrolytes, such as anion doped PEDOT [77], have assisted in producing stable solid state DSSCs. Detailed discussion on fabrication and alternative counter electrodes is presented in the Sections 2.4.1 and 2.5.

### 2.3.2 Organic photovoltaic

Carbon is the most common chemical element contained in organic materials. It has the atomic number six, thus four of the six electrons of carbon occupy the valence band. According to the Hund's rule, it therefore has the electronic configuration 1s<sup>2</sup>2s<sup>2</sup>2p<sup>2</sup> (one electron each in 2p<sub>x</sub> and 2p<sub>y</sub> orbitals, and no electron in 2p<sub>z</sub>) [78]. Generally, organic semiconductors are defined by a sequence of follow in turn of single and double bonds between the carbon atoms. This structure, also called conjugation, provides the essential optical and electronic properties required for the material to interact with visible radiation. Hybridization of the carbon atom's orbitals lead to energetically stable state. In an sp<sup>2</sup> hybrid, the valence electrons of carbon reside in sp<sup>2</sup> hybridised orbitals (3 electrons) both in the plane, and in one p<sub>z</sub>-orbital (1 electron) perpendicular to the sp<sup>2</sup>-orbitals. The electrons in the sp<sup>2</sup>-orbitals form covalent bonds with neighbouring atoms via  $\sigma$  molecular orbitals. The remaining electron in the p<sub>z</sub>-orbital can form a covalent bond with a neighbouring p<sub>z</sub> electron and form a  $\pi$  molecular orbital. The carbon atoms in a sp<sup>2</sup> hybridized ethylene molecule are depicted by a double bond ( $\sigma$  and  $\pi$ ) between the carbon atoms. An energy diagram of a double bonded carbon molecule. It shows that two electrons each occupy the  $\sigma$  and  $\pi$  molecular orbitals. The remaining four carbon electrons are non-bonded, and therefore available for creating bonds [79]. The discrepancy between the energy levels of bonding  $\sigma^-$  and antibonding  $\sigma^+$  molecular orbitals is very high and beyond the visible light spectra. The electron wave functions in the p<sub>z</sub>-orbitals along the backbone overlap (also known as conjugation), which causes a splitting between the  $\pi$  and  $\pi^*$  molecular orbitals [79]. The electrons are delocalized in the conjugated backbone of the molecule and are

therefore associated with a molecular orbital. Furthermore, the  $\pi$ -bond strength is significantly weaker in comparison to the  $\sigma$ -bond, which causes an additional splitting between the  $\pi$  and  $\pi^*$  molecular orbitals into smaller energy levels depending on the number of conjugated molecules. A stronger conjugation caused by the increased number of alternating single and double bonds narrows the fundamental energy gap and forms a band structure. In this band structure, the electronic levels are defined as the Highest Occupied Molecular Orbital (HOMO) and the Lowest Unoccupied Molecular Orbital (LUMO) as shown in Fig. 2.3.

The energy of the HOMO level is considered to be the ionization potential (IP) required to displace an electron from the HOMO level into the vacuum energy, whereas the energy of the LUMO level is referred to as the electron affinity (EA) of the molecule (the energy needed to inject an electron from vacuum energy into the LUMO). Hence, the fundamental energy gap is defined as the difference between the IP and the EA of the organic molecule [80]. For organic semiconductors, this energy is typically between 1.5eV–3eV [78] the difference between the HOMO and LUMO levels, (known as the band gap) corresponds to a particular energy which if applied can excite electrons from the HOMO level to the LUMO level. According to the Planck-Einstein relation, the energy of a photon of light is directly proportional to the frequency of the light. Therefore, because the frequency of light can be expressed as the speed of light divided by the wavelength, the energy of a photon is inversely proportional to the wavelength of the light. This means that if a semi conducting material with a specific band gap is illuminated by light of corresponding wavelength, an electron will be promoted from the valance band to the conduction band.

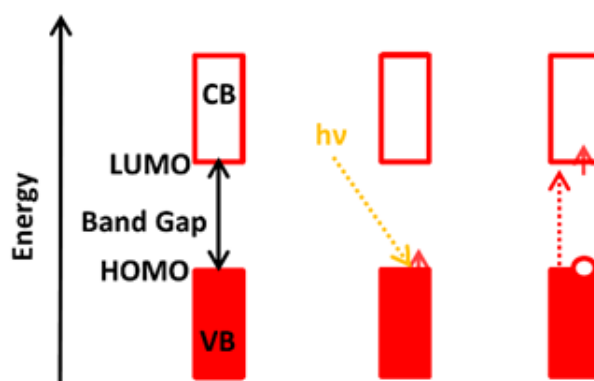


**Figure 2.3: Band structure of a typical OPV Device.**

An exciton which is a strongly bound electron-hole pair is formed due to the absorption of a photon with sufficient energy by an organic semiconductor. This strong coulombic attraction between the electron and the hole is due to the low dielectric constant of organic

materials ( $\epsilon_r \sim 2-4$ ). The exciton is, therefore, referred to as a Frenkel exciton and has a binding energy of 0.5–1.2 eV, which is much larger than the binding energy observed for Wannier excitons in inorganic semiconductors (thermal energy of  $\sim 26$  meV at room temperature is sufficient to create free charge carriers) [81]. Due to typically weak intermolecular interactions in organic materials, excitons are localized on molecules and not in energy bands. The generation of excitons in organic materials does not immediately lead to the formation of free charge carriers that contribute to the current. Instead, the binding energy of the exciton first has to be overcome, in order to separate the electron-hole pair. Nevertheless, when sufficient high energy band offset is provided, the exciton binding energy can be overcome, leading to the exciton separation. This is often the case at the interface between p-type donor (D) molecules that exhibit a low IP and therefore high-lying HOMO level, and n-type acceptor (A) molecules with a high EA and thus a low-lying LUMO level [82].

A considerable breakthrough in the field of organic-based PVs was made in 1986 when Tang *et al.* showed a significant enhancement of the dissociation probability of photo generated excitons by developing the first organic cell with a D/A bi-layer hetero junction [89]. The photoactive layer was deposited by thermal evaporation under high vacuum, and sandwiched between electrodes of ITO and Ag [83]. In this bi-layer structure, as shown in Fig. 2.4(a) (next page), a photo induced charge transfer of electrons from a p-type donor (polyene diimide derivative) to a n-type acceptor (copper phthalocyanine) was demonstrated.

However, there is a major drawback associated with the bi-layer hetero junction OPVs. To avoid exciton recombination, the thickness of organic layers needs to comply with the exciton diffusion length  $L$  of 10 nm – 20 nm ( $L = (D\tau)^{1/2}$ , where  $D$  is the diffusion coefficient and  $\tau$  the exciton lifetime) [84][85]. As a result, for bi-layer hetero junctions, an efficient exciton generation and transport can usually be accomplished for photoactive layers with a thickness around 20 nm. However, the ability of the D/A system to absorb efficiently light is greatly reduced for such thin layers [86]. An approach to overcome the limitation of the bi-layer D/A hetero junctions was proposed with the introduction of the bulk-hetero junction (BHJ). The pioneering work in this field was carried out by Yokoyama *et al.*, who showed a twofold increase in photocurrent compared to a double-layered cell, due to an efficient photo generation in a co-deposited interlayer [87]. Further developments were achieved by Heeger and Sariciftci, who in 1992 patented the “Conjugated polymer–acceptor hetero junctions; diodes, photodiodes, and photovoltaic cells” [88]. The first applications of this invention followed soon

after in papers by Heeger *et al.* and Friend *et al.*, who reported the deposition of BHJ layers from a solution containing a D/A mixture in order to form a layer with an interpenetrating network of both materials [27][89]. In this respect, if the length scale in the D/A blend is comparable to the exciton diffusion length, then the probability of the exciton reaching a D/A interface is significantly increased. By means of this, the recombination of excitons is dramatically reduced. Additionally, exciton generation and respectively, dissociation, can occur everywhere in the BHJ due a larger interface area than in the bi-layer hetero junctions. This also allows for the deposition of thicker photoactive layers that absorb a greater photon flux. Since the first reports of BHJ-based photoactive layers, this type of hetero junction has therefore become the standard D/A system for OPV devices [86]. Schematic band diagrams of OPV cells with a D/A bi-layer and a BHJ system are shown in Fig. 2.4(b). Due to the common use of this system, the fundamental processes that occur in the photoactive blend are described for the BHJ system in Fig. 2.4(b).

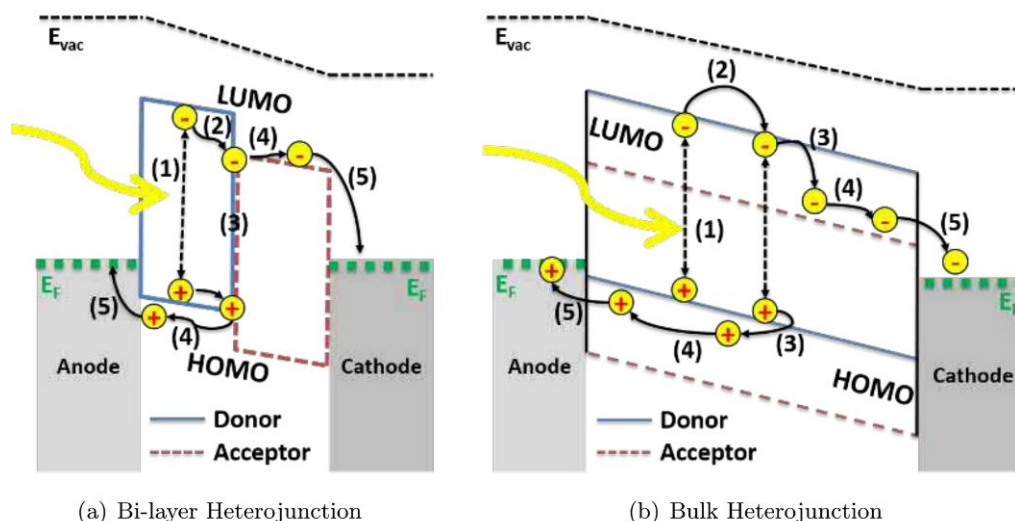


**Figure 2.4: Schematic band diagram of (a) bi-layer and (b) BHJ solar cell under illumination and under short-circuit condition. The HOMO and LUMO energy levels of the donor and acceptor materials are shown with continuous blue or long dashed red lines.  $E_F$  is the Fermi level of the metal electrode and  $E_{vac}$  the vacuum energy. The generation of free charge carriers is summarized in five steps.**

The working principle of the OPV device, however, is identical for both hetero junctions and is described in five fundamental steps: charge carrier generation; diffusion; dissociation; transport; and extraction/collection at the electrodes. In the first step, Organic semiconductors exhibit large absorption coefficients of about  $10^5 \text{ cm}^{-1}$ , which allows them to efficiently harvest most of the photons within their absorption spectra in thin layers (100 nm – 200 nm)

[90]. If the energy of a photon is high enough, *i.e.* superior to the fundamental gap of the organic semiconductor, an electron is pushed from the HOMO to the LUMO level of the material. A neutral entity made of a coulombically bound electron-hole pair called exciton is created. Most of the incident photons lead to the generation of electron-hole pairs in the donor domain, due to the electron-rich nature of the p-type material. Therefore, it is assumed that the photoexcitation of the donor material contributes primarily to exciton generation, although photon absorption in the acceptor phase was shown to play an important role for the generated exciton yield as well [91]. In the second step *i.e.*, exciton diffusion, to generate free charge carriers, excitons have to diffuse to the D/A interface, where they can relocate from the D to the A domain by a Förster and/or Dexter mechanism of energy transfer [92][93]. The movement of the exciton is accomplished by hopping along the backbone of adjacent molecules, and is not influenced by an electric field due to the neutral character of the electron-hole pair [82]. Therefore, the conjugation between the  $\pi$  molecular orbitals influences the strength of the intermolecular couplings, that together with the presence of traps and impurities in the p-type material, determine the charge carrier mobilities [94]. As a result, rather low mobilities of about  $10^{-7} \text{ cm}^2 \text{ V}^{-1} \text{ s}^{-1}$  to  $10^{-3} \text{ cm}^2 \text{ V}^{-1} \text{ s}^{-1}$  (*vs.*  $103 \text{ cm}^2 \text{ V}^{-1} \text{ s}^{-1}$  for crystalline silicon) are observed [86][95]. Therefore, in order to avoid a decay of the exciton (recombination of electron-hole pair) from the excited state to the ground state, a nanoscale phase separation between the D/A components with dimensions comparable to the diffusion length of the exciton is required. In the third step, exciton dissociation due to the tight bond between the electron-hole pair, a dissociation into free charge carriers at room temperature (as known for inorganic semiconductors) is not possible. In order for an electron to be transferred from the LUMO level of the donor to the LUMO level of the acceptor, the exciton binding energy has to be overcome. This usually occurs due to the induced electric field at the band offset between the donor and acceptor LUMO levels. However, once the electron migrates to the acceptor, it is still coulombically attracted to the remaining hole in the donor domain. This intermediate state at the D/A interface is called the charge transfer state (CT). There is an ongoing controversy about which mechanisms lead to the dissociation of the exciton from the CT state, a balanced review of which is provided elsewhere [96][97][98]. As this is beyond the scope of this work, it is assumed here that the excited state's energy in the donor is energetically higher than the threshold of the CT state at the D/A interface, and that the energy offset between the D and A LUMO levels is sufficient for an efficient exciton dissociation. In the fourth step, *i.e.*, transportation of free charge carriers, after the exciton dissociation, free charge carriers drift and diffuse in their respective domains towards the electrodes (holes in the donor and electrons

in the acceptor), due to the internal electric field caused by the work function difference of the electrodes [94][90]. Percolated pathways in both material domains are required for an efficient charge transport. It is important to achieve a balanced transport for holes and electrons in order to avoid the accumulation of free charge carriers at interfaces, which can reduce the characteristics of the OPV device. Additionally, the probability of an electron to recombine with a hole are higher in BHJ based systems than in bi-layer hetero junctions, due to the increased contact area at the donor-acceptor interface [78]. In the fifth step i.e., charge carrier collection at the electrodes, once free charge carriers reach the contacts, they can be collected in order to generate electrical currents. However, there is the likelihood of some charges reaching the “wrong” electrode through reverse diffusion, which can lead to their recombination with charges from the electrode material [78]. In order to avoid this loss mechanism, interfacial layers are used to define the polarity of the electrode and to accomplish a facile and selective charge collection (electrons and holes are collected at the cathode and anode, respectively).

### 2.3.3 Electrical characteristics of PV devices

When compared to DSSC it is easier to explain photo voltaic characteristics for organic and inorganic PV cells, which can be represented with the circuit diagram shown in Fig. 2.5. In the dark, due to the p-n junction of the photoactive layer, a solar cell operates electrically as a diode and can be described with the diode Equ. 2.1:

$$I_d = I_0 \left[ \exp\left(\frac{qV}{nk_B T}\right) - 1 \right] \quad (2.1)$$

where  $I_d$  is the current flowing through the diode,  $I_0$  the reverse saturation current of the diode,  $q$  the absolute value of electron charge,  $V$  the applied voltage across the diode,  $n$  the ideality factor of the diode ( $1 \leq n \leq 2$ ),  $k_B$  the Boltzmann constant, and  $T$  the temperature [99]. Under illumination, however, a photocurrent is generated which is represented by the current source  $I_{ph}$  in the circuit diagram. A solar cell also exhibits an internal series resistance ( $R_s$ ) and shunt resistance ( $R_{sh}$ ), as shown in Fig. 2.5 (next page).

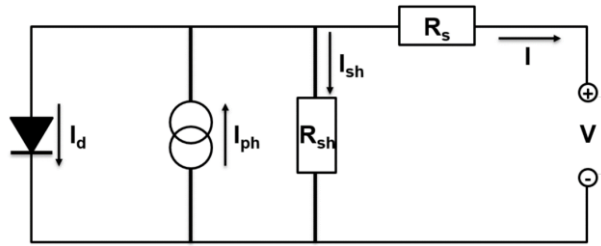


**Figure 2.5: Equivalent circuit diagram of a real PV cell. A diode presents the behaviour of the solar cell in dark;  $I_{ph}$  is the photogenerated current;  $R_{sh}$  and  $R_s$  are the shunt and series resistances of the device.**

$R_{sh}$  describes the leakage current in the device stack, whereas the former represents the resistance of the device to the current flow. A detailed explanation of the Analysis of the characteristics of organic photovoltaic devices and the origin of  $R_s$  and  $R_{SH}$  for OPV devices is provided below. Considering Fig. 2.5, the current  $I$  on the external load is, therefore, the sum of the current through the diode junction  $I_d$ , the photocurrent  $I_{ph}$ , and the leakage current  $I_{sh}$  as given in Equ. 2.2:

$$\begin{aligned}
 I &= I_{ph} - I_d - I_{sh} \\
 &= I_{ph} - I_0 \left[ \exp\left(\frac{qV}{nk_B T}\right) - 1 \right] - I_{sh} \\
 &= I_{ph} - I_0 \left[ \exp\left(\frac{q(V + IR_s)}{nk_B T}\right) - 1 \right] - \frac{V + IR_s}{R_{SH}}
 \end{aligned} \tag{2.2}$$

If the assumption is made that the resistance and recombination processes of the solar cell do not alter with illumination, the current output of the device equals the sum of the diode and photocurrent curvatures. Taking into account Equ. 2.2, the current density-voltage (J-V) plots in Fig. 2.6 can be divided in three zones depending on the voltage range.

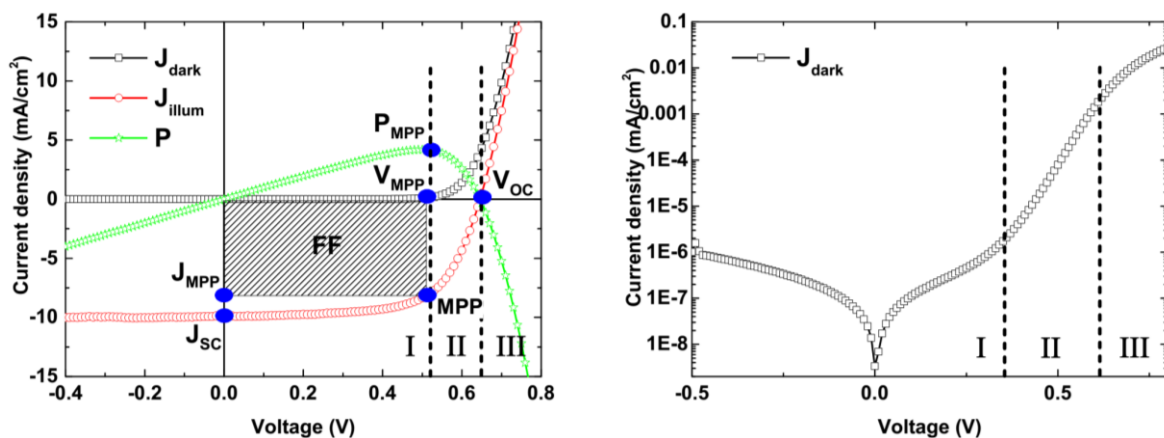


**Figure 2.6: Typical J-V curve of an OPV cell under illumination and in the dark (a) with all characteristic parameters of the OPV device. A semi-logarithmic plot of the  $J_{dark}$  for better visual interpretation is shown in (b). The data is identical.**

## Literature Review

---

In the Fig. 2.6(b), the slope of the J-V plot in zone I is determined by the leakage currents, zone II shows recombination currents and zone III is related to the  $R_S$ ; Zone I represents the J-V curve at negative and low positive voltages, where the slope of the curve is mainly dependent on the  $R_{SH}$ . At intermediate positive voltages (Zone II) the J-V curve is determined by the diode parameters  $I_0$  and  $n$ . Zone III describes the device behaviour at high voltages, where the slope of the curve is governed by the  $R_S$  [100].

All main parameters of a PV device can be extracted from its J-V curve under illumination and in the dark. As shown in Fig. 2.6(a), the short-circuit current density ( $J_{SC}$ ) of a solar cell is described as the current at zero applied voltage. The voltage measured at zero current value is the open circuit voltage ( $V_{OC}$ ). The maximum power point ( $P_{MPP}$ ) is defined as the operation point with the highest electrical power  $P$  and is described as a product of the current and voltage at the MPP on the J-V curve:

$$P_{MPP} = V_{MPP} \times I_{MPP} \quad (2.3)$$

The fill factor (FF) is a relation between the power of the device at the MPP and the theoretical value, determined by the  $V_{OC}$  and  $J_{SC}$  of the PV cell:

$$FF = \frac{P_{MPP}}{P_{max}} = \frac{V_{MPP} \times I_{MPP}}{V_{OC} \times I_{SC}} \quad (2.4)$$

The power conversion efficiency ( $\eta$  or PCE) of the PV cell is then calculated as electrical power produced by the device divided by the power of incident light ( $P_{light}$ ) irradiating the device area, which combines with Equ. 2.4 resulting in:

$$\eta = \frac{P_{OUT}}{P_{IN}} = \frac{P_{MPP}}{P_{light}} = \frac{V_{MPP} \times I_{MPP}}{P_{light}} = \frac{V_{OC} \times I_{SC} \times FF}{P_{light}} \quad (2.5)$$

The highest PCE is then achieved for an ideal solar cell with a FF approaching 100%,  $R_S$  of zero and  $R_{SH}$  close to infinity. However, in reality,  $R_S$  and  $R_{SH}$  never reach their ideal values and recombination processes within the PV device reduce the FF. As a result, low shunt resistance displaces the J-V curve proportionally to higher currents, whereas high series resistance shifts the J-V curve to lower voltages [95].

There are fundamental differences between the energetic band properties of organic and inorganic semiconductors, therefore, the photo excitation in organic semiconductors does not

immediately lead to the generation of free charge carriers at room temperature, as is the case for inorganic semiconductors, due to the tight coulombic attraction of the Frenkel exciton. Moreover, the transport properties and loss mechanisms of charge carriers differ for both semiconductor types. The circuit model used for inorganic PVs, can nevertheless be used to describe the characteristics of OPV devices and thus, all equations and fundamental figures of merit for traditional inorganic PVs can be used for describing the behavior of OPVs [101]. However, attention is required when analyzing the

$$V_{OC} = |E_D(HOMO)| - |E_A(LUMO)| - 0.3 \text{ eV} \quad (2.6)$$

where the 0.3 eV is an empirical factor due to the difference between the  $V_{BI}$  and the actual device  $V_{OC}$ . The origin of the 0.3 eV loss is still a debated topic and no clear explanation for it has been found yet. Electrical characteristics of OPV-based devices, as factors that affect the  $V_{OC}$ ,  $J_{SC}$ , FF,  $R_s$ , and  $R_{SH}$  may vary due to the intrinsic properties of organic semiconductors, especially in a D/A BHJ system which is fundamentally different from the typical p-n junction in inorganic semiconductors. The open circuit voltage  $V_{OC}$  of an OPV-based devices is dependent on the type of contact formed between the electrodes and the BHJ layer. For a non-ohmic contact, described by Mihailtechi *et al.* experimentally proved that the  $V_{OC}$  matches the work function difference between the electrodes, as expected from the MIM model. On the other hand, assuming the presence of an ohmic contact, the maximum theoretical value of the  $V_{OC}$  for BHJ systems, namely the built in potential  $V_{BI}$ , can be obtained (described as the difference between the donor HOMO level and the acceptor LUMO level). For ohmic-contacts at the electrodes, Mihailtechi *et al.* reported a very low variation of the  $V_{OC}$  of the negative electrode work function. Regardless of the electrode material used (Ca (W.F=2.9 eV) or Au (W.F=5.1 eV)), the  $V_{OC}$  alteration was of only 160 meV. This effect was explained by the pinning of the electrode Fermi level to the redox potential of the fullerene material in the BHJ [102]. As 1.7 eV–2.1 eV is the typical optical band gap of light harvesting organic semiconductors, it is reasonable to expect a similar value for the  $V_{OC}$  of an OPV device [103]. In reality, however, the  $V_{OC}$  is often nearly two times lower than the  $E_{opt}$ . This reduction is due to various factors and loss mechanisms: recombination processes, temperature, light intensity, energetic disorder, defect states, CT states, D/A morphology, and interface area, which are reviewed in detail elsewhere [103][102][104]. Nevertheless, a good empirical estimation of the  $V_{OC}$  value for OPV-based solar cells given by Scharber *et al.* in 2006, still applies [104]. Nevertheless, according to Equ. 2.6, the device  $V_{OC}$  can be increased with the use of a tailored

synthesis of novel acceptor materials with a LUMO level closer to the vacuum energy (assuming that the HOMO level of the donor material is constant) [105][106][107][108]. The short circuit current  $J_{SC}$  is strongly dependent on the optical and electrical characteristics of the D and A materials used for the BHJ photoactive layer. Some of the factors that need to be considered for achieving high  $J_{SC}$  yields and therefore efficient OPV-based devices are: the choice of energetically and optically matching D and A materials; the area of the D/A interfacial contact in the BHJ; and the thickness and morphology of the photoactive layer. In this regard, increasing the BHJ thickness and tailoring the optical band gap to increase the harvest of photons from the solar spectrum, has been shown to successfully improve the  $J_{SC}$  of OPV based devices [101]. Further enhancement can be achieved with an intelligent selection of the BHJ solvent type, the deposition method, and the fabrication conditions [109][110]. Special attention has to be devoted in order to reduce recombination processes in the BHJ or at interfaces within the device stack due to thick BHJ layers and low charge carrier mobility, which usually reduce the  $J_{SC}$  [111]. The series resistance  $R_S$  in both inorganic and organic PV cells is attributed to the bulk resistance of the photoactive layer, the resistance of the electrodes and interfacial layers, the contact resistance at any functional interface in the device stack, and the measuring probe resistance. In OPV-based devices, the  $R_S$  is additionally dependent on the electric field strength within the stack, whereas in traditional p-n junction solar cell models, the  $R_S$  is independent on the applied voltage as previously shown in Equ. 2.2 [112][113]. This dependence originates from the fact that organic semiconductors exhibit field dependent mobilities [100]. In other words, in organic semiconductors high mobilities are recorded at high voltages and thus  $R_S$  decreases with increasing voltage. As a result, the most accurate measurement of  $R_S$  is conducted by evaluating the differential resistance  $dV/dJ$  of the J-V slope near the  $V_{OC}$  of the device obtained in the dark [114]. Furthermore, the series resistance is dependent on the D and A characteristics (*i.e.* regio-regularity, molecular packing, and crystallinity) and the phase separation of the BHJ [115]. The length of the photocurrent extraction path towards the electrodes (when bigger than  $1 \text{ cm}^2$ ) greatly increases the  $R_S$  when TCOs such as ITO are used [116][117]. This originates from the fact that TCO conductivities are often greater than an order of magnitude lesser than typical conductivities of metals [114][118]. Analytical models and guidelines to design large-area OPVs have also been published [119][120][121][122]. The shunt resistance  $R_{SH}$ , on the other hand, describes current leakages in the solar cell such as current leakage between the photoactive layer and the electrodes due to presence of pinholes, or current leakage induced by impurities in the device. Defects on the surface of materials have been reported to serve as recombination centers for

free charge carriers [123]. Another study conducted by Kim *et al.* suggested that there are three reasons for the  $R_{SH}$  of P3HT:PCBM based OPVs: the photoactive layer thickness; the interface between the photoactive film and the electrodes; and the illumination intensity [125]. In this regard, the use of interfacial layers improves  $R_{SH}$  by defining the polarity of the device and assuring a selective charge carrier transport towards the electrodes. An increased  $R_{SH}$  due to prevention of Al diffusion into the photoactive blend and reducing the surface roughness at the interface has also been observed [101]. Ultimately, the majority of studies in the literature use a similar method to evaluate the  $R_{SH}$ : calculating it from the inverse slope of the J-V curve in the dark near the  $J_{SC}$  [124]. The fill factor FF appears to be the most sensitive of all the characteristic parameters of OPV devices, due to its complex dependence on various factors such as the fabrication conditions, the device area, the electrode materials, the thickness and morphology of the BHJ, the recombination losses in the BHJ and at interfaces between layers in the device stack, and the type of metal contact [101][125]. A suitable energetic alignment between the layers in the device structure is also important in order to avoid J-V curves with a characteristic “s-shape”, which drastically reduces the FF [126][127][126][128]. Effectively, the FF is strongly dependent on the  $R_S$  and  $R_{SH}$  of the device, which furthermore depend on many of the above mentioned factors [115][101].

P-type organic semiconductors such as conjugated small molecules and conjugated polymers can be efficiently used as electron donating materials. Detailed reviews of the chemistry and their synthesis, can be found elsewhere [129][130][131]. A good summary of current developments on the field of p-type small molecules has been published by Dou *et al.* and Kang *et al.*, [86][132]. Generally, the structure of a conjugated polymer is determined by three main components: backbone, side chains, and substituents [133]. From these, the conjugated backbone is the vital component as it defines the physical properties of the polymer. For example, homo polymers commonly have optical band gaps above 1.9 eV, due to steric hindrance associated with the repeating single aromatic unit or fused aromatic units of the conjugated backbone [133]. Instead, the optical band gap can be reduced notably after an internal charge transfer when a repetition of polymers with an electron-rich and electron-deficient moieties are used to construct the backbone [133]. In this respect, depending on the optical band gap of the polymer, p-type donor materials are generally divided into two classes: wide band gap D materials ( $E_{opt} > 1.7\text{eV}$ ) and low band gap D materials ( $E_{opt} < 1.7\text{eV}$ ). The characteristics of some low band gap polymers can be further tailored to absorb the near infrared (NIR) region of the solar spectrum. Narrowing the optical band gap of an organic

semiconductor allows for greater light absorption, which in turn leads to an increased exciton yield and charge carrier generation. In a D/A BHJ this means that higher  $J_{SC}$  values are achieved for narrower (lower)  $E_{opt}$  of the organic semiconductors, whereas deepening the HOMO level of the D (or increasing the EA of the A) improves the device  $V_{OC}$ . This can be accomplished by utilizing alternating D/A-type co-polymers to construct the backbone of the donor material. Extensive research has been conducted in the last decade, leading to the synthesis of countless novel p-type semiconductors based on donor and acceptor moieties such as benzothiadiazole (BT), benzodithiophene (BDT), cyclopentadithiophene (CPDT), diketopyrrolopyrrole (DPP), dithienosilole (DTS), dithienogermole (DTG), thienopyrroledione (TPD) and thienothiophene (TT) are the commonly used electron donor materials [86][132].

One of the first successful uses of the BT and carbazole units in a co-polymer was accomplished with the synthesis of PCDTBT (poly [9'-hepta-decanyl-2,7-carbazole-alt-5,5-(4',7'-di-2-thienyl-2',1',3' benzo-thiadiazole)), shown in Fig. 2.7(b)) by Leclerc's group [134]. At the time, PCDTBT-based OPV devices exhibited high  $V_{OC}$  of 0.89 V, owing to the low-lying HOMO level of the material (-5.5 eV). Exciton separation in organic semiconductors takes place at the D/A interface in the photoactive layer, therefore, the role of n-type materials for efficient charge generation in OPV devices, is equally important to the role of the donor material. A distinction can be drawn between fullerene and non-fullerene based n-type organic semiconductors. The latter can be divided into polymers and small molecules, whereas the former is represented by derivatives of the  $C_{60}$  and  $C_{70}$  molecules. In this thesis, only the properties of fullerene based acceptors are discussed, due to their relevance to the scope of this work. Information on the development of non-fullerene acceptors can be found elsewhere [135][136]. The  $C_{60}$  and  $C_{70}$  fullerenes (Buckminster fullerenes) are considered to be the third allotrope of carbon [137][138][139]. These molecules were discovered by Kroto, Smalley, and Curl, who were awarded the 1996 Nobel Prize in Chemistry "for their discovery of fullerenes". The chemical structures of  $C_{60}$  and  $C_{70}$  consist of a conjugation between 60 or 70  $\pi$  electrons that results in a system exhibiting a high electron affinity. This characteristic of the fullerenes was associated to a low-lying LUMO level (approximately -4.3eV).  $C_{70}$  showed a better absorption than  $C_{60}$ , due to the asymmetric nature of the molecule. As a result, both fullerenes were used as acceptor materials at the early years of OPV-based solar cells. However,  $C_{60}$  and  $C_{70}$  exhibit poor solubility in common solvents, and high crystallization tendency. Therefore, the fullerenes had to be modified in order to overcome these drawbacks [140].

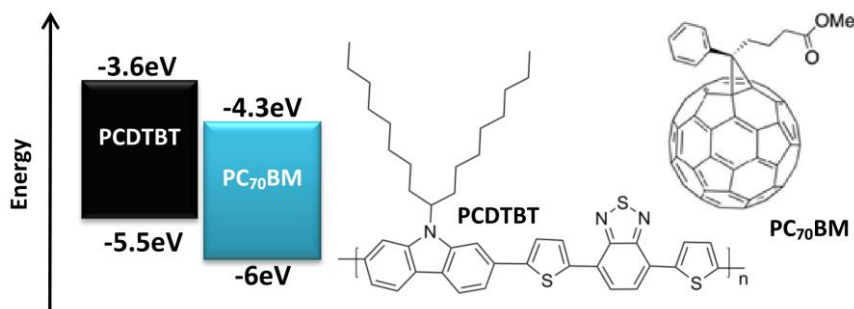


**Figure 2.7: (a) Band energy diagram for PCDTBT: PC70BM and (b) the chemical structure for both PCDTBT and PC70BM.**

Another significant advantage of PCDTBT as an active layer material is the chemical stability of the polymer material. This has allowed PCDTBT devices to be fabricated in air via both an inkjet printing method and a spray coating method with minimal losses in efficiency [124][125]. This makes PCDTBT a more promising candidate for scale up to large area devices [122]. The chemical stability of PCDTBT also leads to an increase in device lifetime for encapsulated devices, after the initial burn in period seen in polymer solar cells [141]. Devices have been extrapolated to a lifetime of 6.2 years on average, in comparison to P3HT devices which are extrapolated to last for 3.1 years. It is noted that these devices are under constant illumination at one sun's intensity, and assuming 5.5 hours of sun light at one sun intensity per day, 365 days a year [141]. This material is considered as suitable for rGO devices to be an alternative to commonly used bathocuproine (BCP) (LUMO at -3.5 eV) as electron transport layer (ETL). The first successful use of a functionalized C<sub>60</sub> fullerene was reported in 1995, when the group of Heeger *et al.* used PC60BM ([6,6]-Phenyl C 60 butyric acid methyl ester), synthesized by Wudl *et al.*) as an acceptor for the first reported BHJ-based OPV device [27][142][143]. PC60BM has a LUMO level of approximately -3.9 eV, good solubility and relatively high electron mobility of 10<sup>-3</sup> cm<sup>2</sup> V<sup>-1</sup> s<sup>-1</sup> [144]. However, a major drawback of PC60BM is poor absorption of light in the visible wavelengths, owed to the high symmetry of the C<sub>60</sub> molecule. In order to overcome this limitation, Janssen *et al.* synthesized the PC70BM molecule, as shown in Figure 2.7(b). The synthesized molecule exhibited higher absorption in the wavelengths 350 nm–500 nm than PC60BM does [145]. Nowadays, due to its higher absorption PC70BM is prevalently used as acceptor in blends with low band gap donors, which leads to improved device JSC. Despite this obvious advantage, PC 70BM is more expensive than PC 60BM because of the long purification process required to yield C<sub>70</sub> [143]. Nevertheless, PC 60BM and PC 70BM are still the most commonly used fullerene acceptors for OPV devices Finding alternatives to PCBM (hereafter used to represent both PC60BM and

PC 70BM) appear to be difficult. Ideally, new acceptor materials should exhibit high absorption in the visible region, sufficient electron mobility, and high EA. Additionally, the LUMO level of the acceptor has to be energetically positioned to match the LUMO level of the donor, in order to facilitate efficient exciton dissociation at the D/A interface, whereas the difference between the LUMO of the acceptor and the HOMO of the donor should be kept as large as possible in order to yield high device  $V_{OC}$  values. Therefore, acceptors with LUMO levels that are higher than those of PCBM are needed, in order to improve the PCE of P3HT-based OPV systems by increasing the device  $V_{OC}$ . Because of the superlative properties for PC70BM over PC60BM, as mentioned above in this work PC70BM is used as the electron acceptor material for the OPV.

### *2.3.4 Interfacial layers for OPV devices*

The utilization of interfacial layers (IFLs) in the OPV stack plays an essential role as it leads to performance and stability improvements. This originates from the various functionalities of the IFLs such as: improving the energy alignment between the photoactive layer and the electrodes; forming a selective contact for free charge carriers; affecting the morphological formation of the photoactive layer; prohibiting a chemical or physical reaction between the D/A materials and the electrode; and acting as an optical spacer for better light distribution within the device [146][147]. Generally, IFLs can be divided into inorganic and organic-based ones, depending on the materials used. Taking into consideration the electronic properties of the materials, they can be further distinguished between conducting, semi-conducting, and dipole IFLs. A mixture of at least two of the above mentioned IFL types can be defined as a composite IFL. The following sections solely give an overview of IFL suitable for the fabrication of OPV devices.

Metals are known for their high conductivity. Thin layers (< 30 nm) of thermally evaporated metals appear transparent and can serve as interfacial layers. For instance, Calcium (Ca) with low work function is commonly used to modify the electrode work function and accomplish an ohmic contact between the BHJ and the electrode. However, low work function materials tend to oxidize easily in ambient conditions, and chemically transfer to insulating metal oxides that cause reduction of the device performance. Besides, they cannot be easily solution processed and are more useful for research purposes than for application in industry. This class of interfacial layers include numerous semiconducting ceramics, most of which are known as transition metal oxide materials (MeOx). They offer a wide range of advantages over

solely metal-based IFLs [148]. Semiconductors are n-type and p-type, according to the charge carrier excess in the material (free electrons for n-type or holes for p-type). The presence of a band gap improves the charge selectivity of the contacts, while modifying the electrode work function to allow a facile transfer of free charge carriers. Additionally, MeO<sub>x</sub> exhibit high transparency in the visible spectrum due to wide optical band gaps, and can be easily solution processed over large areas.

Zinc oxide (ZnO) is a commonly used n-type interfacial material [149][150][151][152][153]. Due to its high electron mobility, ZnO is ideal as an electron selective contact layer [128][154]. Moreover, ZnO films exhibit high optical transmittance in the visible range (>90%) and can be deposited at a low cost by various coating techniques, which makes it an ideal electron transporting layer (ETL) for OPV cells [155][156]. There are many different ZnO-based materials available on the market. Depending on the processing temperature required for the deposition of ZnO, the available ZnO samples can be generally divided into R2R compatible and R2R incompatible. In this regard, there are three main solution based deposition methods: an extensively investigated sol-gel process [156][157][158]; a nanoparticles approach (NPs) [159][149][150][160][161]; and approaches that require a ZnO-precursor to be annealed in air in order to convert to ZnO hydrolysis [124][162]. Detailed information about the advantages and disadvantages of the different fabrication techniques for ZnO can be found in comprehensive reviews elsewhere [153]. Titanium oxide (TiO<sub>x</sub>) is another commonly used MeO<sub>x</sub>, which is a good alternative to ZnO [163][164][165][166]. TiO<sub>x</sub> can be efficiently used as an ETL, due to its good electron collecting ability and transparency in the visible range [167][168]. Commonly reported in the literature is the use of titanium isopropoxide or suboxide [168][169][170]. These titania precursors are usually in a liquid phase which allows for an ease application in a sol-gel or dilution process [167][171]. Detailed information about the different application methods and ETL characteristics can be obtained from reviews prepared by Park *et al.* and Steim *et al.*, [146][172]. Tin oxide (SnO<sub>x</sub>) and niobium oxide (NbO<sub>x</sub>) have also been reported to act as ETLs, however their application in OPV devices is limited due to their high processing temperatures and adverse characteristics compared to ZnO and TiO<sub>x</sub> [173][174][175][176]. Molybdenum oxide (MoO<sub>x</sub>) is probably one of the most used p-type metal oxide for OPV applications. This is because of the high transparency of the material (in the visible spectrum), and deep lying Fermi level, which is nearer to the conduction band of the material, making MoO<sub>x</sub> a good choice as an efficient hole transport layer (HTL) and electron blocking layer towards the anode. MoO<sub>x</sub> is also processable from solution at low

temperatures using various techniques such as sol-gel, spray-pyrolysis deposition, wet-deposition, and NPs approaches [177][108][178][179][180][181][182]. MoO<sub>x</sub> films can also be obtained at room temperatures [183][184]. Vanadium pentoxide (V<sub>2</sub>O<sub>5</sub>) has similar characteristics to MoO<sub>x</sub>. Therefore, this material is also often used as a HTL in OPVs. There are many published reports of different deposition techniques such as sol-gel processing, NPs approaches, and low temperature wet processing [153][185][186][187][188]. Nickel oxide (NiO<sub>x</sub>), tungsten oxide (WO<sub>x</sub>), and copper oxide (CuO<sub>x</sub>) have also found use as HTL due to their similar opto-electric characteristics to other p-type semiconductors [189][184][108]. Organic polymers ( $\pi$ -conjugated or not) and small molecules can also be used to improve the charge carrier transport from the BHJ towards a desired electrode, or to modify the work function of an electrode in order to accomplish an ohmic contact between it and the photoactive layer of OPV cells. One main advantage of organic IFLs over their inorganic counterparts is the versatility of possible material combinations, which allows for the fine adjustment of the characteristics of the IFL. This can be used to accomplish a desired orientation of the IFL used, which can induce the formation of permanent interfacial dipoles and alter the work function of the electrode [132]. There are only a few reports detailing n-type doping of polymers for use as IFLs for OPV devices. A good review on the field was conducted by Walzer *et al.*, [190]. Fullerene based n type small molecules, on the other hand, are widely used as IFLs. A good review of the field can be found elsewhere [191]. Other n-type small molecules such as bathocuproine (BCP) and bathophenanthroline (BPhen), are commonly used as ETLs (and HBLs) in the OPV (and OLED) community [117][146][192]. Poly(3,4-ethylenedioxythiophene) (PEDOT) is a widely used and extensively investigated p-type conductive polymer. Due to its low band gap (1.6 eV – 1.7 eV), high optical transparency, and environmental stability, PEDOT is used for diverse applications such as a hole injection layer in OLEDs, and as a flexible electrode in organic electronics. Nevertheless, to improve the solubility characteristics of PEDOT, polystyrenesulfonate (PSS) is commonly used in combination with PEDOT [193]. The resulting organic compound, is furthermore widely used as a hole selective contact and a standard HTL in OPV devices. However, PEDOT:PSS exhibits low conductivity of typically  $10^{-5}$  S cm<sup>-1</sup> to 10 S cm<sup>-1</sup>. The conductivity can be increased by simple film treatments with methanol (MeOH;  $\sigma$  of 1362 S cm<sup>-1</sup>); the addition of solvents like dimethylsulfoxide (DMSO;  $\sigma$  of 1418 S cm<sup>-1</sup>) with high boiling point, or ionic liquids such as 1-ethyl-3-methylimidazolium tetracyanoborate (EMIM TCB;  $\sigma$  of 2084 S cm<sup>-1</sup>) [193][194][195]. Nevertheless, PEDOT:PSS exhibits an intrinsically acidic and hydroscopic character, which causes the degradation of OPV devices. There are several comprehensive

## Literature Review

---

reviews of water/alcohol soluble conjugated and non-conjugated polymers that can be used as IFLs [196][197][198]. Generally, a significant device performance enhancement can be achieved by the use of polyfluorene-based conjugated materials such as poly[9,9-bis(6'-(18-crown-6) methoxy)hexyl) fluorene] chelating to potassium ion (PFCn6:K<sup>+</sup>) or poly[(9,9-bis(3'-(N,N dimethylamino)propyl)-2,7-fluorene)-alt-2,7-(9,9-dioctylfluorene)](PFN) [199][200][201][202]. Some relevant examples of non-conjugated polymers are polyethylenimine ethoxylated (PEIE), polyethyleneimine (PEI), and polyallylamine (PAA).[203][204] Generally, films formed from non-conjugated polymers are very sensitive to film thickness, due to their large band gap and insulating character, compared to conjugated polymers. Another approach to efficiently modify the electrode work function is the use of self-assembled monolayers (SAM) of small molecules. In this regard, device performances can be enhanced by modifying the electrode work function with 4-chlorobenzenesulfonyl chloride (CBS), chlorobenzoic acid (CBA), 4-chlorophenyldichlorophosphate (CBP), 4-chlorobenzoylchloride (CBC), or with SAMs containing a -NH<sub>2</sub>, -CH<sub>3</sub>, or -CF<sub>3</sub> terminal groups [205][206][207][208]. Recently, a novel non-conjugated small-molecule electrolyte named 4,4'-(((methyl(4-sulphonatobutyl)ammonio)bis(propane-3,1-diyl))bis(dimethyl-ammonium-diyl))bis-(butane-1-sulphonate) (MSAPBS) was shown to efficiently serve the purpose of an IFL, and an OPV device PCE above 10% was reported [209].

The number of publications reporting on IFLs formed from a composite of two compounds (inorganic and/or organic) has increased over the years. Composite IFLs often consist of a mixture between a metal oxide and an inorganic or organic counterpart. In this respect, high device performance characteristics were reported for a ZnO-TiO<sub>x</sub> mixture [210]. In another approach, ZnO was doped with cesium (Cs) leading to a smoother IFL surface and reduced bulk resistance [211]. Small *et al.*, on the other hand, reported enhanced device J<sub>SC</sub> values after adding poly(vinyl pyrrolidone) (PVP) to a sol-gel ZnO, which caused an improved contact between the ZnO nanoclusters and PCBM [159]. Hybrid composites between metal oxides and reduced graphene oxide (RGO) are also possible, and lead to PCE improvements due to reduced device R<sub>s</sub> and improved IFL conductivity as recently shown by Beliatas *et al.*, [212]. Similar approaches were also reported by others [213]. Other hybrid composites are metal oxides with incorporated metal NPs [181][214]. Organic IFLs such as PEDOT:PSS have also been used in combination with MeO<sub>x</sub> [213][215]. The incorporation of Ag and Au NPs, or even a combination of both, mixed with PEDOT:PSS is another method to improve device

functioning and is often credited with improving the electrical properties of the IFL [216][217][218][219][220].

The electrodes of any OPV device embody an essential component in its stack, as they collect the free charges that are generated and enable contact with an external circuit. In this regard, electrons are collected at the electron selective contact named cathode, and holes are collected at the hole selective contact named anode. To accomplish an efficient charge transport with few losses, the ideal electrode should show low sheet resistance ( $RS_{HEET} < 10 \Omega/$ ) and thus high conductivity [221]. There are many materials exhibiting these characteristics, which can be efficiently utilised as electrodes. However, in OPVs light has to reach the photoactive layer through one, and ideally both electrodes, in order to generate charge carriers. Therefore, it is very important that at least one of the electrodes exhibits high transparency. The opto-electrical characteristics mentioned above are possible for electrically conducting ceramics (doped metal oxides), also known as transparent conductive oxides (TCOs). A typical example of this type of materials is ITO, which usually has a  $RS_{HEET}$  between  $15 \Omega/\square$  and  $75 \Omega/\square$  and a transparency of above 90% in the visible spectrum. The resistivity of the TCO is important and has to be kept low at all times. Otherwise, the device performance decreases for extended conduction paths (above 1 cm), due to reduced  $J_{SC}$  and FF values owed to non-geminate recombination processes [100][117][118][222]. Unfortunately, high quality ITO is very expensive and contains indium, which is limited in supply. Additionally, ITO is not solution processable and does not have sufficient flexibility for certain fabrication applications on plastic substrates [223]. Therefore, numerous alternatives to ITO as a bottom electrode have been studied. In this respect, highly conductive polymers alone or in combination with metal grids have also been shown to overcome the conductivity limitations of ITO [194][195][172][224][225]. Carbon nanotubes (CNTs) and graphene are other promising materials, due to their low-cost and uncomplicated fabrication [226][227][228][229][230]. OPVs also have a top electrode. In research laboratories it is usually deposited by vacuum thermal evaporation of Al or Ag, whereas printing and coating techniques are more common in industry due to the possibility of fast deposition with unlimited design layouts. In this regard, Ag-based inks are exclusively used in industry, despite recent advances that allow for the fabrication of carbon-based electrode systems [231]. Given the possibility to replace ITO as a bottom electrode and/or evaporated metal top electrodes, the fabrication of large area solar cells (aperture of at least  $1 \text{ cm}^2$ ) can be easily achieved using R2R fabrication techniques on plastic substrates.

### 2.4 Device Architectures

#### 2.4.1 DSSC architecture

Instead of Pt, a number of carbon based materials [232] including graphene related materials [16][17][18][233][234][235] have been tested as alternative CE materials which exhibited excellent conductivity and high electro-catalytic activity. Even though the efficiencies of DSSCs with graphene related materials (graphene obtained through electrophoretic deposition [16] and graphene with incorporation of SiO<sub>2</sub> nanoparticles [17] as CE materials are high (5.69% [16] and 4.04% [17]), the fabrication of devices involve complex process steps and therefore require optimization of a number of process parameters. In another important work [18] the efficiency of DSSC with photothermal reduced graphene oxide (P-rGO) as CE was 7.62%, the method used for fabricating the final CE may not be suitable for realizing large area CEs. In the case of graphene based composites as CE materials in DSSCs, it is difficult to understand and control the electrochemical activity at the electrode/electrolyte interface. However, graphene ink [19] spray coated on FTO substrates was recently used as a CE in fabricating large-area DSSC modules via the spray coating technique. In this case, the electrochemical activity at the electrode/electrolyte interface could be easily explained. Additionally, using a CE composed of graphene nanoplatelets (GNP), in the structure FTO/Au/GNP, produced a DSSC with a record efficiency of over 14% [20], outperforming a similar FTO/Pt CE DSSC. In both cases, the electrolyte was a cobalt(III/II) tris(1,10-phenanthroline) complex ([Co(phen)<sub>3</sub><sup>3+/2+</sup>]) transition metal redox couple system with TiO<sub>2</sub> electrodes co-photosensitized with a strongly anchored alkoxysilyl-dye (ADEKA-1) and a carboxyorganic dye (LEG4). Figure 2.8(top) (next page) shows the schematic of DSSC used in this thesis, A DSSC typically consists of a photo-anode, an electrolyte with a redox species (such as iodide/tri-iodide (I<sup>-</sup>/I<sub>3</sub><sup>-</sup>) in an organic solvent), and a counter electrode (CE). The anode consists of a transparent conducting oxide (TCO) coated glass substrate in this work fluorine-doped tin oxide (FTO) is used, with a deposited mesoporous network of wide band gap metal oxide semiconductor, such as nanosized TiO<sub>2</sub> particles, which is sensitized with a suitable dye like purified cis-bis (isothiocyanato) bis (2,2'-bipyridyl-4,4'-dicarboxylato) ruthenium (II)-bis-tetrabutylammonium dye solution (N719), which absorbs a photon (Energy =  $h\nu$ ), injects an electron into the conduction band of TiO<sub>2</sub> and travels to the FTO front electrode. The redox couple the liquid electrolyte which was prepared by mixing 1-butyl-3-methylimidazoliumiodide (BMII, 0.5 M), lithium iodide (LiI, 0.1 M), Iodine (I<sub>2</sub>, 0.05 M), guanidinetiocyante (GuNC, 0.1 M), and ter-butylpyridine (tBP, 0.5 M) in acetonitrile works

## Literature Review

as a mediator which transfers electrons from the cathode to the oxidized dye molecules.  $I^-$  ions reduce the sensitizer and oxidize to  $I_3^-$  ions while the monovalent  $I^-$  ions are recovered at the cathode prepared by spray coating of Solar reduced graphene oxide (SRGO). As shown in the energy level diagram Fig. 2.8(bottom) The energy difference between the Fermi level ( $E_F$ ) of  $TiO_2$  and the redox potential ( $I_3^-/I^-$ ) of the electrolyte results in open circuit voltage ( $V_{OC}$ ) of the fabricated DSSC.

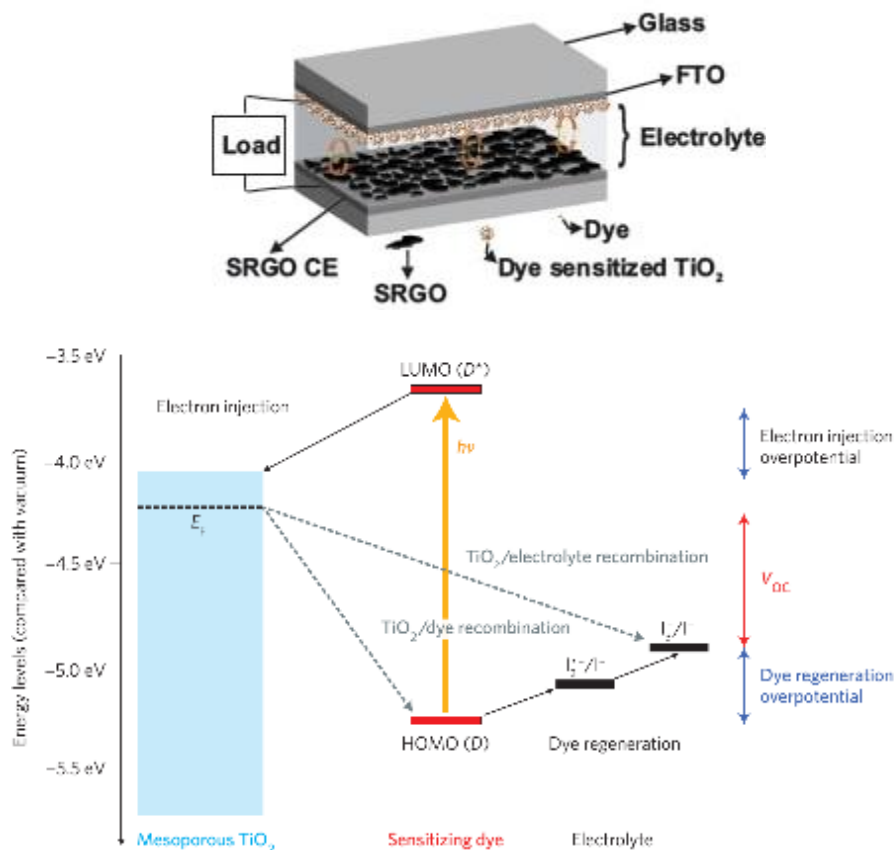


**Figure 2.8: (top) Dye-sensitized solar cell device schematic and (bottom) DSSC operation.**

### 2.4.2 OPV device architecture

A great deal of work has been devoted over the past decades to investigate OPV devices comprising a regular stack geometry. In this architecture (Fig. 2.9 (left)) the anode is commonly ITO, functionalized by an organic HTL made of PEDOT:PSS. To enhance the electron extraction towards the cathode, while forming an ohmic contact with the photoactive layer, a low work function metal, *i.e.* Ca, is generally used as an IFL. The outermost or top electrode (the cathode) is commonly formed by Al. However, there are a number of issues associated with the use of Ca as the ETL. Due to its low work function of 2.87 eV, Ca is air and water

sensitive making it only suitable for processing in an inert atmosphere [22][236]. Instead of Ca, thin layers of n-type organic materials ( $\sim 5$  nm) such as BCP can be used. However, in both cases an expensive and time consuming thermal-vacuum evaporation process is required for the ETL deposition. Metal oxides such as ZnO and  $\text{TiO}_x$  are less reactive with air and humidity than Ca, and therefore they can be used as efficient ETLs. Moreover, most  $\text{MeO}_x$  used in OPV devices are solution processable under ambient conditions, due to their improved air stability over Ca [166][25][26]. Nevertheless, care must be taken in the selection of deposition solvents so that orthogonality and good wetting on top of the BHJ layer is maintained. Similar considerations apply also for ETLs other than  $\text{MeO}_x$ , whenever a deposition from a solution is done.

As mentioned, a main responsibility of IFLs is to adjust the electrodes' work function, in order to accomplish a suitable energy alignment between layers in the device stack. Thus, Fig. 2.9(right) shows the energy band diagram of a typical OPV cell with a standard architecture. It can be seen, that the ITO work function of  $-4.7$  eV can be modified by PEDOT:PSS, which effectively changes the contact work function to approximately  $-5.1$  eV. By doing this, the electrode work function is brought closer to the HOMO level of PCDTBT, in order to ease hole transport towards the ITO electrode, which becomes the anode. In a similar manner, as can be seen in Fig. 2.9(right), the work function of rGO ( $\sim -4.2$  eV) is positioned above the LUMO of PC70BM, allowing for the formation of an ohmic contact with the Al electrode which defines Al as the cathode of the cell.

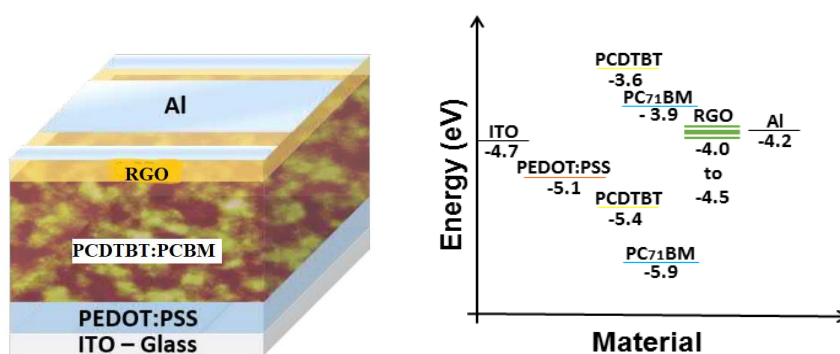


**Figure 2.9: (left) Schematic diagram of a regular/standard device geometry and (right) the corresponding energy diagram for the device stack.**

### 2.5 Graphenaceous Materials as Counter Electrodes in DSSC

Low cost, high surface area, and high electric conductivity are the benefits of using conventional carbon materials in DSSCs as CEs. Due to considerable electrochemical activity

and high conductivity [237] comparable to Pt, carbon nanofibers [238], carbon nanotubes [239][18], carbon black [240], and mesoporous carbon [241] were under a great deal of research interest in the recent years. Professor Grätzel's group initially started developing low-cost Pt-free carbonaceous CEs[242], they showed PCE of 6.67% in DSSC by using high-surface area carbon black ( $C_b$ ) composited with functionalized graphite, where the use of  $C_b$  increased the catalytic effect while the electronic conduction was enhanced by Graphite to get the desired Sheet resistance ( $R_{sq}$ ), further the higher record PEC for DSSCs with conventional carbon CEs of 9.1% was made possible by utilizing nanometer-sized  $C_b$  to prepare CEs [240]. other than  $C_b$ , excellent catalytic activity for  $I_3^-$  reduction was reported in the literature for mesoporous carbon (MC) due to which PEC of 7.5% on optimization of porosity during the synthesis process [241]. It is also reported that 20.7% PEC (8.63%) improvement was observed using an all-carbon CE instead of conventional Pt electrode [54]. Other than carbon black and mesoporous carbon considerable attention been attracted by CNTs, since they possess distinctive properties due to variety of structures, Teflon membrane filter deposited by Single-wall CNTs (SWCNTs) by filtration also showed sheet resistance ( $R_{sq}$ ) of  $1.8 \Omega \text{ sq}^{-1}$ , which exhibited 4.5% PEC when used as CE in DSSC, while 7.6% PCE was reported when fluorine doped tin oxide (FTO) spray coated with multi-wall CNTs (MWCNTs) was used as CE [243], 8.3% PEC was reported when screen printed CNTs were utilized as CEs, while highest PEC of 10.04% with CNTs was reported when CEs prepared by growing CNTs on FTO using chemical vapor deposition (CVD) technique [244]. These results indicates, that fabrication process of CE is vital step for use of CNTs. Like above mentioned carbon materials, Graphene exhibited better regeneration of  $I_3^-/\Gamma^-$  in an ionic liquid [245], it showed superior restoration of the redox couple (from  $I_3$  to  $\Gamma^-$ ) than the traditional organic solvents the catalytic activity observed to increase with the increase in edge oxygen functional group defects [246]. It was observed that the catalytic activity can be varied by varying the functionalization of graphene, indicated by C/O ratio, PEC value nearer to DSSC with Pt CE (5.5%), approximately 5% was reported by using functionalized graphene sheets as CE upon optimization the C/O ratio [247]. However, when the oxygen content was too high conductivity of graphene dramatically decreased[248][247][249]. Doping or co-doping heteroatoms (S[250], F[251], N[252][253], B [254][255]) is another approach to increases the catalytic activity with minimal loss in conductivity[256][257]. For example, 7.07% PCE value for DSSC was reported by using 3-dimensional N-doped graphene foams (N-GFs) as CE material, this value is close to control DSSC with Pt-CE (7.44%), to maintain the conductivity, Xue et al., graphene oxide foams (GOF) prepared by freeze-drying is further annealed in the presence of ammonia to dope N

atoms [258], the DSSC showed PCE greater than that of a reference cell with an un doped graphene electrode (4.84%). Using graphene decorated by nitrogen containing polyelectrolyte like diallyldimethylammonium chloride (PDDA) also observed to have enhanced the catalytic activity of the CE, using PDDA decorated Graphene layered thin film Xu et al., reported higher PCE for DSSCs (9.54%) than that of DSSC with Pt CE (9.14%) control cell. The catalytic activity of graphene was found to be very well suitable for higher redox potential system like  $\text{Co}(\text{bpy})_3^{3+/2+}$  these Co mediated electrolytes showed upto 12.3% PCE when used in conventional DSSCs with Pt-CE [259][260][261][262][241]. The DSSCs fabricated with solution processed graphene electrodes showed low charge transfer resistance ( $R_{CT}=3.3 \Omega \text{ cm}^2$ ) at the graphene/electrolyte interface when compared to Pt-electrode ( $R_{CT}=5.5 \Omega \text{ cm}^2$ ), hence the former DSSCs exhibited higher PCE (9.4%) than that of the DSSC with Pt-CE (8.2%) under the same fabrication and experimental conditions by Kavan et al. [263][246]. Ju et al., reported higher PCE than 10% with film of nitrogen-doped graphene nano platelet CE [264][265]. To prepare semitransparent DSSCs Pt-Graphene hybrid films (~ 80% transmittance) were used [266], utilizing these films as electrodes, upon illumination PCE of 6.55% (front side) and 5.17% (rear sides) was reported by Dao et al., and by increasing the Pt percentage in the hybrid films, an enhanced PCE values of 8.0% (front side) and 7.0% (rear sides) were reported by Shih et al., [267]. Graphene ribbons [268], carbon nanotubes [269], graphene with polymer composite [54] and graphene fibers [270] were also used to fabricate flexible DSSCs. PCE value of 6.05% for DSSCs with all-carbon flexible electrode was demonstrated by Li et al., [54]. Wire shaped DSSCs with PCE value of 8.45% having mechanical strength (102–103 MPa) was demonstrated by Yang et al., they are not only highly flexible abut also showed electrical conductivity ( $10^2\text{--}10^3 \text{ S cm}^{-1}$ ), this could be possible because of the use of CE with graphene fiber electrodeposited with Pt NPs [269]. It was also observed that on increasing the functionalization charge transfer resistance ( $R_{ct}$ ) is decreasing, to overcome this problem a hierarchical vertically oriented graphene was used, which is prepared by a plasma enhanced CVD process on top of a stainless steel substrate; using this CE the lowest  $R_{ct}$  of about  $0.0073 \Omega \text{ cm}^2$  for the  $\text{I}_3^-/\text{I}^-$  redox couple was reported, which is 1% of the level ( $0.59 \Omega \text{ cm}^2$ ) obtained with Pt CE [271]. With superior mechanical flexibility and better optical transparency graphene and its derivatives attracted much research interest in comparison with conventional carbonaceous materials, FTOs spin coated with 1-pyrenebutyrate functionalized rGO were used as CEs a lower PCE of 2.2% was reported for these devices by Xu et al [272], Hong et al. reported PCE of 4.5% using PEDOT:PSS-rGO composite [273]. To further increase the catalytic activity and decrease  $R_{ct}$ , similar methods used for preparing electrodes for super

capacitors and batteries were used [274]. FTOs screen-printed with rGO are used as CEs by Zhang et al., these films formed 3D network structure upon annealing, the increase in specific surface area of these annealed films showed PCE value of 6.81% which is close to that of a reference device with a Pt-CE (7.59%), due to larger available reaction area at the interface between the electrode and electrolyte [128]. To get similar effect from the 3D structure CEs grown with CVD technique fabricated by Lee et al., they reported PEC value of 5.2% [54].  $\text{Li}_2\text{O}$  and CO subjected to react to form three-dimension (3D) honeycomb-like structured graphene CEs, using these CEs PCE of 7.8% was reported by Wang et al. [275], in similar reaction, between  $\text{CO}_2$  gas and Li liquid to form 3D cauliflower fungus-like graphene (CFG), was used by Wei et al., DSSCs with these CEs exhibited high PCE of 8.1% [276]. In order to decrease charge transfer resistance ( $R_{ct}$ ) of graphene-based CEs, other conductive materials like Ag NPs [277], Ni NPs [278][279], Pt NPs [18], and CNTs [280][281] has been combined with graphene to form hybrid CEs. Using rGO–CNT hybrid CEs, DSSCs with PCE of 8.23% was demonstrated by Yang et al. [270], As expected, DSSC fabricated with graphene-with 20% Pt Nano particles hybrid films reported high PCE of 8.79% [18], Highest efficiency of DSSCs without Pt was reported by Bi et al., using hybrid quasi core–shell structure of cobalt sulfide (CoS)–N-doped graphene (NG) films as CE, the PCE value of 10.7% was achieved due to interfacial influence between the core (CoS) and Shell (NG) which enhanced the catalytic activity and conductivity [282].

### 2.6 Graphenaceous Materials as Electron Transport Layers in OPV Devices

The discovery of the  $\text{C}_{60}$  Buckminsterfullerene in 1985 [283] sparked a revolution in the field of carbon materials. In the 30 years that followed, the allotropes of carbon expanded from just graphite and diamond, to a wide range of nanomaterials in various shapes and sizes. A nanomaterial is defined as a material that contains particles with at least one dimension in the nanoscale range, considered to be between 1-100 nm ( $10^{-9}$  m). This is significantly smaller than the micro scale and leads to interesting quantum effects. These quantum effects arise due to a phenomenon known as ‘size quantization’ which occurs in the nanometer range. This phenomenon, often explained using the particle in a box model, is caused by the confinement of movement of electrons and leads to the formation of discrete energy levels or orbitals [284]. These energy levels were the basis of the Bohr atom model in 1913 [285]. However, the Bohr atom model failed to take into account the Heisenberg uncertainty principle, which states that it is not possible to measure the exact position and momentum of an electron simultaneously. To take into account the uncertainty principle, orbitals were redefined as regions in 3D space

where the probability of finding the electron is above a certain value (95%). These atomic orbitals are characterized by a set of quantum numbers  $n$ ,  $l$ , and  $m$  which define the energy of the electron, and the shape and orientation of the orbital. The shape of orbitals, as defined by the quantum number  $l$ , is important to understanding many of the properties of carbon nano materials. The shapes of the  $s$  and the 3 degenerative  $p$  orbitals, which are important when dealing with carbon materials. It is the overlapping of these orbitals which leads to the creation of covalent chemical bonds. The electronic configuration of the six electrons in a standard carbon atom, is  $1s^2$ ,  $2s^2$  and  $2p^2$ . Standard covalent bonds are formed when two atomic orbitals containing one electron each overlap, allowing a sharing of the electron between the two nuclei. In its ground state, carbon has two atomic orbitals which contain one electron each which could be used for bonding. However, because the energy difference between the  $2s$  orbital and the  $2p$  orbitals is so small, it is energetically favorable for one of the electrons in the  $2s$  orbital to jump into the unoccupied  $2p$  orbital, allowing for the creation of 4 equal bonds through a process called ‘orbital hybridization’. This is the process where the  $2s$  and the  $2p$  orbitals hybridize to form  $sp$ ,  $sp^2$  and  $sp^3$  orbitals, depending on how many  $p$  orbitals combine with the  $s$  orbital. This allows the carbon atoms to bond to multiple other elements to form a variety of compounds, as the bond hybridization allows for carbon atoms to bond to 2, 3 or 4 neighboring atoms equally. The  $sp^2$  and  $sp^3$  orbitals are very significant when looking at carbon nanomaterials, as they can be used to explain the two original carbon allotropes, diamond and graphite. Diamond is made completely of  $sp^3$  carbon atoms, with each carbon atom bonded to 4 neighboring carbon atoms in a tetrahedral formation. Alternatively, graphite is made up of multiple flat sheets of  $sp^2$  carbon atoms stacked on top of each other. In graphite sheets, each carbon atom is bonded with three neighboring carbon atoms in a trigonal planar formation, forming a two dimensional hexagonal lattice. The difference in bonding type between diamond and graphite has major implications on the properties of both, particularly the electrical properties. Diamond as a material is electrically insulating, while graphite is electrically conductive, albeit only in two dimensions. This electrical conductivity in graphite is a result of the free electron in the  $p_z$  orbital which sits above and below the plane of  $sp^2$  bonding. The combination and delocalization of these  $p_z$  orbitals on each carbon atom allows for electrical conduction along the graphite sheet. In order to have covalent chemical bonding, electrons must be shared between atoms. This is achieved by combining orbitals (Fig. 2.10), either via end to end overlap, also known as sigma bonding, or side to side overlap, known as  $\pi$  bonding. In diamond, two  $sp^3$  orbitals overlap to form a sigma bonding ( $\sigma$ ) and a sigma anti-bonding ( $\sigma^*$ ) orbital between each carbon atom. The electrons occupy the bonding orbital which is a

lower energy confirmation, thus creating a C - C  $\sigma$  bond. With  $sp^2$  carbon materials such as graphite,  $sp^2$  orbitals overlap to form a C - C  $\sigma$  bond much like in diamond; however the  $p_z$  orbitals can also form delocalized  $\pi$  bonds with neighboring carbon atoms. In the case of benzene which has six  $sp^2$  carbon atoms bonded together in a ring, this creates three pi ( $\pi$ ) bonding orbitals and three pi\* anti-bonding ( $\pi^*$ ) orbitals. When this is extended to graphite, which contains a much larger number of carbon atoms, the  $\pi$  bonding orbitals are easier to consider as a band of orbitals. The energy difference between the highest occupied molecular orbital (HOMO) and the lowest unoccupied molecular orbital (LUMO) is negligible, and therefore electrons can easily be raised from the HOMO level to the LUMO level to facilitate charge transport. Therefore, graphite can be considered a semi-metal which leads to the conductivity in graphite as previously discussed [286].

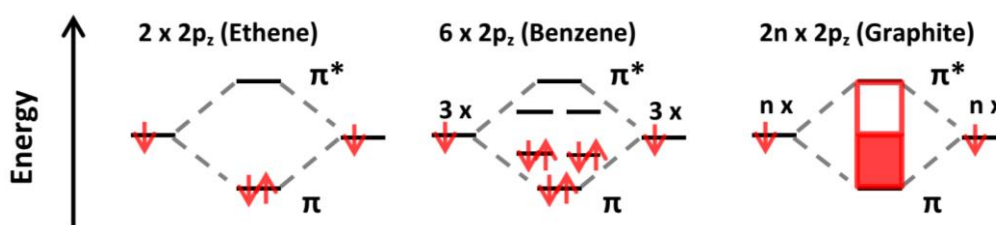


**Figure 2.10:  $\pi$  molecular orbital diagrams for ethene, benzene and graphite, showing the increasing number of  $\pi$  orbitals formed, resulting in the formation of a band of orbitals when  $n$  approaches infinity. The red part of the band represents orbitals filled with electrons. The  $sp^2$  C - C  $\sigma$  bonds are neglected for simplicity.**

The energy of the HOMO and LUMO levels and the difference between them, also known as the band gap, are used to determine the electrical conduction properties of a material. If the gap between the HOMO and the LUMO level is very large, a lot of energy is required to promote an electron into the LUMO level, therefore restricting the movement of the electron, which in turn makes the material an insulator. If the band gap is small, electrons can easily be excited from the HOMO to the LUMO level, via addition of light or heat for example. These materials are classified as semi conducting materials. If the band gap is negligible, like in the case of graphite, then the material is considered a metal or semimetal. The Fermi level ( $E_F$ ) is defined as the electrochemical potential for electrons in the material. In the context of band theory, this relates to a hypothetical energy level between the HOMO and LUMO levels, where the probability of the energy level being filled is 50% [287]. The work function ( $\phi_{WF}$ ) of a material can then be defined as the energy difference between the Fermi level and the vacuum energy level ( $n = \infty$ ) of the material. The band diagrams for various materials are shown in Fig. 2.11.

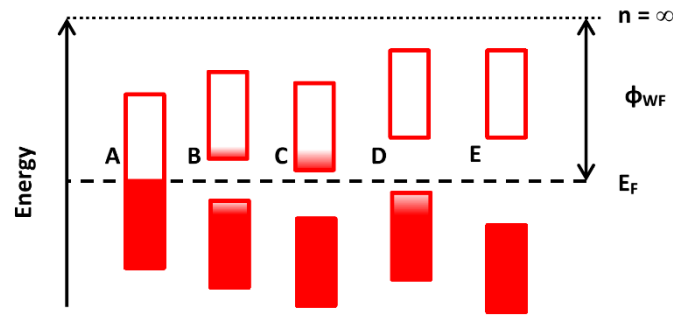


**Figure 2.11: Band energy diagram for (A) a metal, (B) an intrinsic semiconductor, (C) an N-type semiconductor, (D) a P-type semiconductor and (E) and insulator. The Fermi level, vacuum level and work function are also described graphically.**

The semi-metal like conductivity observed in graphite also transfers to other graphite based nanomaterials such as fullerenes, CNTs, and graphene, which are made up of  $sp^2$  bonded carbon atoms much like graphite. As previously stated, graphite is made up of flat sheets of  $sp^2$  carbon atoms stacked on top of each other. These individual layers are given the name graphene, and are only one carbon atom thick. CNTs can be subsequently considered as one graphene sheet rolled into a tube shape, whereas a fullerene, of which the  $C_{60}$  Buckminsterfullerene was the first to be discovered, can be considered as a graphene sheet rolled into the shape of a ball. Therefore, the properties that relate to graphene have wide reaching implications in all carbon nanomaterials, whether looking at graphite, fullerenes, or CNTs. An individual sheet of graphite, the material also known as graphene, was first isolated in 2004 at the University of Manchester by physicists Geim and Novoselov. This and following experiments with graphene led to the pair receiving the Nobel Prize in Physics in 2010. The electrical properties of the individual graphene sheet isolated were remarkable, with electron and hole concentrations of approximately  $10^{13} \text{ cm}^{-2}$  [288]. When an electron is promoted into an excited state, it leaves a vacancy in the orbital it previously occupied. This is referred to as an electron hole. Due to graphene's atomic thickness, it absorbs only 2.3% light per layer making it virtually transparent [289]. This coupled with its electrical properties make it a very interesting material for next generation electronics. Through nano-indentation on a defect-less flake of graphene, it has also demonstrated incredible intrinsic strength and elasticity [290]. These properties make graphene an ideal candidate for use in flexible electronics. However, the major problem limiting the use of graphene in applications is the production method. The original isolation of graphene films in 2004 was accomplished through the repeated delamination of highly ordered pyrolytic graphite (HOPG) using scotch tape. This mechanical exfoliation method, while easy to implement, is not time effective or scalable to the large quantities required for mass production of applications. Other mechanical methods have been

proposed in the literature [291]. However, control of the flake thickness is not easy, and such techniques often require high temperatures to remove chemical adhesives used in the process making them unsuitable for plastic substrates which would be required for flexible applications. Another common method of graphene film synthesis is epitaxial growth via chemical vapour deposition (CVD). Growing graphene via CVD involves depositing carbon based gases such as methane onto a catalytic transition metal surface, e.g. copper, cobalt or nickel. A combination of hydrogen gas and carbon feeder gas flow into a vacuum chamber in the presence of the catalyst and react to deposit carbon atoms on the catalyst surface. This method has been shown to be very effective at producing high quality graphene [165]. Most methods require very high temperatures ( $>700$  °C), although lower temperature alternatives are being developed. Using a photo-thermal CVD process it is possible to produce graphene films with a reported sheet resistance of  $790 \Omega/\square$ . with an optical transmission of over 90% [184]. However, in all epitaxial growth methods, the grown films require delamination from the metal catalyst and a transferring step before it can be used on the target substrate. One of the major routes for graphene material synthesis is the chemical exfoliation of graphite. This requires overcoming graphite's interlayer bonding energy, allowing for separation of individual sheets. Through experimental investigation, the interlayer bonding energy ( $E_b$ ) for graphite has been determined as 42.6 meV per atom at an interlayer distance of 3.35 Å [292]. This bonding energy is the result of a series of electrostatic and dipole interactions designated Van Der Waals forces. The delocalised  $\pi$  bonds caused by the  $p_z$  orbitals can create temporary dipoles above and below individual graphene sheets, which will induce dipoles on neighbouring sheets, and so on throughout the rest of the graphite layers. Chemical exfoliation focuses on disrupting the Van Der Waals interactions, allowing for separation of individual layers. Chemical exfoliation of graphite can be sub-divided into 3 main categories. The first, labelled as direct solvent exfoliation involves finding a suitable solvent that can intercalate in between the layers, disrupting the induction of dipoles and therefore lowering the interlayer binding energy. Various solvents have been suggested in the literature to achieve this, including 1-propanol [293], *N*-methyl-2-pyrrolidinone [294], (NMP) and *N,N*-dimethylformamide (DMF) [295]. One of the major disadvantages of direct solvent exfoliation is the sonication time required in order to achieve a mono disperse solution at high concentrations. Frequently samples contain only small amounts of monolayer graphene, with the majority of the sample containing few layer graphite particles. These few layer graphite materials are nearly impossible to separate from the monolayer graphene flakes owing to their similar size, weight and structure. Another disadvantage with this method is the solvents used are often very harmful and/or toxic to the

environment. For example, one of the best solvents for creating stable graphene solutions from graphite is chlorosulphonic acid, capable of creating 2 mg/mL solutions without the need for sonication [296]. However chlorosulphonic acid is highly toxic, and a powerful lachrymatory agent, commonly referred to as a tear gas, and therefore is not suitable for industrial applications. Another common method for exfoliating graphene from graphite is to use surface active agents or surfactants. Most surfactants are amphiphilic compounds with both a hydrophilic (water attracting) and a hydrophobic (water repelling) end which bridges the gap between the hydrophobic graphene and the water solvent. This method has the advantage of using much more environmentally friendly solvents, such as water in order to achieve a stable dispersion [297]. One of the most notable methods developed recently was the use of a combination of surfactants and shear mixing to demonstrate graphite exfoliation [298]. This method exhibited scale up potential as large quantities of graphene like material could be processed simultaneously. It should be noted that the exfoliation by surfactant is not 100% successful, often producing few layer graphite materials dispersed in the solution. For example, in the case of surfactant combined with shear mixing, the measured thickness of the final flakes was less than 10 layers thick, however only approximately 10% of the flakes were monolayer [298]. The use of surfactant exfoliation is promising because of the high quality graphene materials which can be created. However, the presence of additional surfactant chemicals surrounding the graphene flakes is likely to disrupt the desired electronic properties, unless it is possible to remove the surfactant post deposition. Unfortunately, if the surfactant is removed after exfoliation but before deposition, the van der Waals interactions will cause multilayer flakes to reform. The final type of chemical exfoliation is the functionalization of the graphite material itself, to aid in exfoliation and promote dispersion into environmentally friendly solvents. This overcomes the issue of flake reformation seen in surfactant exfoliation, often at the expense of the quality of the material. The most commonly used method is to oxidize graphite into graphite oxide, which can easily be exfoliated into individual GO sheets and then reduced back to a graphene like material, termed reduced graphene oxide (rGO), after deposition [299] A schematic for this method is shown in Fig. 2.12.

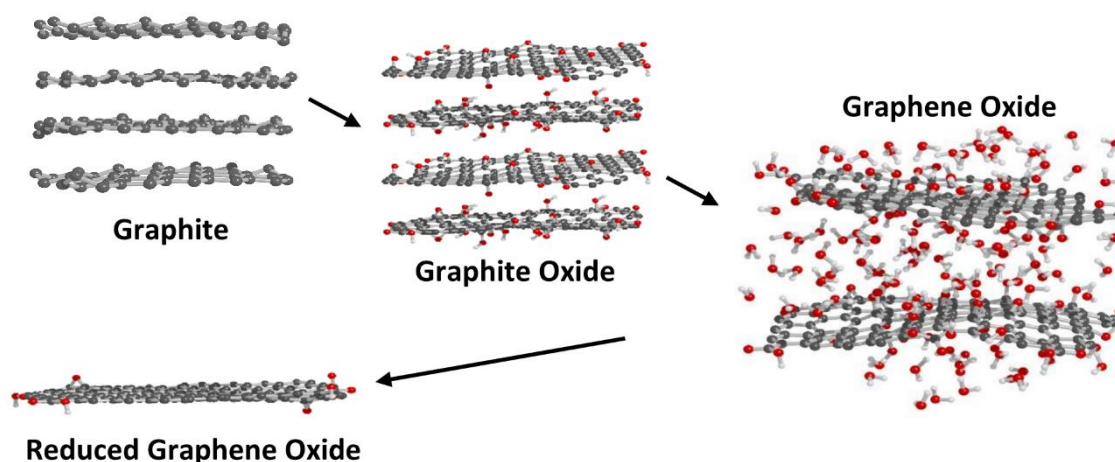


**Figure 2.12: Schematic representation of the chemical exfoliation of Graphite through the production of Graphene oxide. The black, red and white atoms represent carbon, oxygen and hydrogen, respectively.**

As described in the previous section 2.4.2 from Fig. 2.9(right) (page 40) the main requirement of the electron transport layer is to have a work function ( $\phi_{WF}$ ) matches with the LUMO level of the acceptor material, PC70BM approximately  $-4.3$  eV. To achieve this work function Liu et al., doped GO with high electron dense molecule  $Cs_2CO_3$ , by doing this they achieved decrease in work function of GO upto  $-4.0$  eV [270], using the doped GO as ETL, OPV device with PCE of 3.67% (normal architecture) and 2.97% (inverted architecture) was demonstrated with GO as the hole transport layer with high work function at one end and lowered work function n-doped GO as ETL [210]. Since, completely reduced GO (rGO) also have a work function suitable to the PCBM, Qu et al., demonstrated OPV device with PCE value of 3.89 % with rGO noncovalent functionalization via Pyrene to PCBM as ETL for P3HT:PCBM photo active material [300]. Instead of  $Cs_2CO_3$ , air stable oxides with work function approximately equal to LUMO level of PCBM like, ZnO,  $TiO_2$  or  $TiO_x$  are used in [270] composited form with rGO were also used as ETLs [270][212][275]. PCE value of 6.72% (with ZnO-rGO ETL) and 6.57% ( $TiO_2$ -rGO ETL) for OPVs with PCDTBT:PC71BM active layer is reported by Beliatz et al., [212], with the same ETL layers OPVs with PCE values between 7.4 to 7.5% are reported with PTB7:PCBM active layers [301].

---

## Chapter 3 Experimental Procedure

### 3.1 Synthesis of Graphenaceous Materials

This thesis explored the use of solution processable novel graphenaceous materials [302][303][304][305][306][307] as functional materials in DSSC and OPV applications. Brief synthesis methods developed during the course of this theses are presented below:

*Solar reduced graphene oxide (SRGO):* Initially, graphene oxide (GO) sheets were synthesized from a previously reported method [308] which is explained briefly here. 1 g of Graphite flakes (300 mesh, Graftech) was added to 50 g of sodium chloride (NaCl) and ground together for 10 min using a pestle and mortar to produce a uniform mixture. Sufficient water was added to the mixture of graphite flakes and NaCl to dissolve the NaCl with stirring. The NaCl was removed by filtration along with any hetro atomic contamination (~15% of carbon got wasted in this step). The remaining graphite flakes (~0.85 g) were stirred along with 23 ml of Sulphuric Acid (H<sub>2</sub>SO<sub>4</sub>, 98%) for 8 h using a magnetic stirrer. 3 g of Potassium permanganate (KMnO<sub>4</sub>) was then gradually added to the solution while maintaining the solution temperature at <20 °C (While beaker kept in an Ice bath). The mixture was then stirred at 35-40 °C for 30 min, and then at 65-80 °C for 45 min. 46 ml of Distilled water was then added and the mixture heated at 98-105 °C for 30 min. The reaction was terminated by the addition of 140 ml excess Distilled water and 10 ml of hydrogen peroxide solution (H<sub>2</sub>O<sub>2</sub>, 30%) while stirring continuously. The mixture was washed by repeated centrifugation and filtration until it attained a pH of ~7, first with aqueous hydrochloric acid solution (HCl, 5%), to remove any metallic contaminants formed during the synthesis processes, and then with distilled water. Finally, 160 ml of water was added to the final Graphene Oxide (GO) product and mixed well to make a uniform suspension for storage. The GO was subjected to solar-induced chemical reduction (deoxygenation) using a thin solution layer within a petri dish subjected to focused sunlight using a converging lens for around 3 min. The GO is exfoliated during the reduction and results in solar reduced graphene oxide (SRGO).

*Thermal reduced graphene oxide (TRGO):* The GO (above procedure) is placed on a crucible then introduced in a furnace heat treated up to 400 °C (preferably pre heated) up to 2h.

*Thermal reduced few layered graphene (TFLG):* 3 g of graphite flakes (~325 mesh, particle size 44 µm, Alfa Aesar make) are added to a mixture of 9:1 Con. H<sub>2</sub>SO<sub>4</sub>/H<sub>3</sub>PO<sub>4</sub> (360:40 ml). This reaction is an exothermic reaction and therefore results in rise of temperature (35–40 °C).

## Experimental Procedure

---

After 30 min of stirring, 18g of  $\text{KMnO}_4$  was added to the above mixture and was maintained (with stirring) at a temperature of  $50\text{ }^\circ\text{C}$  for 12 h. The reaction mixture was then cooled to room temperature and subsequently kept on an ice bath at  $0\text{ }^\circ\text{C}$ . Then 400 ml of distilled water was poured into the mixture along with 3ml of  $\text{H}_2\text{O}_2$ . The resultant pink solution, which was acidic in nature, was then subjected to multiple washes with distilled water until it attained a pH of  $\sim 7$ . Finally the filtrate was collected and kept in a hot oven at  $100\text{ }^\circ\text{C}$  overnight to obtain GO powder. The dried GO powder was placed on a borosilicate glass and introduced into a furnace pre-heated to  $400\text{ }^\circ\text{C}$  in ambient atmosphere for few minutes. This resulted in exfoliation of GO to FLG.

*Multilayered graphene (MLG):* 3g of graphite flakes (flake size  $\leq 300\text{ }\mu\text{m}$ , Loba Chemie) are added to 60 ml of  $\text{H}_2\text{SO}_4$  (98 %, Fisher Scientific) and stirred overnight. To this mixture, 1.5 g of  $\text{NaNO}_3$  (98 %, SD Fine Chemicals Limited, India) was added and stirred for 5 min. Sixty milliliters of concentrated  $\text{H}_2\text{SO}_4$  was then added to the reaction mixture under stirring. All the above-mentioned additions are done under room conditions. In the subsequent step, reaction mixture was cooled to  $0\text{ }^\circ\text{C}$  using an ice bath and was maintained at  $0\text{ }^\circ\text{C}$  while 9 g of  $\text{KMnO}_4$  was slowly added to the reaction mixture. Zero degrees Celsius was maintained because  $\text{KMnO}_4$  addition leads to a highly exothermic reaction. The reaction mixture was allowed to attain room temperature and was then stirred for 30 min. One hundred fifty milliliters of distilled water was then slowly added to the mixture. Temperature of the mixture was then raised to  $98\text{ }^\circ\text{C}$  and was maintained at this temperature for 1 h. After cooling the mixture to room temperature, it was further diluted by adding 150 ml of distilled water and 5 ml of 30 %  $\text{H}_2\text{O}_2$  (SD Fine Chemicals Limited, India). The mixture was then subjected to multiple washes with distilled water (supernatant was discarded after each wash), and finally, the filtrate was collected and kept overnight (in a hot oven) at  $100\text{ }^\circ\text{C}$  to obtain fine GO powder. GO powder was subsequently irradiated with microwaves in a household microwave oven (IFB Industries Ltd, 30SC2, India) for 3 min (60 s in three cycles) to obtain multilayered graphene (MLG) structures.

*Zinc oxide decorated reduced graphene oxide (ZnO-RGO):* The synthesis of ZnO decorated RGO composites using the MLM technique involves mainly four steps. In the first step, 0.2 g of TFLG powder was dispersed in 250 ml of ethanol by sonication for 30 min to obtain a stable suspension by attaching/removal of the functional groups turning FLG surfaces to rGO. In the second step, 0.9 g of zinc acetate dehydrate ( $\text{Zn}(\text{CH}_3\text{COO})_2 \cdot 2\text{H}_2\text{O}$ ) was added to the r-GO suspension, and the mixture was then ultrasonicated for 2 h. Sonication assists the dispersion

## Experimental Procedure

---

of Zn ions among the suspended r-GO sheets and promotes the reaction between Zn ions and functional groups on the r-GO sheets. In the third step, the solution was vaporized while stirring it at 100 °C in air. During this process, solvent and ligands are expected to be removed, while the Zn ions on r-GO surfaces are expected to form ZnO. The fourth and final step involves heating (calcination process to obtain stable crystalline powders) the product at 500 °C for 8 h in ambient atmosphere to obtain ZnO decorated r-GO named as ZnO-0.2G.

*Silver decorate reduced graphene oxide (Ag-RGO):* 100 mg of MLG was dispersed in 50 mL ethanol and sonicated for 15 min, then added to 1.7 g of AgNO<sub>3</sub> was dissolved in 100 mL distilled water. The reaction mixture was stirred for 30 min at room temperature before addition of the reducing agent. 10 mL of 0.01 mol dm<sup>-3</sup> freshly prepared solution of NaBH<sub>4</sub> was added slowly to the reaction mixture of AgNO<sub>3</sub>-MLG suspension under vigorous stirring. The color of the reaction mixture turns into dark brown to grey depending on the concentration of the AgNO<sub>3</sub>. The reaction mixture was stirred for another 5 h for the complete reduction at room temperature.

### 3.2 Deposition of Active Layers

*Fabrication techniques for the deposition of functional materials can be divided depending on their capability to be used on an industrial scale. Thus, the most common and well-known spin-coating technique does not allow for a high throughput fabrication, and it is therefore accepted as a non-scalable, laboratory-scale deposition method [309]. Coating (except for spin coating), printing, and vacuum-deposition techniques, however, are easily transferable from the laboratory into industry, and they have been successfully implemented for the fabrication of large-area OPV cells.*

#### 3.2.1 Spray coating

Spray coating is an easy technique to deposit materials prepared by solution processing in the form of dispersions and inks, which can be easily deposited on substrates with small area to larger areas. This technique does not require any tedious protocols in the transfer of material from solution to the substrate like other bottom-up approaches. This technique is widely used for large-area processing of thin film. The substrate is kept firmly stable, a spray gun with sufficient concentration of ink (a dispersion of a material) is moved with uniform speed from one end to the other end, keeping the flow rate of the solution/ink constant, this process is repeated to and fro until the solution covers uniformly throughout the substrate. Due to the force of collision of dispersed material in the solution onto the substrate and evaporation of the

## Experimental Procedure

---

solvent the final thickness and adhesion of the film is achieved.

### 3.2.2 Spin coating

Spin-coating is a rotation-based technique for the application of homogeneous and uniform films from an ink (a dispersion of a material) onto a substrate. This technique is widely used for small-area processing of thin films. The working principle can be explained as follows: a sufficient volume of the ink is applied with a pipette onto a substrate so that it covers the complete surface; the ink is then spun off the edges of the substrate, due to a radial flow caused by rotational centrifugal forces. The final thickness of the film is achieved after evaporation of the solvent [66][310]. The desired film thickness  $d$  is empirically proportional to  $c/(\omega^*)^{1/2}$  where  $c$  is the concentration of the solution, and  $\omega^*$  the angular velocity [66]. Further details can be found in the literature [311].

### 3.2.3 Vacuum-thermal evaporation technique

Thermal evaporation under high vacuum can be used for the deposition of various materials such as small molecules, metals, and semiconductors. The evaporation process is usually carried out in a vacuum chamber at pressures of less than  $3 \times 10^{-6}$  mbar. This allows for atoms and molecules to travel directly to the surface of a substrate, where they condense to form a film. The material to be vaporized is placed in a tungsten filament or a crucible and heated electrically by way of the Joule effect. The evaporation rate and film thickness can be monitored with a quartz oscillator with a resolution limit of about 0.1 Å/s. For this thesis, the vacuum thermal evaporation of Al was undertaken in a Moorfield Nanotechnology Ltd. evaporator.

## 3.3 Fabrication of DSSC Device

### 3.3.1 Preparation of nanocrystalline $\text{TiO}_2$ photo-anode

Photo-electrodes were fabricated by following a previously reported procedure (Susmitha et al., 2015) which is briefly given here for convenience. As-procured fluorine-doped tin oxide (FTO) conducting glass plates (7 Ω/square, TCO22-7, Solaronix) were cleaned with a detergent solution and then rinsed sequentially with Millipore water, absolute ethanol and 2-propanol (Merck, Germany) to remove organic and other particulate contaminants. FTO glass plates were then dried under a nitrogen purge. Nanocrystalline titanium dioxide ( $\text{TiO}_2$ , anatase phase) layer was coated onto the FTO glass plates and then sintered. In order to make sure that the  $\text{TiO}_2$  layer has a good mechanical contact with the conducting FTO glass substrate,  $\text{TiO}_2$

## Experimental Procedure

---

coated plates were treated with a 40 mM titanium tetrachloride ( $\text{TiCl}_4$ ) solution at 70 °C. A 43T mesh screen was used to produce 12  $\mu\text{m}$  thick  $\text{TiO}_2$  film using commercial 18 nm  $\text{TiO}_2$  colloidal paste (18NR-T, Dyesol) after sintering at 500 °C for 30 min. Another 90T mesh screen was used to produce 6  $\mu\text{m}$  thick film of 200 nm scatter  $\text{TiO}_2$  paste (WER2-O, Dyesol). A post-deposition  $\text{TiCl}_4$  treatment was then undertaken, before sintering further at 500 °C for 30 min. While cooling the electrodes to around 110 °C, the electrodes were stained in purified cis-bis(isothiocyanato) bis (2,2'-bipyridyl-4,4'-dicarboxylato) ruthenium (II)-bis-tetrabutylammonium dye solution (0.3 mM, N719), prepared in a mixture of tert-butanol/acetonitrile (1/1 v/v), for 18 h under dark conditions. The photoelectrode was subsequently withdrawn from the solution and rinsed twice with anhydrous acetonitrile to remove any unanchored dye molecules on the surface of the  $\text{TiO}_2$  film. The plates were finally dried under nitrogen purge. The schematic depicting all the steps is given in Appendix 1.

### 3.3.2 Fabrication of GO and SRGO counter electrodes

GO and SRGO were prepared using previously reported procedures in section 3.1. 1 mg of GO (or SRGO) was then dispersed in 1 mL of iso-propanol (Merck, Germany) and the resultant solution was ultra sonicated for 30 min prior to spray coating the entire volume with a spray gun at 1 mL/min using pure  $\text{N}_2$  gas. To inject the electrolyte into the test cells, holes (0.1 mm diameter) were drilled into the FTO glass plates using a micro-tipped drill (DREMEL 300) with a diamond coated micro-drill bit. The FTO glass was washed sequentially with diluted detergent, 0.1 M HCl solution in ethanol, Millipore water, absolute ethanol and finally cleaned with isopropanol in a sonicator for 30 min. The cleaned FTO glass substrate was placed on a hotplate at 180 °C and the entire 1 ml of GO (or SRGO) solution was spray coated using a 0.3 mm micro-tip needle spray gun at 1 mL  $\text{min}^{-1}$  using pure  $\text{N}_2$  gas. The temperature 180 °C was used during spray coating to ensure the evaporation of the solvent and good adhesion of the GO (or SRGO) to the FTO substrate. The heat treatment to a moderate temperature of 380 °C after the coating is to increase the porosity of GO (or SRGO) for enhancing the adsorption of the electrolyte for improvement in electrochemical activity, which in turn enhances the efficiency of the DSSC. The spray coated GO or SRGO FTO glass substrate was then heated in a furnace at 380 °C for 30 min to obtain FTO/GO and FTO/SRGO CEs. The schematic depicting all the steps is given in Appendix 2.

## Experimental Procedure

### 3.3.3 Fabrication of the device

The photo-anodes and CEs were assembled using thermal adhesive (25 lm, Surlyn, Solaronix) as a spacer to produce a sandwich cell. The liquid electrolyte was prepared by mixing 1-butyl-3-met hyylimidazoliumiodide (BMII, 0.5 M), lithium iodide (LiI, 0.1 M), Iodine (I<sub>2</sub>, 0.05 M), guanidiniethiocyanate (GuNC, 0.1 M), and terbutylpyridine (tBP, 0.5 M) in acetonitrile. The prepared electrolyte was injected through the hole drilled through the CE, before the holes were sealed with a cover glass using Surlyn. The fabricated DSSCs (Table 3.1) have an active area of 0.36 cm<sup>2</sup>.

**Table 3.1: Photo- and counter-electrode configurations.**

Photo-electrode	Counter electrode	Cell name
FTO/TiO <sub>2</sub> /N719	FTO/GO	GO-DSSC
FTO/TiO <sub>2</sub> /N719	FTO/SRGO	SRGO-DSSC

The schematic depicting all the steps is given in Appendix 3.

### 3.4 Fabrication of OPV devices

Poly[N-9'-heptadecanyl-2,7-carbazole-alt-5,5-(4',7'-di-2-thienyl-2',1',3'benzothiadiazole)] (PCDTBT SOL4280, Solaris Chem Inc.) and [6,6]-Phenyl-C71-butyric acid methyl ester (PC70BM, Nano-C) were used for preparing BHJ blend. The PCDTBT:PC70BM (D-A components) were mixed in a 3:1 vol.% solution of 1, 2 dichlorobenzene (o-DCB, 99%) and chlorobenzene (CB, 99.8%). To prepare the BHJ blend, a total 35mg of PCDTBT and PC70BM in 1:4 weight ratio were mixed into o-DCB:CB (3:1 by vol.% in 1 mL) and dissolved for at least 24 hours under vigorous stirring at room temperature. Poly(3,4-ethylenedioxythiophene) poly-(styrenesulfonate) (PEDOT-PSS Clevis P VP AI 4083, Heraeus Holding GmbH) was used as the hole transport layer and as synthesized graphenaceous materials mentioned in the above section 3.1 were used as the electron transport layer. To prepare the ETL solution, initially a stock solution containing 20mg of the as synthesised graphenaceous materials (SRGO/TRGO/TFLG/MLG/Ag-RGO/Zno-RGO) dispersed in 20ml of methanol. This stock solution was further diluted in methanol by 1:200 V/V ratio before deposition.

In this work only standard solar cells having ITO-glass/HTL/BHJ/ETL/Al structure were fabricated. The fabrication procedure was carried out in 7 steps, (1) substrate cleaning, (2) and (3) PEDOT:PSS application as HTL, (4) and (5) BHJ application, (6) ETL and electrode evaporation and (7) complete device ITO-patterned (1.5 cm × 1.5 cm glass substrates with a

## Experimental Procedure

---

centered 1.5 cm × 0.9 cm ITO stripe) were first cleaned (step 1) in soap water, deionised water (DI), acetone and methanol for 5 min respectively using ultrasonic bath. A nitrogen gun was used to blow dry the substrates. Then the substrates were subjected to oxygen (O<sub>2</sub>) plasma for 5 min at 100 W and 15 sccm O<sub>2</sub> in Emitech K1050X plasma asher. 100 µl of the PEDOT:PSS solution was pipetted on the substrate and spin-coated for 60 s at 4000 rpm to form approximately 40 nm thin film (step 2 and 3). Samples were then transferred onto a hot plate in a nitrogen filled glove box and were annealed for 30 min at 150 °C to improve the PEDOT:PSS conductivity by removing the residual DI water[17]. Samples were then put on the chuck of the spin-coater equipment and the as prepared PCDTBT:PC70BM BHJ blend (40 µl) mentioned above was then pipetted on top of the PEDOT:PSS layer for 30 s at 3000 rpm (step 4 and 5). To carry out BHJ solvent annealing and drying the samples were covered with a petri dish (60 mm diameter, 15 mm height) for 30 min. Next, the samples were placed on a hot plate for 10 min to carry out thermal pre-annealing at 150 °C. One of the ETL solutions diluted in methonal as mention above were deposited on top of the BHJ layer by placing the samples again on the spin coater for 45 s at 3000 rpm (step 6). At the end, the samples were put in a metal holder with a shadow mask is placed in a vacuum thermal evaporator installed in the same glove box, where the 80 nm thick Al electrode were deposited (step 7). An aluminum evaporation (80 nm, pressure below 3 × 10<sup>-6</sup> mbar) through a shadow mask. The overlap between the Al and ITO electrodes within the devices was 0.90 cm<sup>2</sup>. All fabrication steps after the PEDOT:PSS deposition were performed in a nitrogen-filled glove box. The schematic depicting all the steps is given in Appendix 4.

### 3.5 Characterization of Materials

Scanning electron microscopy was mainly used to obtained secondary electron (SE) images of synthesized considered in this study. For all synthesized materials, field emission scanning electron microscope (FESEM, model Zeiss Ultra 55) operated at accelerating voltages of 5 kV was used. Care was taken to avoid the charging effects by imaging an area quickly (high scan rate) without compromising on the quality of the image. In this work, x-ray diffraction (XRD) patterns are recorded with 2θ (where θ is the angle of diffraction) values from 10 to 60° using Cu Kα as the X-ray source (λ=1.54 Å); Bruker's AXS Model D8 Advance System was used to carry out the XRD experiments. Standard procedure was followed to index the diffraction peaks apart from comparing the patters with standard patterns available in the internationally accepted databases. XRD study was carried out to understand the crystallinity of different synthesized materials. Raman spectroscopic study was carried out using LabRam HR800

## Experimental Procedure

---

Raman spectrometer; 514.5 nm green line of Ar<sup>+</sup> ion laser was used as the excitation source. The spectral resolution of all the measurements was 1 cm<sup>-1</sup>. All spectra were recorded in the wavenumber range 0-3000 cm<sup>-1</sup>. Specific to CNMs, Raman scattering is helpful for determining the graphitic and defects characteristics of the samples. It is also useful in estimating the number of graphene layers in the graphenaceous materials. The presence of pores in the samples was investigated using physical adsorption of N<sub>2</sub> at the liquid N<sub>2</sub> temperature (77 K) on an automatic surface area and porosity analyzer (ASAP2010, Micromeritics). Prior to the measurements, each sample was vacuum-degassed at 200 °C for 5 h. Using Brunauer-Emmett-Teller (BET) method, specific surface area of the samples was estimated in the relative pressure range 0.01-0.2. The total pore volume was obtained from the volume of N<sub>2</sub> adsorbed at a relative pressure of 0.99. Pore size distribution in each sample was obtained using Barret-Joyner-Halenda (BJH) equation. For deeper understanding of the role of Solar reduced graphene oxide (SRGO) in the functioning of DSSC, morphological studies were also carried out using transmission electron microscope (TEM) (Model: FEI Technai G2 S – Twin). 200 kV of operating accelerating voltage was used. Very minute amount of SRGO was mixed in methanol and after homogeneously mixing, the SRGO-methanol solution was drop casted on to the holey carbon TEM grid for transferring SRGO onto the grid after evaporation of methanol.

### 3.6 Device Characterization and Testing

#### 3.6.1 Electrochemical characterization of DSSC devices

Cyclic-voltammetry was used to understand I<sup>-</sup> - I<sub>3</sub> redox reaction occurring in the LiClO<sub>4</sub> (0.1 M)/LiI (5 mM)/I<sub>2</sub> (0.5 mM)/ acetonitrile electrolyte solution at the CEs. A potentiostat (CHI608E instrument) in a three electrode configuration was used to measure the current at a scan rate of 10 mVs<sup>-1</sup>. An Ag/Ag<sup>+</sup> electrode (0.01 M AgNO<sub>3</sub> in acetonitrile) was used as the reference electrode, and the TiO<sub>2</sub>/dye complex was used as the working electrode.

Electrochemical impedance spectroscopy (EIS) was performed in the frequency range of 0.1 Hz to 100 kHz on an electrochemical workstation (IVIUMSTAT, IVIUM technologies b.v.) at 10 mV and respective open circuit voltage.

#### 3.6.2 I-V characteristics of the solar cells

To check the solar photovoltaic performance of the fabricated DSSCs, the current density-voltage characteristics were measured under the illumination of Xe arc solar simulator (PEC-

## Experimental Procedure

---

L01, Peccell Inc., Japan) with AM 1.5 spectral filter and source-meter (2401 Keithley Instruments Inc, U.S.A.). The intensity was adjusted to provide 1 sun ( $100 \text{ mW cm}^{-2}$ ) using a calibrated Si solar cell. For OPV devices, Keithley 2400 source measurement apparatus was used for acquiring current-voltage (I-V) characterizations in the four-point probe configuration. Test was conducted in ambient atmosphere, without encapsulation. An Abet Technologies 10500 solar simulator (class AAB) at AM 1.5 G, calibrated with a silicon reference cell (PV Measurements, Inc. 20 mm x 20 mm) to  $100 \text{ mW cm}^{-2}$ , was used to illuminate the devices. For more accurate definition of the illuminated area, an aperture of  $0.43 \text{ cm}^2$  was used.

### *3.6.3 External quantum efficiency of OPV devices*

For external quantum efficiency (EQE) measurements, a Bentham Instruments PVE 300, with 1-Sun light bias, was utilized in the wavelength range from 300 nm to 800 nm (5 nm step).

---

## Chapter 4 Results and Discussion

### 4.1 Morphology and Composition of Graphenaceous Materials

Graphene oxide (GO) was synthesized using a modified Hummers method and was reduced by using focused sunlight to obtain solar reduced graphene oxide (SRGO) [302]. GO and SRGO are then used as Pt free counter electrode materials in dye sensitized solar cells (DSSCs). X-ray diffraction (XRD) analysis of graphite flakes (the starting material), the synthesized Counter electrode materials GO and SRGO showed characteristic differences in the diffraction peak positions confirming the formation of GO from graphite flakes and SRGO from GO.

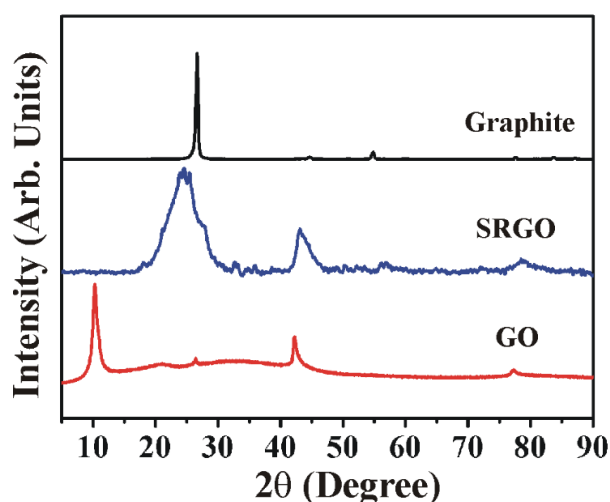


**Figure 4.1: X-ray diffractograms of graphite, SRGO and GO.**

XRD profile (Fig. 4.1) of graphite is dominated by the intense diffraction peak at  $2\theta = 26^\circ$  which corresponds to the characteristic reflection from (002) graphite planes. Low intensity diffraction peak at  $2\theta = 54^\circ$  corresponds to the reflection from (004) graphite planes. XRD profile of GO shows a peak at  $2\theta = 11.2^\circ$  which is characteristic of increase in spacing between the graphite planes along its c-axis due to oxidation of graphite. Other characteristic peak pertaining to the oxidation of graphite or formation of GO is also observed at  $2\theta = 44^\circ$  [312]. XRD profile of SRGO has a broad primary peak at  $2\theta = \sim 24^\circ$  which is characteristic of reduction of GO or formation of SRGO (i.e., formation of few layered graphene along with removal of oxygen functional groups). The appearance of (002) peak again close to  $2\theta = 26^\circ$  (now at  $\sim 24^\circ$ ) in the case of SRGO is indicative of decrease in the spacing between the graphene basal planes in SRGO. X-ray diffractogram of SRGO indicates that the reduction of GO to SRGO is only partial because (002) peak did not appear again at its original position of  $2\theta = 26^\circ$ . There is every possibility that the residual oxygen functional groups present in the

## Results and Discussion

SRGO may electrostatically interact with the liquid electrolyte. Enhanced specific surface area and increased porosity (as indicated by BET analysis shown in Fig. 4.4) may also assist in enhanced interaction of the SRGO with the liquid electrolyte and consequently allow the participation of cations in the intercalation and adsorption onto SRGO while participating in the operation of DSSC. This gives an indication that that SRGO may perform better than GO as a CE in DSSC.

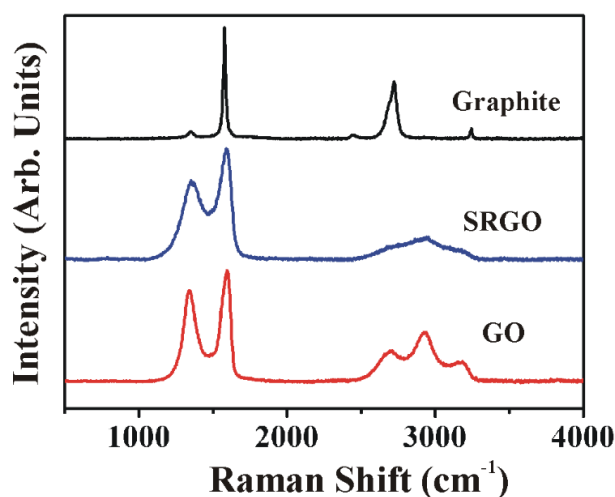


**Figure 4.2: Raman spectra of graphite, SRGO and GO.**

Raman scattering analysis complemented well with the XRD analysis. The Raman spectra (Fig. 4.2) of GO and SRGO in comparison with the Raman spectrum of graphite. Bands at  $\sim 1348$ ,  $\sim 1575$ , and  $\sim 2710$   $\text{cm}^{-1}$  in the case of graphite are the typical D, G and 2D Raman bands, respectively. The broad bands at  $\sim 1334$  and  $1596$   $\text{cm}^{-1}$  in the case of GO are the typical D and G bands, respectively. The typical triplicate of D+G, 2D and 2D' overtone bands indicative of the oxidation of graphite or formation of GO are also discernible in the case of GO. In the case of SRGO Raman spectrum, the D band is slightly red-shifted ( $1350$   $\text{cm}^{-1}$ ) while the G band is slightly blue-shifted ( $1588$   $\text{cm}^{-1}$ ). The intensity ratio,  $I_D/I_G$  in the case of SRGO is 0.718 which is lower in comparison to that of GO ( $I_D/I_G$  in the case of GO is 0.814). This indicates an increase in the size of the in-plane  $\text{sp}^2$  domains through the removal of oxygen functional groups from the GO sheets [302]. Electron microscopy (Fig. 4.3) showed that SRGO consisted of randomly aggregated, thin and wrinkled graphene sheets with a close restacking with one another forming a disordered solid.

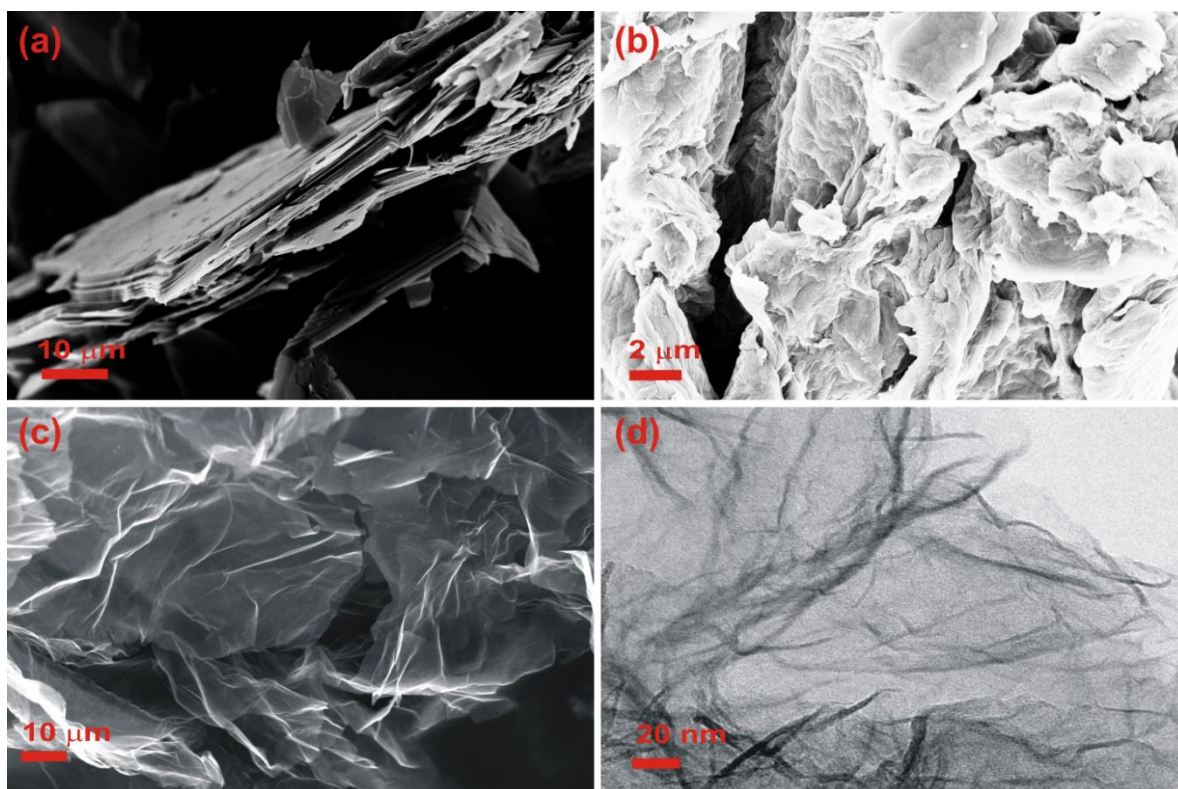


**Figure 4.3: Secondary electron micrographs of (a) Graphite, (b) GO and (c) SRGO and (b) transmission electron micrograph of SRGO.**

N<sub>2</sub> adsorption/desorption isotherms (Fig. 4.4) of GO and SRGO resembled type IV characteristics of Brunauer-Emmett-Teller (BET) classification types I-VI whilst the hysteresis loops in both the cases are found in the relative pressure range of 0.4–0.9. BET specific surface area of SRGO (~107 m<sup>2</sup>/g) was found to be more than double that of GO (~51 m<sup>2</sup>/g) indicates that, SRGO exhibited mesoporosity which can play a major role in enhancing its performance as a CE as it allows the faster mobility of the charge carriers and thereby improving the activity at the electrode/electrolyte interfacial area.

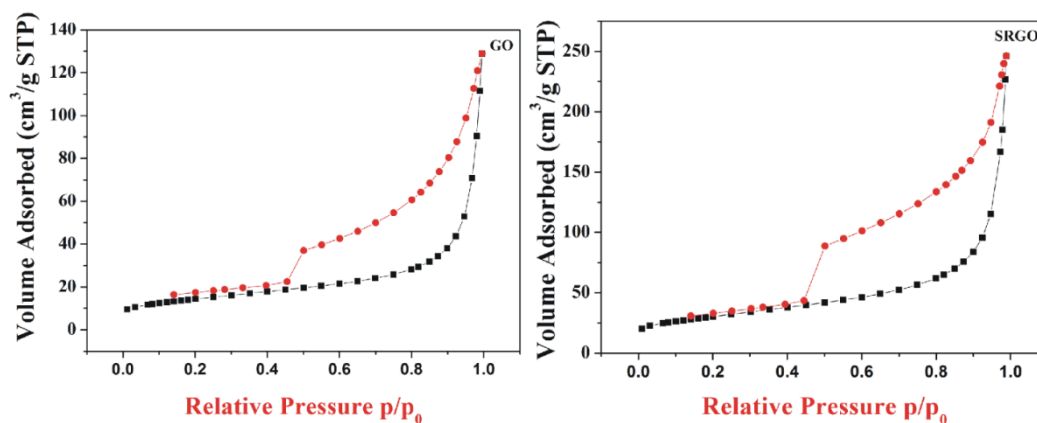


**Figure 4.4: N<sub>2</sub> adsorption/desorption isotherms of GO (left) and SRGO (right).**

### 4.2 Electrochemical Analysis of DSSC Devices

The main functions of a CE in DSSC are to provide the pathway for electron transfer from the external circuit to the redox electrolyte and to catalyze the reduction of  $I_3^-$  to promote the regeneration of dye molecules [313][17][18]. Therefore, the electro-catalytic activity during the reduction of  $I_3^-$  is a key factor for determining the performance of a CE. In this context, CV curves of GO and SRGO are compared in Fig. 4.5.

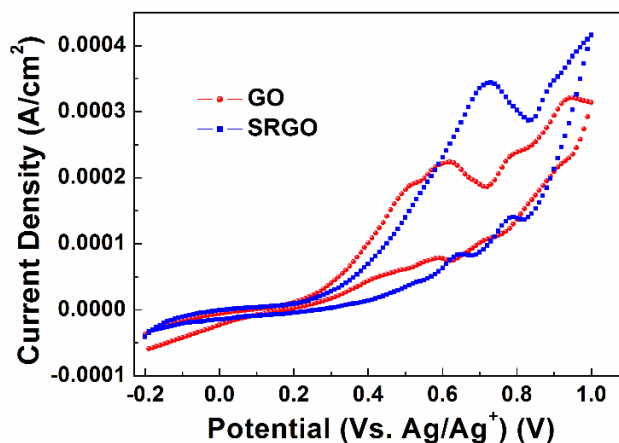


Figure 4.5: CV curves of GO and SRGO electrodes.

Two redox peaks are discernible in the case of SRGO electrode. The peak at  $\sim 0.64$  V is attributed to  $3I_2 + 2e^- \rightarrow 2I_3^-$  reaction whilst the one at  $\sim 0.79$  V is attributed to  $I_3^- + 2e^- \rightarrow 3I^-$  reaction [314]. On the other hand, a lone cathodic peak at  $\sim 0.59$  V is discernible in the case of GO electrode. Peaks corresponding to redox pairs (as observed in the case of SRGO) are indiscernible probably due to the domination of background current [314][315]. CV characteristics of GO and SRGO electrodes as-extracted from the CV curves are compared in Table 4.1. The smaller difference ( $\Delta E_p$ ) between the cathodic and anodic peak potentials in the case of SRGO electrode in comparison to that of GO electrode shows that SRGO is a better electrode to catalyze the reduction of the tri iodide ion to iodide.

Table 4.1: Comparison of CV characteristics of GO and SRGO electrodes.

Sample	Peak Potential (mV)		Reaction	$\Delta E_p$ (mV)
	Cathodic	Anodic		
GO	---	590	---	--
	720	690	$3I_2 + 2e^- \rightarrow 2I_3^-$	30
	890	830	$I_3^- + 2e^- \rightarrow 3I^-$	60
SRGO	520	520	---	0
	620	640	$3I_2 + 2e^- \rightarrow 2I_3^-$	20
	790	780	$I_3^- + 2e^- \rightarrow 3I^-$	10

Nyquist plots pertaining to DSSCs constituted by GO and SRGO CEs are shown in Fig. 4.6 (next page). The circuit (as-obtained by fitting the EIS data using the software IVIUM Soft v. 2.509) corresponding to the spectra is also shown in Fig. 4.6. The sheet resistance element ( $R_s$ ) of the GO and SRGO DSSCs is measured as 49 and 5  $\Omega \text{ cm}^2$  respectively, indicating that the SRGO film is firmly bonded to the FTO substrate and exhibits a lower  $R_s$  and therefore indicating an enhanced electron transfer from SRGO CE to the  $I_3^-$  ion in the electrolyte. The lower internal resistance element ( $R_{ct1}$ ) measured as  $\sim 34 \Omega \text{ cm}^2$  at the SRGOCE/electrolyte interface (compared to  $\sim 175 \Omega \text{ cm}^2$  in the case of GO) indicates that an enhanced electrocatalytic redox reactivity is achieved in the reduction of  $I_3^-$  at the interface. Low  $R_s$  and total internal resistance ( $R_{ct}$ ) are indicative of the ease of transfer of charge to the CE and effective reduction of  $I_3^-$  to  $I^-$  at the electrolyte/CE interface, respectively and both of which favor the regeneration of the dye molecules at the electrolyte/photo-electrode interface [315]. Lower  $R_{ct}$  also means a lower over-potential for electrons transferring from CE to electrolyte, and is therefore also indicative of an easier electron transfer [316][124][317]. It is known that the lower  $R_s$  and  $R_{ct1}$  values subsequently lead to an enhancement in  $J_{SC}$  [318].

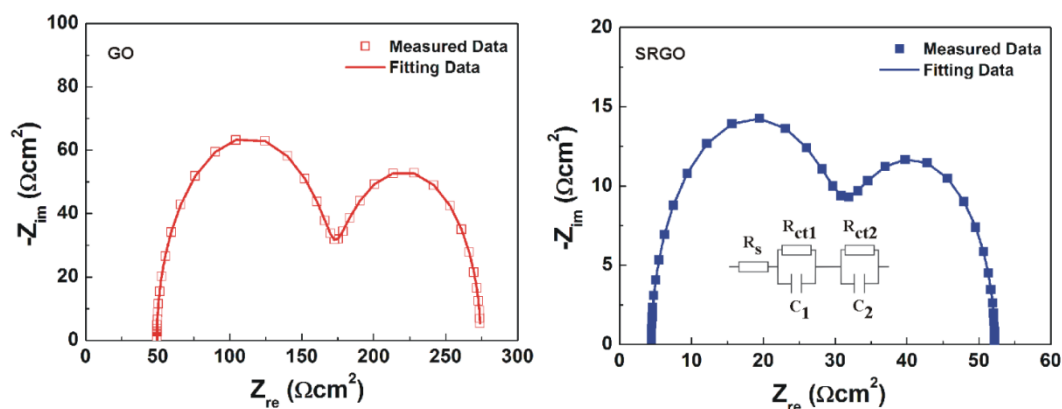


**Figure 4.6: Electrochemical impedance spectra of GO (left) and SRGO (right). Inset shows the equivalent circuit used for fitting the EIS data in both GO and SRGO cases.**

### 4.3 Photovoltaic Performance of DSSC Devices

The photocurrent density ( $J$ ) versus voltage ( $V$ ) curves of the fabricated DSSCs are shown in Fig. 4.7 while the calculated photovoltaic parameters using Equ. 2.5 mentioned in section 2.3.3 of the cells are tabulated in Table 4.2.

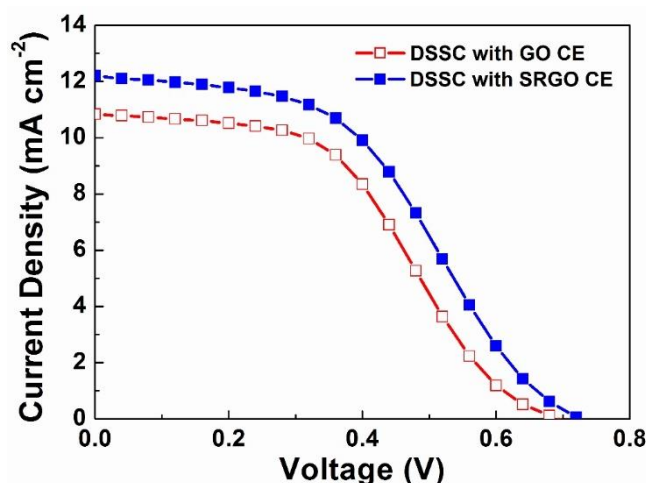


**Figure 4.7: Photocurrent density versus voltage characteristics of DSSCs with GO and SRGO CEs.**

**Table 4.2: Photovoltaic performances of the GO and SRGO DSSC test cells.**

Cell Name	$V_{OC}$ (V)	$J_{SC}$ (mA/cm <sup>2</sup> )	$FF$	$\eta$ (%)	$R_s$ ( $\square$ cm <sup>2</sup> )	$R_{ct}$ ( $\square$ cm <sup>2</sup> )
GO-DSSC	0.69	10.83	0.45	3.38	49.02	632.48
SRGO-DSSC	0.72	12.20	0.44	3.96	5.04	132.50

The S-shaped J-V curve arises due to charge accumulation/trapping at either of the electrode electrolyte interfaces as a result of a mismatch between the work function and the electrolyte redox potentials [126]. This is more likely to occur at the FTO/TiO<sub>2</sub> cathode, due to the unavoidable existence of impurity induced energy gap states in the thin TiO<sub>2</sub> layer and the low mobility of holes during charge transport due to their hopping mechanism. Alternatively, it may be due to defects at the counter electrode interface, and other interfacial behavior in the fabricated solar cells. The DSSC with SRGO CE exhibits  $J_{SC}$  of 12.20 mA/cm<sup>2</sup>,  $V_{OC}$  of 0.72 V and  $FF$  of 0.44. This yields  $\eta$  of 3.96 %, which is higher than that of the DSSC constituted by GO CE ( $\eta$ = 3.38%). The higher  $V_{OC}$  in the case of SRGO is attributed to the positive shift in the iodide/tri-iodide redox energy level [315][317].

### 4.4 Photovoltaic Performance of OPV Devices

The power conversion efficiency ( $\eta$ ) was calculated using Equ. 2.5 mentioned in section 2.3.3, series resistance ( $R_s$ ) of a polymer solar cell can be accurately evaluated as the differential resistance  $dV/dJ$  i.e slope of the photocurrent density versus voltage (J-V) curve near the operating voltage  $V_{oc}$  of the cell and shunt resistance ( $R_{sh}$ ) is determined from the inverse slope of the light J-V curve near the  $J_{sc}$ . Semi-logarithmic plot of the  $J_{dark}$  curve is plotted for better visual interpretation. The polymer solar cell (PSC) characteristics obtained by using synthesized graphene materials as ETLs are tabulated in Table 4.3. The polymer solar cell with conventional device architecture as mentioned above without any electron transport layer was fabricated as a reference solar cell. The characteristics of the same are shown in Fig. 4.8. The solar cells characteristics shows efficiency of 5.03, which is lowest of all the devices as expected due to the non-alignment of the energy band structure. The symmetric shape of dark current curve up to 0.5 V of the reference cell in Fig. 4.8(b) clearly indicates charge carrier recombination and trapping at the electrode interface resulting in lower fill factor (FF) of 53.2 resulting in higher shunt resistance ( $R_{sh}$ ) of  $4390.64 \Omega/cm^2$  as a result sum of bulk resistance of each layer which is represented by series resistance ( $R_s$ ) is  $12.97 \Omega/cm^2$ . Even though the charge recombination is taking place, when light shines on the solar cell, because of the existence of incident photon converted charge carriers in the photoactive layer (PCDTBT:PC<sub>70</sub>BM) as shown in the Fig. 4.9, the solar cell exhibited short-circuit current density ( $J_{sc}$ ) of  $13.31 \text{ mA/cm}^2$  as shown in Fig. 4.8(a) resulting in an open-circuit voltage ( $V_{oc}$ ) of 0.71V.

**Table 4.3: Comparison of the photovoltaic performance of the PSCs fabricated with different ETLs.**

ETL Used	$V_{oc}$ (V)	$J_{sc}$ ( $\text{mA/cm}^2$ )	FF (%)	$\eta$ (%)	$R_s$ ( $\Omega/cm^2$ )	$R_{sh}$ ( $\Omega/cm^2$ )
No ETL	0.71	13.31	53.2	5.03	12.97	4390.64
Ag-RGO	0.88	9.97	59.3	5.21	14.42	1494.75
ZnO-RGO	0.9	10.87	59.9	5.86	16.1	4466.55
SRGO	0.84	11.83	59.7	5.93	11.04	3091.09
MLG	0.89	11.12	65.1	6.45	8.57	1730.75
TRGO	0.89	11.91	63.8	6.77	11.07	614.52
TFLG	0.9	12.08	63.4	6.9	9.98	447.1

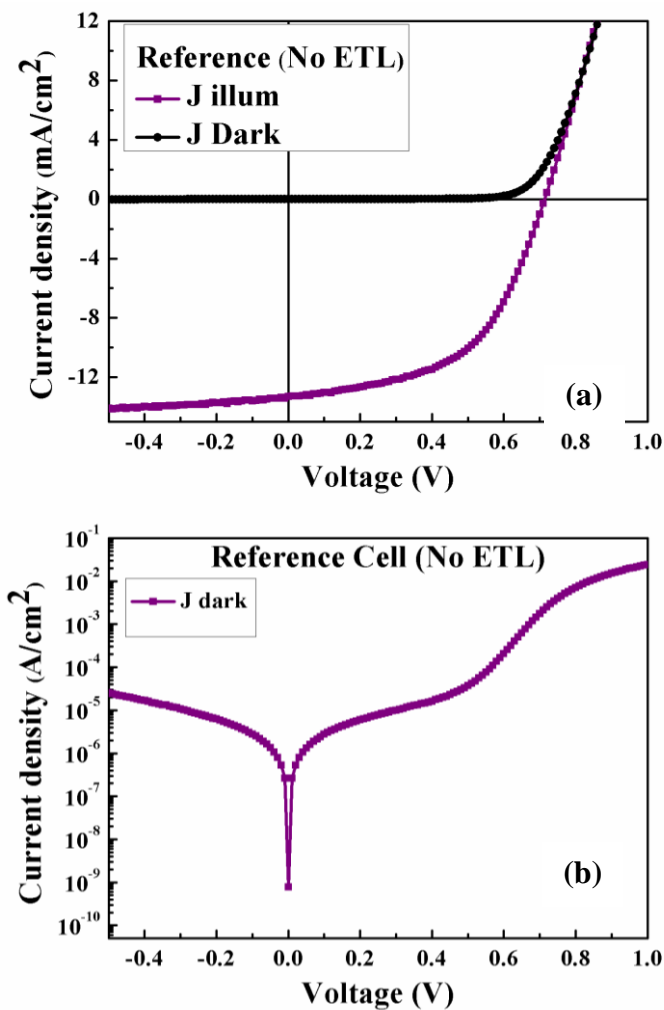


Figure 4.8: Photocurrent density ( $J$ ) versus voltage ( $V$ ) characteristics of reference polymer solar cell (without any electron transport layer) and corresponding semi-logarithmic plot of the  $J_{\text{dark}}$ .

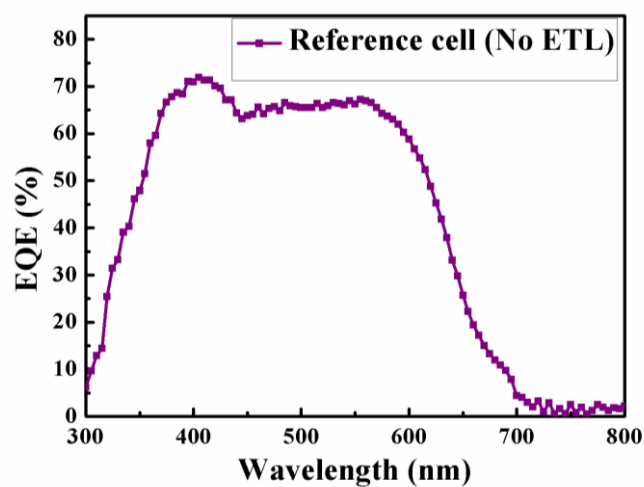
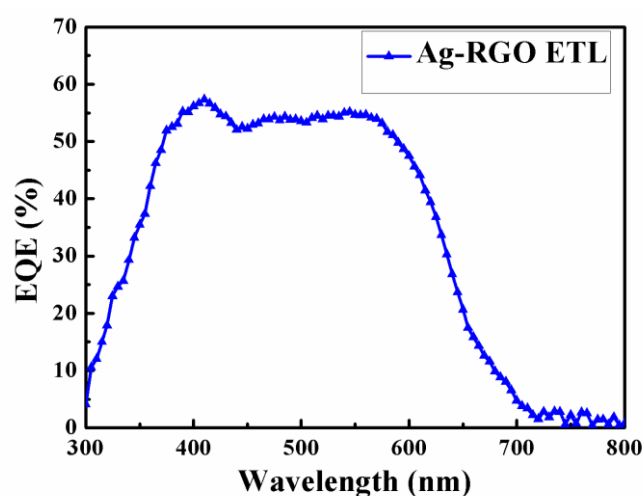


Figure 4.9: External quantum efficiency (EQE) spectrum of the Reference polymer solar cell.

Ag-RGO was introduced as an ETL to improve the efficiency of the PSC, even though the shunt resistance ( $R_{sh}$ ) decreased to  $1494.75 \Omega/cm^2$ , indicating good transport mechanism due to the presence of Ag, the increase in series resistance ( $R_s$ ) to  $14.42 \Omega/cm^2$  indicates that resistance at the interface of the layers increased and decrease in EQE values (Fig. 4.10) upto 50% resulted in lower short-circuit current density ( $J_{sc}$ ) of  $9.97 mA/cm^2$  (Fig. 4.11), this may be due to the plasmonic effects of nanosilver particles, trapping of light and internal reflection or scattering of photons in the solar cell, resulting a very low enhancement in the power conversion efficiency ( $\eta$ ) upto 5.21%.



**Figure 4.10: External quantum efficiency (EQE) spectrum of the polymer solar cell with Ag-RGO ETL.**

When ZnO-RGO composite was used as electron transport layer, even though  $R_s$  ( $16.1 \Omega/cm^2$ ) and  $R_{sh}$  ( $4466.55 \Omega/cm^2$ ) are high, due to band alignment of conduction band ZnO at 4.2 eV with the Al back contact and RGO resulted in 60% EQE (Fig. 4.12) which in turn resulted in a higher  $J_{sc}$  value of  $10.87 mA/cm^2$  (Fig. 4.13) compared to Ag-RGO ETL, resulting in higher  $V_{oc}$  (0.9 V) and PCE of 5.86 %. Since, hybrid/composite materials of reduced graphene oxide has not resulted in more than 16.5% enhancement in PEC, in this work, as synthesised grapheneous materials which are diluted in methanol (1:200 v/v) are used as ETLs, PEC of 5.93% is achieved with SRGO as ETL, with lower  $R_s$  ( $11.04 \Omega/cm^2$ ) and  $R_{sh}$  ( $3091.09 \Omega/cm^2$ ) values lower than that of previously mentioned composite materials. Even though the  $J_{sc}$  ( $11.83 mA/cm^2$ ) value was improved due to lower resistances, lower  $V_{oc}$  (0.84 V) value was observed (Fig. 4.14).

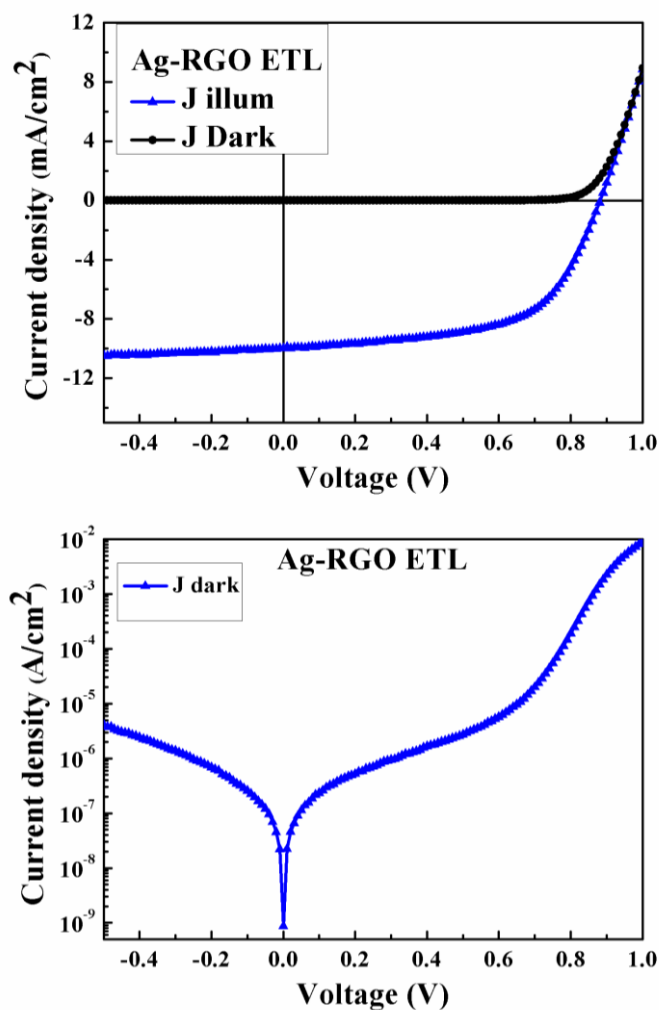


Figure 4.11: Photocurrent density (J) versus voltage (V) characteristics of polymer solar cell with Ag-RGO as electron transport layer and corresponding semi-logarithmic plot of the  $J_{\text{dark}}$ .

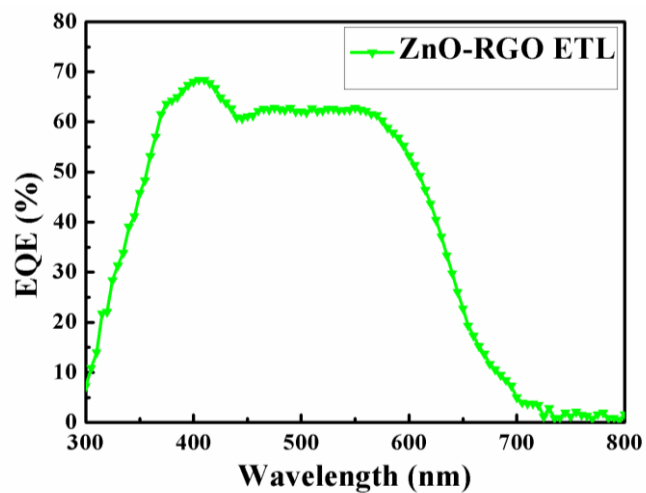
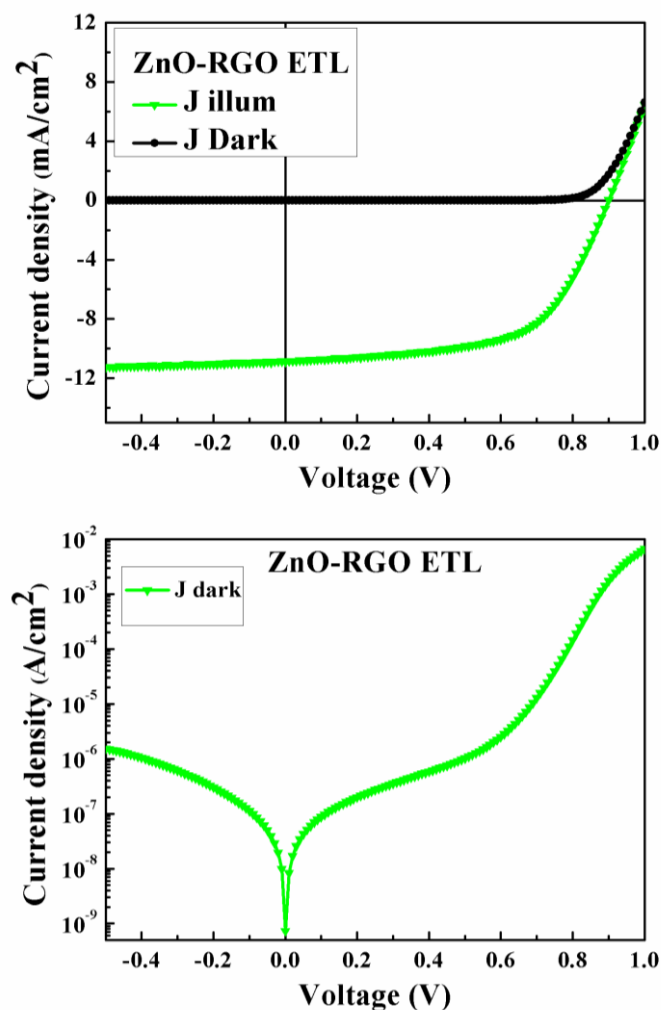


Figure 4.12: EQE spectrum of the polymer solar cell with ZnO-RGO ETL.



**Figure 4.13: Photocurrent density (J) versus voltage (V) characteristics of polymer solar cell with ZnO-RGO as electron transport layer and corresponding semi-logarithmic plot of the  $J_{\text{dark}}$ .**

The observations pertaining to Fig. 4.14 may be attributed to the charge accumulation at the interface which was observed in a S-shaped curve in DSSC. Since, EQE spectrum (Fig. 4.15) shows more than 60% photons within the wavelength range of 400 - 600 nm participated in charge generation after incidence on the solar cell. To further understand the interaction between photoactive layer and grapheneous materials, MLG is used as ETL, which resulted in a higher PEC value of 6.45%. The series resistance ( $R_s$ ) which is mainly a resultant of sum of bulk resistance of each layer was enormously decreased to 8.57  $\Omega/\text{cm}^2$ , but the shunt resistance ( $R_{\text{sh}}$ ) due the multilayered structure was found to be high (1730.75  $\Omega/\text{cm}^2$ ). The lower  $R_s$  value indicates that the MLG is compatible with the photoactive layer and Al back contact. As a result the EQE values crossed 65% between the wavelength range of 400 – 600 nm (Fig. 4.17), hence the photovoltaic characteristics have  $J_{\text{sc}}$  (11.83  $\text{mA}/\text{cm}^2$ ) and  $V_{\text{oc}}$  (0.84 V) also found to be improved along with higher FF of 65.1% (Fig. 4.16).

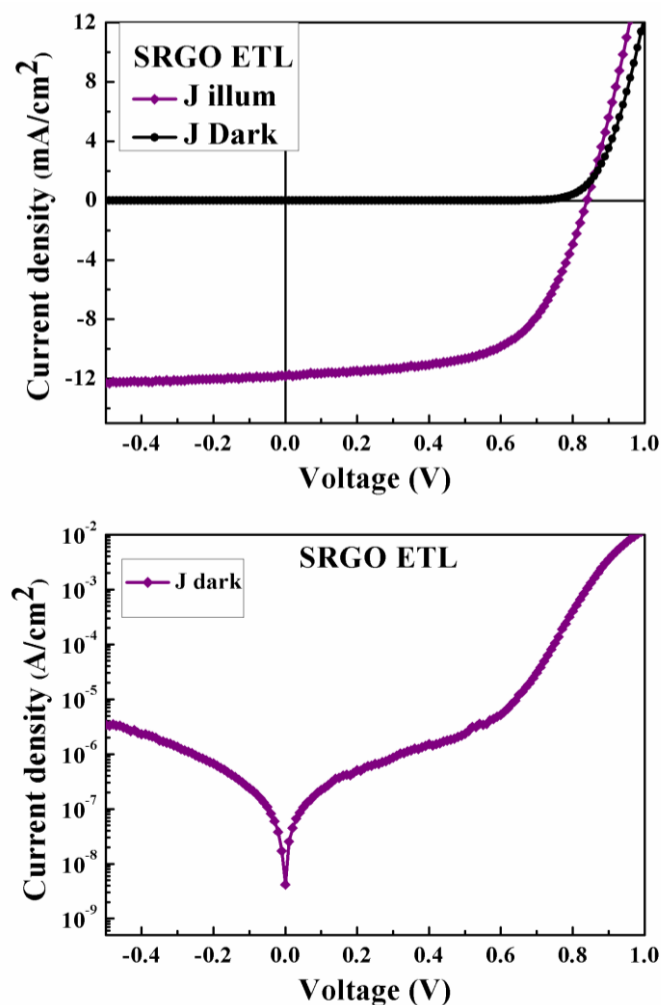


Figure 4.14: Photocurrent density (J) versus voltage (V) characteristics of polymer solar cell with SRGO as electron transport layer and corresponding semi-logarithmic plot of the  $J_{\text{dark}}$ .

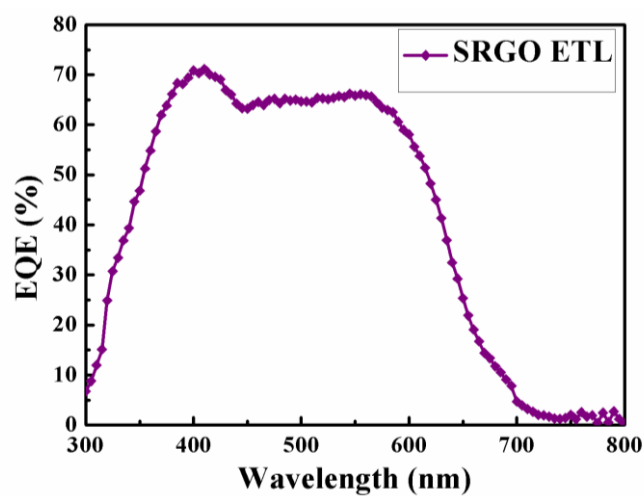


Figure 4.15: EQE spectrum of the polymer solar cell with SRGO ETL.

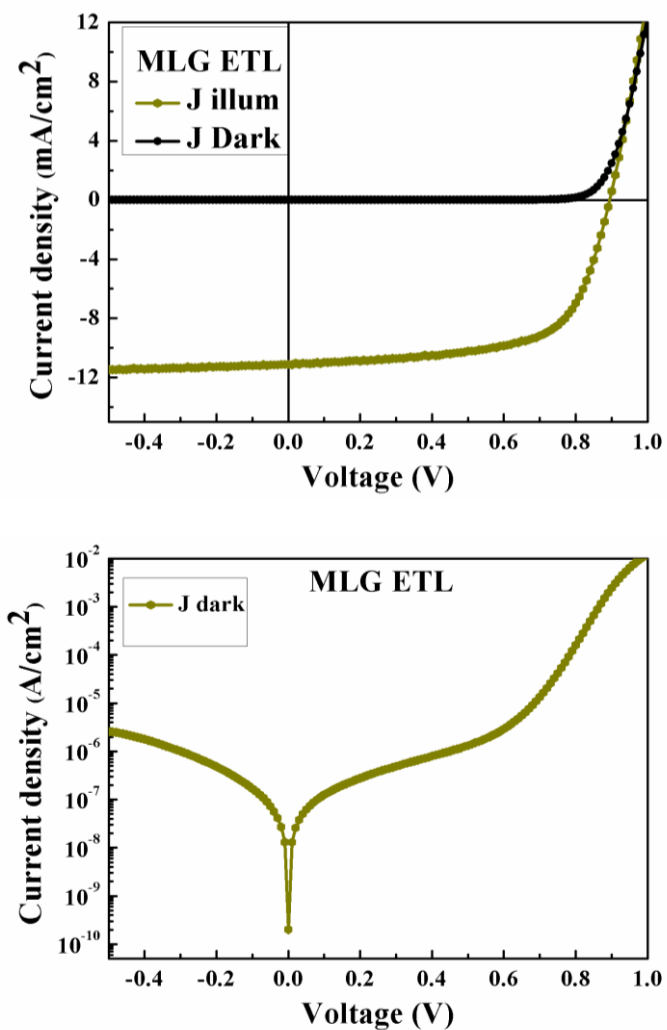


Figure 4.16: Photocurrent density (J) versus voltage (V) characteristics of polymer solar cell with MLG as electron transport layer and corresponding semi-logarithmic plot of the  $J_{\text{dark}}$ .

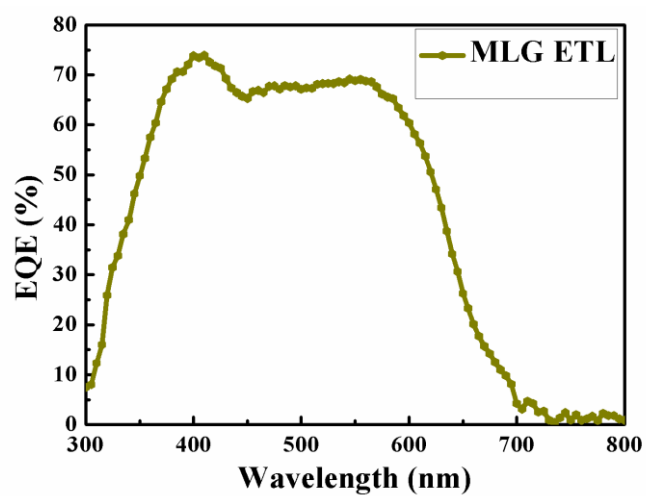
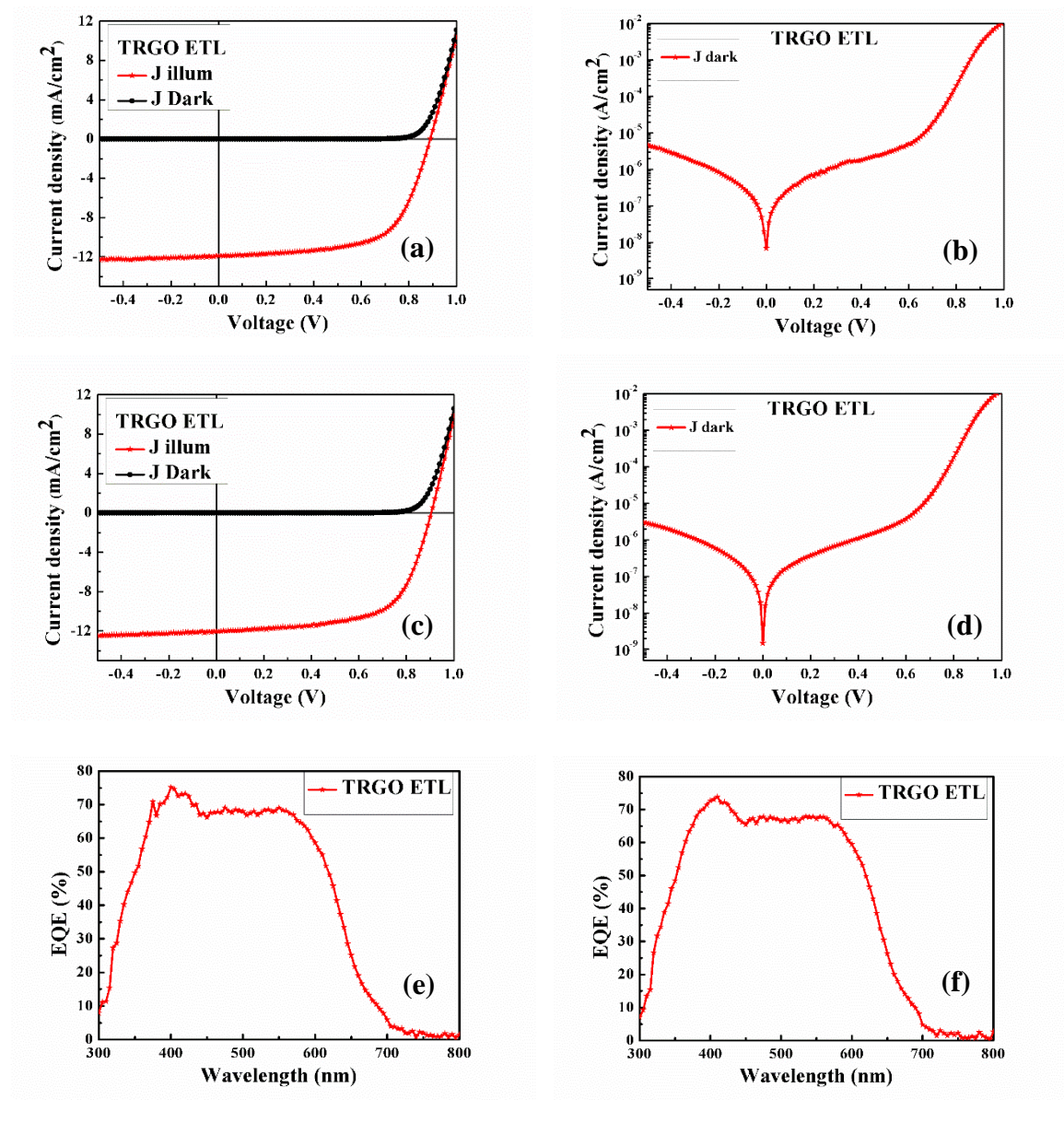


Figure 4.17: EQE spectrum of the polymer solar cell with MLG ETL.

## Results and Discussion

---

J-V characteristics of polymer solar cell with TRGO as ETL is showed in Fig. 4.18. The intermediate compound, graphene oxide (GO), used for getting the end product SRGO and TRGO was same, instead of subjecting the GO to solar reduction, it is subjected to heat treatment in a preheated furnace at 400 °C. TRGO exhibited almost same  $R_s$  ( $11.07 \Omega/\text{cm}^2$ ), but  $R_{sh}$  ( $614.52\Omega/\text{cm}^2$ ) value achieved was very low when compared to that of SRGO. These values clearly indicate that the band gap alignment is achieved in the device for smooth transfer of photo generated charge carrier between the active polymer layer and the Al back contact. It is observed that the OPV devices fabricated by depositing TRGO and TFLG dispersed in methanol as electron transport layers with spinning rates below 3000 rpm got short circuited indicating larger thickness of the ETL at few places making contact between the top (ITO) and bottom (Al) electrodes. The deposition of ETL with spinning speeds above 3500 rpm showed similar trend and efficiency as that of the devices without ETL indicating that there is no presence of the TRGO/TFLG on the active layer due to slipping off of the material from the active surface before adhesion at higher speeds. Hence the optimum speed fixed for the ETL deposition was at 3500 rpm. Further optimizing the spin coating rate to 3000 rpm to 3500 rpm improved the FF value from 63.8% to 64.1%, indicating the suitable fabrication condition of the solar cell, due to proper dispersion of the TRGO on active layer (Fig. 4.18). Hence, the  $J_{sc}$  and  $V_{oc}$  values are improved from  $11.91 \text{ mA}/\text{cm}^2$  to  $12.03 \text{ mA}/\text{cm}^2$  and 0.89V to 0.9V. Hence, improved PCE of 6.94% has been achieved with TRGO as ETL. The polymer solar cell characteristics obtained after optimization are given in Table 4.4.



**Figure 4.18:** Photocurrent density ( $J$ ) versus voltage ( $V$ ) characteristics of polymer solar cell with TRGO as electron transport layer, corresponding semi-logarithmic plots of the  $J_{\text{dark}}$  and EQE spectra (a, b & e) before optimization and (c, d & f) after optimization of spin coating speed.

**Table 4.4:** Comparison of the photovoltaic performance of the OSCs fabricated with different ETLs.

ETL Used	$V_{\text{oc}}$ (V)	$J_{\text{sc}}$ ( $\text{mA}/\text{cm}^2$ )	FF (%)	$\eta$ (%)	$R_s$ ( $\Omega/\text{cm}^2$ )	$R_{\text{sh}}$ ( $\Omega/\text{cm}^2$ )
TRGO	0.9	12.03	64.1	6.94	10.30	348.61
TFLG	0.9	12.37	64.1	7.14	10.18	451.97

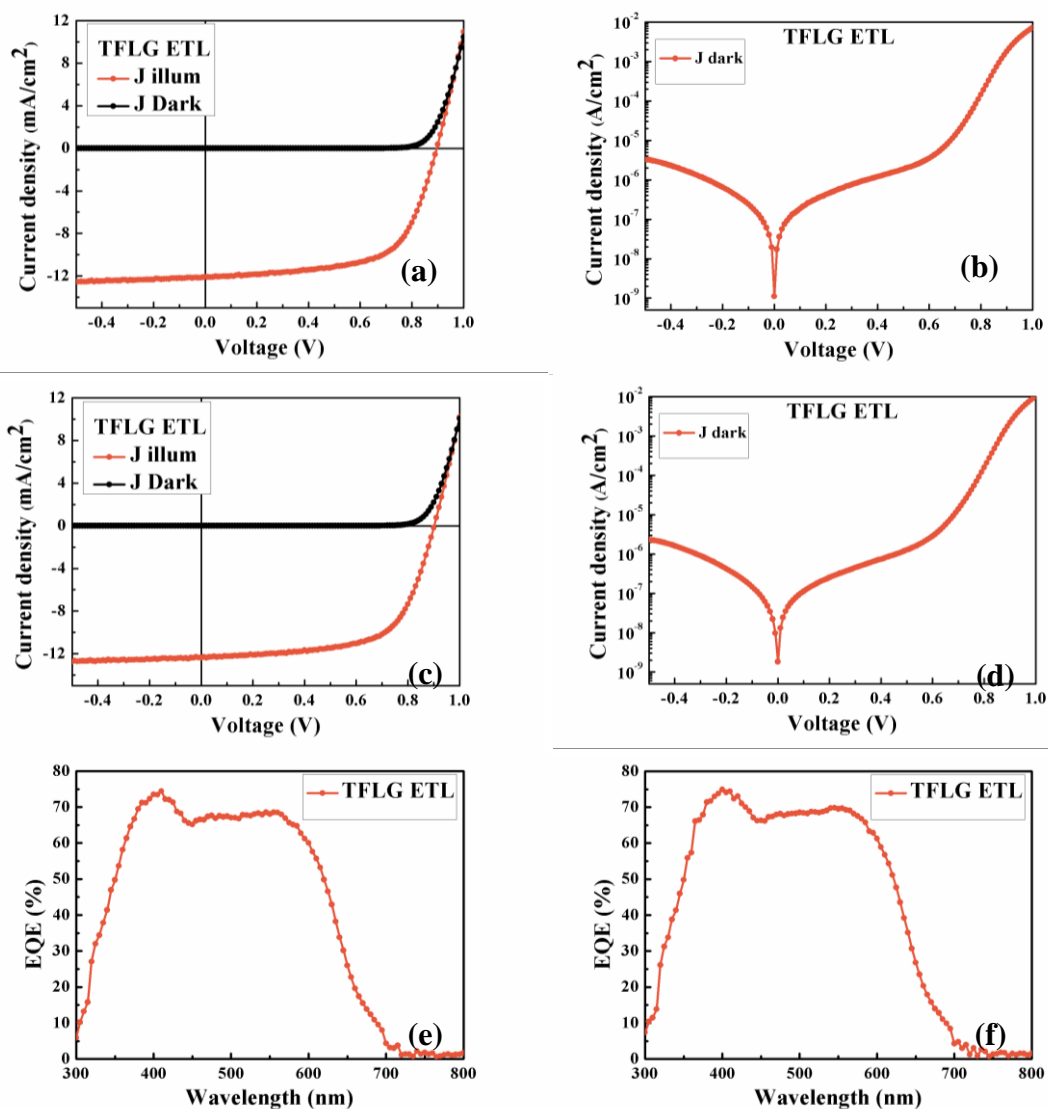


**Figure 4.19: Photocurrent density (J) versus voltage (V) characteristics of polymer solar cell with TFLG as electron transport layer, corresponding semi-logarithmic plot of the  $J_{\text{dark}}$  and EQE spectra (a, b & e) before optimization and (c, d & f) after optimization of spin coating speed.**

Similarly, FLG synthesized from thermal reduction of GO was used as ETL. The polymer solar cells fabricated with TFLG exhibited still lower values of  $R_s$  ( $9.98 \Omega/\text{cm}^2$ ) and  $R_{\text{sh}}$  ( $447.1 \Omega/\text{cm}^2$ ) upon optimization of spin coating the FF has improved from 63.4% to 64.1% resulting in improvement in solar cell characteristics  $V_{\text{oc}}$  (0.9V),  $J_{\text{sc}}$  ( $11.91 \text{mA}/\text{cm}^2$ ), hence highest PEC of 7.14% is achieved (Fig.4.19), indicating that the optimum solar cell configuration for these polymer solar cells is ITO/PEDOT:PSS/PCDTBT:PC<sub>70</sub>BM/TFLG/Al.

---

## Chapter 5 Conclusions and Future Aspects

### 5.1 Conclusions

Graphenaceous materials viz., Solar reduced graphene oxide (SRGO), Silver decorate reduced graphene Oxide (Ag-RGO), Zinc Oxide decorated Reduced Graphene Oxide (ZnO-RGO), Multilayered Graphene (MLG), Thermal reduced Few layered graphene (FLG) and Thermal reduced graphene oxide (TRGO) were synthesized using easy methods. The as-synthesized GO and SRGO materials are spray coated onto FTO glass substrates which were then used as CEs in DSSCs. In other words, Pt-free CEs were fabricated and used in DSSCs. The fabrication process used in this work to obtain DSSCs is not a complicated process in comparison to the other works in the literature. SRGO exhibited a more suitable electrochemical behavior than GO. The conversion efficiencies obtained in this work when GO and SRGO CEs are used in DSSCs are 3.38 and 3.96%, respectively. All the synthesized materials spin coated on the photosensitive BHJ layer by mixing them in methanol, which allow an ETL deposition at room temperature in the fabrication of the conventional ITO/PEDOT:PSS/PCDTBT:PC<sub>70</sub>BM/ETL/Al OSC device architecture, without need for further thermal treatment like conventional metal oxide precursors used to deposit metal oxides as ETLs, reducing the device degradation due to the heat treatment. All the materials enhanced the PCE of the OSCs while maximum PCE of 6.94% and 7.14% are achieved in the case of TRGO and TFLG, respectively, due to the optimal dispersion of TRGO and TFLG creating maximum percolation pathways to the electrons to the back Al contact resulting in extraction of charges from the active layer with minimum recombination.

### 5.2 Future Aspects

This thesis work can be extended to develop large area photovoltaic devices which reduces the processing costs and making large area processing a possibility. With the as prepared Graphenaceous carbon materials can be used to enabling integration of the energy harvesting and storage technologies. Since, the same Graphenaceous materials are used as electrodes in energy storage devices like supercapacitors, batteries, fuel cells etc., integration of the fabricated solar cells with energy storage devices helps in fabricating low carbon, higher performance green energy generators and efficient energy storage devices with higher specific energy and power densities. Above mentioned integrated devices, makes the devices overcome intermittent power back up problem, load levelers, renewable energy storage systems and electrification of transport systems to ubiquitous portable electronic devices, energy storage

## Conclusions and Future Aspects

systems. The energy storage device is the crucial link between energy generating devices (e.g. Solar PV) and energy utilization. In recent years, the conductivity, surface area and form factor of carbon nanomaterials, such as graphene and carbon nanotubes, have also shown great potential for energy storage applications. These carbon materials are also attracting interest as electrode materials for electrochemical capacitors, because of their high surface area, electrical conductivity, chemical stability and functionality, and low cost. In both cases the carbon nanomaterials will be used for charge transport and physical support scaffolds between the electrodes as required. The extension of this work is demonstrating integrated carbon nanomaterial based scaffolds for an electricity generation and storage system can be identified to provide a format for defining the required properties of the carbon scaffolds.

**Table 5.1: Different grapenaceous materials useful in development of future solar cells.**

ETL Used	$\eta$ (%)	Future aspects	Research area
Ag-RGO	5.21	Further study and experimentation is required to know how the weight percentage of metal oxides/metals effects the improvement of light coupling to further enhance efficiency of the solar cells.	Building Integrated Photovoltaics
ZnO-RGO	5.86		
SRGO	5.93	Chemical treatment methods to further control the porosity in these materials needs a further investigation for improved charge exchange mechanisms at the interface between these materials and ions in the electrolytes.	DSSCs and Perovskite Solar Cells
MLG	6.45		
TRGO	6.94	Work function tenability of these materials during chemical treatments for functionalization and composition formation needs to be addressed for optimal percolation with low roughness at the interface with different organic photoactive materials in the solar cells.	Organic Photovoltaic Devices
TFLG	7.14		

The above studies must lead to fabrications of solar cells with PCE of at least 10%.

---

## References

- [1] U. S. E. I. Administration, “Energy Information Administration,” 2006.
- [2] K. Watkins, “Human Development Report,” 2006.
- [3] M. Z. Jacobson and M. A. Delucchi, “Providing all global energy with wind, water, and solar power, Part I: Technologies, energy resources, quantities and areas of infrastructure, and materials,” *Energy Policy*, vol. 39, no. 3, pp. 1154–1169, Mar. 2011.
- [4] M. Z. Jacobson, M. A. Delucchi, G. Bazouin, Z. A. F. Bauer, C. C. Heavey, E. Fisher, S. B. Morris, D. J. Y. Piekutowski, T. A. Vencill, and T. W. Yeskoo, “100% clean and renewable wind, water, and sunlight (WWS) all-sector energy roadmaps for the 50 United States,” *Energy & Environmental Science*, vol. 8, no. 7, pp. 2093–2117, 2015.
- [5] Nrel, “<http://www.nrel.gov/gis/solar.html>.”
- [6] EIA, “World energy outlook,” 2013.
- [7] Worldometers, “World population milestones.”
- [8] BMU, “Federal ministry for the environment, nature conservation and nuclear safety,” 2014.
- [9] M. A. Green, K. Emery, Y. Hishikawa, W. Warta, and E. D. Dunlop, “Solar cell efficiency tables (version 40),” *Progress in Photovoltaics: Research and Applications*, vol. 20, no. 5, pp. 606–614, Aug. 2012.
- [10] N. Kaur, M. Singh, D. Pathak, T. Wagner, and J. M. Nunzi, “Organic materials for photovoltaic applications: Review and mechanism,” *Synthetic Metals*, vol. 190, pp. 20–26, Apr. 2014.
- [11] Inspect, “Inspect.” 2012.
- [12] Sunherald.com, “Konarka technologies advances award winning power plastic cell efficiency with 9 percent certification,” p. 02, 2012.
- [13] Z. Fan, H. Razavi, J. Do, A. Moriwaki, O. Ergen, Y.-L. Chueh, P. W. Leu, J. C. Ho, T. Takahashi, L. A. Reichertz, S. Neale, K. Yu, M. Wu, J. W. Ager, and A. Javey, “Three-dimensional nanopillar-array photovoltaics on low-cost and flexible substrates,” *Nature Materials*, vol. 8, no. 8, pp. 648–653, Aug. 2009.
- [14] F. Priolo, T. Gregorkiewicz, M. Galli, and T. F. Krauss, “Silicon nanostructures for photonics and photovoltaics,” *Nature Nanotechnology*, vol. 9, no. 1, pp. 19–32, Jan. 2014.
- [15] Nrel, “nrel.”
- [16] H. Choi, H. Kim, S. Hwang, Y. Han, and M. Jeon, “Graphene counter electrodes for dye-sensitized solar cells prepared by electrophoretic deposition,” *Journal of Materials Chemistry*, vol. 21, no. 21, p. 7548, 2011.
- [17] F. Gong, Z. Li, H. Wang, and Z.-S. Wang, “Enhanced electrocatalytic performance of graphene via incorporation of SiO<sub>2</sub> nanoparticles for dye-sensitized solar cells,” *Journal of Materials Chemistry*, vol. 22, no. 33, p. 17321, 2012.
- [18] M.-H. Yeh, L.-Y. Lin, L.-Y. Chang, Y.-A. Leu, W.-Y. Cheng, J.-J. Lin, and K.-C. Ho, “Dye-Sensitized Solar Cells with Reduced Graphene Oxide as the Counter Electrode Prepared by a Green Photothermal Reduction Process,” *ChemPhysChem*, vol. 15, no. 6, pp. 1175–1181, Apr. 2014.
- [19] S. Casaluci, M. Gemmi, V. Pellegrini, A. Di Carlo, and F. Bonaccorso, “Graphene-based large area dye-sensitized solar cell modules,” *Nanoscale*, vol. 8, no. 9, pp. 5368–5378, 2016.
- [20] K. Kakiage, Y. Aoyama, T. Yano, K. Oya, J. Fujisawa, and M. Hanaya, “Highly-efficient dye-sensitized solar cells with collaborative sensitization by silyl-anchor and carboxy-anchor dyes,” *Chemical Communications*, vol. 51, no. 88, pp. 15894–15897, 2015.

## References

---

- [21] P. W. M. Blom, V. D. Mihailetschi, L. J. A. Koster, and D. E. Markov, "Device Physics of Polymer:Fullerene Bulk Heterojunction Solar Cells," *Advanced Materials*, vol. 19, no. 12, pp. 1551–1566, Jun. 2007.
- [22] H. B. Michaelson, "The work function of the elements and its periodicity," *Journal of Applied Physics*, vol. 48, no. 11, pp. 4729–4733, Nov. 1977.
- [23] M. Jørgensen, K. Norrman, and F. C. Krebs, "Stability/degradation of polymer solar cells," *Solar Energy Materials and Solar Cells*, vol. 92, no. 7, pp. 686–714, Jul. 2008.
- [24] J. Y. Kim, S. H. Kim, H.-H. Lee, K. Lee, W. Ma, X. Gong, and A. J. Heeger, "New Architecture for High-Efficiency Polymer Photovoltaic Cells Using Solution-Based Titanium Oxide as an Optical Spacer," *Advanced Materials*, vol. 18, no. 5, pp. 572–576, Mar. 2006.
- [25] Y. Sun, J. H. Seo, C. J. Takacs, J. Seifert, and A. J. Heeger, "Inverted Polymer Solar Cells Integrated with a Low-Temperature-Annealed Sol-Gel-Derived ZnO Film as an Electron Transport Layer," *Advanced Materials*, vol. 23, no. 14, pp. 1679–1683, Apr. 2011.
- [26] A. Roy, S. H. Park, S. Cowan, M. H. Tong, S. Cho, K. Lee, and A. J. Heeger, "Titanium suboxide as an optical spacer in polymer solar cells," *Applied Physics Letters*, vol. 95, no. 1, p. 013302, Jul. 2009.
- [27] G. Yu, J. Gao, J. C. Hummelen, F. Wudl, and A. J. Heeger, "Polymer Photovoltaic Cells: Enhanced Efficiencies via a Network of Internal Donor-Acceptor Heterojunctions," *Science*, vol. 270, no. 5243, pp. 1789–1791, Dec. 1995.
- [28] B. A. Collins, Z. Li, J. R. Tumbleston, E. Gann, C. R. McNeill, and H. Ade, "Absolute Measurement of Domain Composition and Nanoscale Size Distribution Explains Performance in PTB7:PC 71 BM Solar Cells," *Advanced Energy Materials*, vol. 3, no. 1, pp. 65–74, Jan. 2013.
- [29] H. Hoppe and N. S. Sariciftci, "Morphology of polymer/fullerene bulk heterojunction solar cells," *J. Mater. Chem.*, vol. 16, no. 1, pp. 45–61, 2006.
- [30] K. D. G. I. Jayawardena, L. J. Rozanski, C. A. Mills, M. J. Beliatas, N. A. Nismy, and S. R. P. Silva, "Inorganics-in-Organics': recent developments and outlook for 4G polymer solar cells," *Nanoscale*, vol. 5, no. 18, p. 8411, 2013.
- [31] U. S. G. Survey and F. S. 087-02, "U.S. Geological Survey Fact Sheet 087-02." .
- [32] M. A. Green, K. Emery, Y. Hishikawa, W. Warta, and E. D. Dunlop, "Solar cell efficiency tables (version 47)," *Progress in Photovoltaics: Research and Applications*, vol. 24, no. 1, pp. 3–11, Jan. 2016.
- [33] P. Campbell and M. A. Green, "High performance light trapping textures for monocrystalline silicon solar cells," *Solar Energy Materials and Solar Cells*, vol. 65, no. 1–4, pp. 369–375, Jan. 2001.
- [34] C. F. Bohren and D. R. Huffman, *Absorption and Scattering of Light by Small Particles*. John Wiley & Sons.
- [35] M. L. Brongersma, Y. Cui, and S. Fan, "Light management for photovoltaics using high-index nanostructures," *Nature Materials*, vol. 13, no. 5, pp. 451–460, May 2014.
- [36] P. Spinelli, M. A. Verschuuren, and A. Polman, "Broadband omnidirectional antireflection coating based on subwavelength surface Mie resonators," *Nature Communications*, vol. 3, no. 1, p. 692, Jan. 2012.
- [37] K. R. Catchpole and A. Polman, "Design principles for particle plasmon enhanced solar cells," *Applied Physics Letters*, vol. 93, no. 19, p. 191113, Nov. 2008.
- [38] P. Spinelli, B. Macco, M. A. Verschuuren, W. M. M. Kessels, and A. Polman, "Al<sub>2</sub>O<sub>3</sub>/TiO<sub>2</sub> nano-pattern antireflection coating with ultralow surface recombination," *Applied Physics Letters*, vol. 102, no. 23, p. 233902, Jun. 2013.

## References

---

- [39] J. van de Groep, P. Spinelli, and A. Polman, "Transparent Conducting Silver Nanowire Networks," *Nano Letters*, vol. 12, no. 6, pp. 3138–3144, Jun. 2012.
- [40] S. Mokkaapati, F. J. Beck, A. Polman, and K. R. Catchpole, "Designing periodic arrays of metal nanoparticles for light-trapping applications in solar cells," *Applied Physics Letters*, vol. 95, no. 5, p. 053115, Aug. 2009.
- [41] V. E. Ferry, M. A. Verschuuren, M. C. van Lare, R. E. I. Schropp, H. A. Atwater, and A. Polman, "Optimized Spatial Correlations for Broadband Light Trapping Nanopatterns in High Efficiency Ultrathin Film a-Si:H Solar Cells," *Nano Letters*, vol. 11, no. 10, pp. 4239–4245, Oct. 2011.
- [42] A. J. Morfa, K. L. Rowlen, T. H. Reilly, M. J. Romero, and J. van de Lagemaat, "Plasmon-enhanced solar energy conversion in organic bulk heterojunction photovoltaics," *Applied Physics Letters*, vol. 92, no. 1, p. 013504, 2008.
- [43] G. Dingemans and W. M. M. Kessels, "Status and prospects of Al<sub>2</sub>O<sub>3</sub>-based surface passivation schemes for silicon solar cells," *Journal of Vacuum Science & Technology A: Vacuum, Surfaces, and Films*, vol. 30, no. 4, p. 040802, Jul. 2012.
- [44] P. Spinelli, M. Hebbink, R. de Waele, L. Black, F. Lenzmann, and A. Polman, "Optical Impedance Matching Using Coupled Plasmonic Nanoparticle Arrays," *Nano Letters*, vol. 11, no. 4, pp. 1760–1765, Apr. 2011.
- [45] P. Spinelli and A. Polman, "Light Trapping in Thin Crystalline Si Solar Cells Using Surface Mie Scatterers," *IEEE Journal of Photovoltaics*, vol. 4, no. 2, pp. 554–559, Mar. 2014.
- [46] P. Spinelli, F. Lenzmann, A. Weeber, and A. Polman, "Effect of EVA Encapsulation on Antireflection Properties of Mie Nanoscatterers for c-Si Solar Cells," *IEEE Journal of Photovoltaics*, vol. 5, no. 2, pp. 559–564, Mar. 2015.
- [47] T. C. Sum and N. Mathews, "Advancements in perovskite solar cells: photophysics behind the photovoltaics," *Energy Environ. Sci.*, vol. 7, no. 8, pp. 2518–2534, 2014.
- [48] A. Kojima, K. Teshima, Y. Shirai, and T. Miyasaka, "Organometal Halide Perovskites as Visible-Light Sensitizers for Photovoltaic Cells," *Journal of the American Chemical Society*, vol. 131, no. 17, pp. 6050–6051, May 2009.
- [49] J.-H. Im, C.-R. Lee, J.-W. Lee, S.-W. Park, and N.-G. Park, "6.5% efficient perovskite quantum-dot-sensitized solar cell," *Nanoscale*, vol. 3, no. 10, p. 4088, 2011.
- [50] H.-S. Kim, C.-R. Lee, J.-H. Im, K.-B. Lee, T. Moehl, A. Marchioro, S.-J. Moon, R. Humphry-Baker, J.-H. Yum, J. E. Moser, M. Grätzel, and N.-G. Park, "Lead Iodide Perovskite Sensitized All-Solid-State Submicron Thin Film Mesoscopic Solar Cell with Efficiency Exceeding 9%," *Scientific Reports*, vol. 2, no. 1, p. 591, Dec. 2012.
- [51] H.-S. Kim, J.-W. Lee, N. Yantara, P. P. Boix, S. A. Kulkarni, S. Mhaisalkar, M. Grätzel, and N.-G. Park, "High Efficiency Solid-State Sensitized Solar Cell-Based on Submicrometer Rutile TiO<sub>2</sub> Nanorod and CH<sub>3</sub>NH<sub>3</sub>PbI<sub>3</sub> Perovskite Sensitizer," *Nano Letters*, vol. 13, no. 6, pp. 2412–2417, Jun. 2013.
- [52] L. Etgar, P. Gao, Z. Xue, Q. Peng, A. K. Chandiran, B. Liu, M. K. Nazeeruddin, and M. Grätzel, "Mesoscopic CH<sub>3</sub>NH<sub>3</sub>PbI<sub>3</sub>/TiO<sub>2</sub> Heterojunction Solar Cells," *Journal of the American Chemical Society*, vol. 134, no. 42, pp. 17396–17399, Oct. 2012.
- [53] W. A. Laban and L. Etgar, "Depleted hole conductor-free lead halide iodide heterojunction solar cells," *Energy & Environmental Science*, vol. 6, no. 11, p. 3249, 2013.
- [54] M. M. Lee, J. Teuscher, T. Miyasaka, T. N. Murakami, and H. J. Snaith, "Efficient Hybrid Solar Cells Based on Meso-Superstructured Organometal Halide Perovskites," *Science*, vol. 338, no. 6107, pp. 643–647, Nov. 2012.

## References

---

- [55] J. M. Ball, M. M. Lee, A. Hey, and H. J. Snaith, "Low-temperature processed meso-superstructured to thin-film perovskite solar cells," *Energy & Environmental Science*, vol. 6, no. 6, p. 1739, 2013.
- [56] M. J. Carnie, C. Charbonneau, M. L. Davies, J. Troughton, T. M. Watson, K. Wojciechowski, H. Snaith, and D. A. Worsley, "A one-step low temperature processing route for organolead halide perovskite solar cells," *Chemical Communications*, vol. 49, no. 72, p. 7893, 2013.
- [57] K. Wojciechowski, M. Saliba, T. Leijtens, A. Abate, and H. J. Snaith, "Sub-150 °C processed meso-superstructured perovskite solar cells with enhanced efficiency," *Energy Environ. Sci.*, vol. 7, no. 3, pp. 1142–1147, 2014.
- [58] A. Swarnkar, A. R. Marshall, E. M. Sanehira, B. D. Chernomordik, D. T. Moore, J. A. Christians, T. Chakrabarti, and J. M. Luther, "Quantum dot-induced phase stabilization of -CsPbI<sub>3</sub> perovskite for high-efficiency photovoltaics," *Science*, vol. 354, no. 6308, pp. 92–95, Oct. 2016.
- [59] A. Mei, X. Li, L. Liu, Z. Ku, T. Liu, Y. Rong, M. Xu, M. Hu, J. Chen, Y. Yang, M. Grätzel, and H. Han, "A hole-conductor-free, fully printable mesoscopic perovskite solar cell with high stability," *Science*, vol. 345, no. 6194, pp. 295–298, Jul. 2014.
- [60] J. Burschka, N. Pellet, S.-J. Moon, R. Humphry-Baker, P. Gao, M. K. Nazeeruddin, and M. Grätzel, "Sequential deposition as a route to high-performance perovskite-sensitized solar cells," *Nature*, vol. 499, no. 7458, pp. 316–319, Jul. 2013.
- [61] J.-H. Im, I.-H. Jang, N. Pellet, M. Grätzel, and N.-G. Park, "Growth of CH<sub>3</sub>NH<sub>3</sub>PbI<sub>3</sub> cuboids with controlled size for high-efficiency perovskite solar cells," *Nature Nanotechnology*, vol. 9, no. 11, pp. 927–932, Nov. 2014.
- [62] M. Saliba, T. Matsui, J.-Y. Seo, K. Domanski, J.-P. Correa-Baena, M. K. Nazeeruddin, S. M. Zakeeruddin, W. Tress, A. Abate, A. Hagfeldt, and M. Grätzel, "Cesium-containing triple cation perovskite solar cells: improved stability, reproducibility and high efficiency," *Energy & Environmental Science*, vol. 9, no. 6, pp. 1989–1997, 2016.
- [63] F. Hao, C. C. Stoumpos, D. H. Cao, R. P. H. Chang, and M. G. Kanatzidis, "Lead-free solid-state organic–inorganic halide perovskite solar cells," *Nature Photonics*, vol. 8, no. 6, pp. 489–494, Jun. 2014.
- [64] N. K. Noel, S. D. Stranks, A. Abate, C. Wehrenfennig, S. Guarnera, A.-A. Haghighirad, A. Sadhanala, G. E. Eperon, S. K. Pathak, M. B. Johnston, A. Petrozza, L. M. Herz, and H. J. Snaith, "Lead-free organic–inorganic tin halide perovskites for photovoltaic applications," *Energy Environ. Sci.*, vol. 7, no. 9, pp. 3061–3068, 2014.
- [65] B. Murali and S. B. Krupanidhi, "Transport properties of CuIn<sub>1-x</sub>Al<sub>x</sub>Se<sub>2</sub>/AZnO heterostructure for low cost thin film photovoltaics," *Dalton Trans.*, vol. 43, no. 5, pp. 1974–1983, 2014.
- [66] F. C. Krebs, "Fabrication and processing of polymer solar cells: A review of printing and coating techniques," *Solar Energy Materials and Solar Cells*, vol. 93, no. 4, pp. 394–412, Apr. 2009.
- [67] R. R. Søndergaard, M. Hösel, and F. C. Krebs, "Roll-to-Roll fabrication of large area functional organic materials," *Journal of Polymer Science Part B: Polymer Physics*, vol. 51, no. 1, pp. 16–34, Jan. 2013.
- [68] Z. Abdin, M. A. Alim, R. Saidur, M. R. Islam, W. Rashmi, S. Mekhilef, and A. Wadi, "Solar energy harvesting with the application of nanotechnology," *Renewable and Sustainable Energy Reviews*, vol. 26, pp. 837–852, Oct. 2013.
- [69] J. Zhao, Y. Li, G. Yang, K. Jiang, H. Lin, H. Ade, W. Ma, and H. Yan, "Efficient organic solar cells processed from hydrocarbon solvents," *Nature Energy*, vol. 1, no. 2, p. 15027, Jan. 2016.

## References

---

- [70] M. A. GREEN, *Third Generation Photovoltaics*, vol. 12. Springer Berlin Heidelberg, 2006.
- [71] B. O'Regan and M. Grätzel, "A low-cost, high-efficiency solar cell based on dye-sensitized colloidal TiO<sub>2</sub> films," *Nature*, vol. 353, no. 6346, pp. 737–740, Oct. 1991.
- [72] M. Grätzel, "Dye-sensitized solar cells," *Journal of Photochemistry and Photobiology C: Photochemistry Reviews*, vol. 4, no. 2, pp. 145–153, Oct. 2003.
- [73] C. Cornaro and A. Andreotti, "Influence of Average Photon Energy index on solar irradiance characteristics and outdoor performance of photovoltaic modules," *Progress in Photovoltaics: Research and Applications*, p. n/a–n/a, Apr. 2012.
- [74] J. Wu, Z. Lan, J. Lin, M. Huang, Y. Huang, L. Fan, and G. Luo, "Electrolytes in Dye-Sensitized Solar Cells," *Chemical Reviews*, vol. 115, no. 5, pp. 2136–2173, Mar. 2015.
- [75] B.-K. Koo, D.-Y. Lee, H.-J. Kim, W.-J. Lee, J.-S. Song, and H.-J. Kim, "Seasoning effect of dye-sensitized solar cells with different counter electrodes," *Journal of Electroceramics*, vol. 17, no. 1, pp. 79–82, Sep. 2006.
- [76] A. Agresti, S. Pescetelli, E. Gatto, M. Venanzi, and A. Di Carlo, "Polyiodides formation in solvent based Dye Sensitized Solar Cells under reverse bias stress," *Journal of Power Sources*, vol. 287, pp. 87–95, Aug. 2015.
- [77] J. Xia, N. Masaki, M. Lira-Cantu, Y. Kim, K. Jiang, and S. Yanagida, "Influence of Doped Anions on Poly(3,4-ethylenedioxythiophene) as Hole Conductors for Iodine-Free Solid-State Dye-Sensitized Solar Cells," *Journal of the American Chemical Society*, vol. 130, no. 4, pp. 1258–1263, Jan. 2008.
- [78] W. Brütting, "Introduction to the Physics of Organic Semiconductors," in *Physics of Organic Semiconductors*, Weinheim, FRG: Wiley-VCH Verlag GmbH & Co. KGaA, 2006, pp. 1–14.
- [79] Q. P. W. Atkins, *A Handbook of Concepts*, 2nd editio. Oxford University Press.
- [80] J.-L. Bredas, "Mind the gap!," *Mater. Horiz.*, vol. 1, no. 1, pp. 17–19, 2014.
- [81] H.-W. Li, Z. Guan, Y. Cheng, T. Lui, Q. Yang, C.-S. Lee, S. Chen, and S.-W. Tsang, "On the Study of Exciton Binding Energy with Direct Charge Generation in Photovoltaic Polymers," *Advanced Electronic Materials*, vol. 2, no. 11, p. 1600200, Nov. 2016.
- [82] F. Gao and O. Inganäs, "Charge generation in polymer–fullerene bulk-heterojunction solar cells," *Phys. Chem. Chem. Phys.*, vol. 16, no. 38, pp. 20291–20304, Jul. 2014.
- [83] C. W. Tang, "Two-layer organic photovoltaic cell," *Applied Physics Letters*, vol. 48, no. 2, pp. 183–185, Jan. 1986.
- [84] J. J. M. Halls, K. Pichler, R. H. Friend, S. C. Moratti, and A. B. Holmes, "Exciton diffusion and dissociation in a poly(p-phenylenevinylene)/C<sub>60</sub> heterojunction photovoltaic cell," *Applied Physics Letters*, vol. 68, no. 22, pp. 3120–3122, May 1996.
- [85] D. E. Markov, E. Amsterdam, P. W. M. Blom, A. B. Sieval, and J. C. Hummelen, "Accurate Measurement of the Exciton Diffusion Length in a Conjugated Polymer Using a Heterostructure with a Side-Chain Cross-Linked Fullerene Layer," *The Journal of Physical Chemistry A*, vol. 109, no. 24, pp. 5266–5274, Jun. 2005.
- [86] L. Dou, J. You, Z. Hong, Z. Xu, G. Li, R. A. Street, and Y. Yang, "25th Anniversary Article: A Decade of Organic/Polymeric Photovoltaic Research," *Advanced Materials*, vol. 25, no. 46, pp. 6642–6671, Dec. 2013.
- [87] M. Hiramoto, H. Fujiwara, and M. Yokoyama, "Three-layered organic solar cell with a photoactive interlayer of codeposited pigments," *Applied Physics Letters*, vol. 58, no. 10, pp. 1062–1064, Mar. 1991.
- [88] A. H. N. Sariciftci, "Conjugated polymer - acceptor heterojunctions; diodes, photodiodes, and photovoltaic cells." US Patent, 1994.

## References

---

- [89] J. J. M. Halls, C. A. Walsh, N. C. Greenham, E. A. Marseglia, R. H. Friend, S. C. Moratti, and A. B. Holmes, "Efficient photodiodes from interpenetrating polymer networks," *Nature*, vol. 376, no. 6540, pp. 498–500, Aug. 1995.
- [90] P. W. M. Blom, V. D. Mihailetschi, L. J. A. Koster, and D. E. Markov, "Device Physics of Polymer:Fullerene Bulk Heterojunction Solar Cells," *Advanced Materials*, vol. 19, no. 12, pp. 1551–1566, Jun. 2007.
- [91] M. Narayan and J. Singh, "Photovoltaic contribution of photo-generated excitons in acceptor material of organic solar cells," *Journal of Materials Science: Materials in Electronics*, vol. 28, no. 10, pp. 7070–7076, May 2017.
- [92] D. L. Dexter, "A Theory of Sensitized Luminescence in Solids," *The Journal of Chemical Physics*, vol. 21, no. 5, pp. 836–850, May 1953.
- [93] D. L. Dexter, R. S. Knox, and T. Förster, "The Radiationless Transfer of Energy of Electronic Excitation between Impurity Molecules in Crystals," *physica status solidi (b)*, vol. 34, no. 2, pp. K159–K162, 1969.
- [94] B. Kippelen and J.-L. Brédas, "Organic photovoltaics," *Energy & Environmental Science*, vol. 2, no. 3, p. 251, 2009.
- [95] J. Nelson, "Organic photovoltaic films," *Current Opinion in Solid State and Materials Science*, vol. 6, no. 1, pp. 87–95, Feb. 2002.
- [96] M. Rita Narayan and J. Singh, "Study of the mechanism and rate of exciton dissociation at the donor-acceptor interface in bulk-heterojunction organic solar cells," *Journal of Applied Physics*, vol. 114, no. 7, p. 073510, Aug. 2013.
- [97] T. M. Clarke and J. R. Durrant, "Charge Photogeneration in Organic Solar Cells," *Chemical Reviews*, vol. 110, no. 11, pp. 6736–6767, Nov. 2010.
- [98] C. Deibel, T. Strobel, and V. Dyakonov, "Role of the Charge Transfer State in Organic Donor-Acceptor Solar Cells," *Advanced Materials*, vol. 22, no. 37, pp. 4097–4111, Aug. 2010.
- [99] W. Tress, *Organic Solar Cells Theory, Experiment, and Device Simulation*. Springer International Publishing, 2014.
- [100] J. D. Servaites, M. A. Ratner, and T. J. Marks, "Organic solar cells: A new look at traditional models," *Energy & Environmental Science*, vol. 4, no. 11, p. 4410, 2011.
- [101] D. Gupta, S. Mukhopadhyay, and K. S. Narayan, "Fill factor in organic solar cells," *Solar Energy Materials and Solar Cells*, vol. 94, no. 8, pp. 1309–1313, Aug. 2010.
- [102] N. K. Elumalai and A. Uddin, "Open circuit voltage of organic solar cells: an in-depth review," *Energy & Environmental Science*, vol. 9, no. 2, pp. 391–410, 2016.
- [103] J. C. Blakesley and D. Neher, "Relationship between energetic disorder and open-circuit voltage in bulk heterojunction organic solar cells," *Physical Review B*, vol. 84, no. 7, p. 075210, Aug. 2011.
- [104] M. C. Scharber, D. Mühlbacher, M. Koppe, P. Denk, C. Waldauf, A. J. Heeger, and C. J. Brabec, "Design Rules for Donors in Bulk-Heterojunction Solar Cells—Towards 10 % Energy-Conversion Efficiency," *Advanced Materials*, vol. 18, no. 6, pp. 789–794, Mar. 2006.
- [105] Y. He, H.-Y. Chen, J. Hou, and Y. Li, "Indene–C 60 Bisadduct: A New Acceptor for High-Performance Polymer Solar Cells," *Journal of the American Chemical Society*, vol. 132, no. 4, pp. 1377–1382, Feb. 2010.
- [106] Y. He, G. Zhao, B. Peng, and Y. Li, "High-Yield Synthesis and Electrochemical and Photovoltaic Properties of Indene-C70 Bisadduct," *Advanced Functional Materials*, vol. 20, no. 19, pp. 3383–3389, Oct. 2010.
- [107] M. Lenes, G.-J. A. H. Wetzelaer, F. B. Kooistra, S. C. Veenstra, J. C. Hummelen, and P. W. M. Blom, "Fullerene Bisadducts for Enhanced Open-Circuit Voltages and

## References

---

- Efficiencies in Polymer Solar Cells,” *Advanced Materials*, vol. 20, no. 11, pp. 2116–2119, Jun. 2008.
- [108] Q. Xu, F. Wang, Z. Tan, L. Li, S. Li, X. Hou, G. Sun, X. Tu, J. Hou, and Y. Li, “High-Performance Polymer Solar Cells with Solution-Processed and Environmentally Friendly CuO x Anode Buffer Layer,” *ACS Applied Materials & Interfaces*, vol. 5, no. 21, pp. 10658–10664, Nov. 2013.
- [109] J. Liu, Y. Shi, and Y. Yang, “Solvation-Induced Morphology Effects on the Performance of Polymer-Based Photovoltaic Devices,” *Advanced Functional Materials*, vol. 11, no. 6, p. 420, Dec. 2001.
- [110] A. C. Arias, J. D. MacKenzie, R. Stevenson, J. J. M. Halls, M. Inbasekaran, E. P. Woo, D. Richards, and R. H. Friend, “Photovoltaic Performance and Morphology of Polyfluorene Blends: A Combined Microscopic and Photovoltaic Investigation,” *Macromolecules*, vol. 34, no. 17, pp. 6005–6013, Aug. 2001.
- [111] C. M. Proctor, M. Kuik, and T.-Q. Nguyen, “Charge carrier recombination in organic solar cells,” *Progress in Polymer Science*, vol. 38, no. 12, pp. 1941–1960, Dec. 2013.
- [112] J. R. Tumbleston, D.-H. Ko, E. T. Samulski, and R. Lopez, “Nonideal parasitic resistance effects in bulk heterojunction organic solar cells,” *Journal of Applied Physics*, vol. 108, no. 8, p. 084514, Oct. 2010.
- [113] M. A. Green, “Solar cell fill factors: General graph and empirical expressions,” *Solid-State Electronics*, vol. 24, no. 8, pp. 788–789, Aug. 1981.
- [114] J. D. Servaites, S. Yeganeh, T. J. Marks, and M. A. Ratner, “Efficiency Enhancement in Organic Photovoltaic Cells: Consequences of Optimizing Series Resistance,” *Advanced Functional Materials*, vol. 20, no. 1, pp. 97–104, Jan. 2010.
- [115] M.-S. Kim, B.-G. Kim, and J. Kim, “Effective Variables To Control the Fill Factor of Organic Photovoltaic Cells,” *ACS Applied Materials & Interfaces*, vol. 1, no. 6, pp. 1264–1269, Jun. 2009.
- [116] L. J. A. Koster, V. D. Mihailetchi, H. Xie, and P. W. M. Blom, “Origin of the light intensity dependence of the short-circuit current of polymer/fullerene solar cells,” *Applied Physics Letters*, vol. 87, no. 20, p. 203502, Nov. 2005.
- [117] J. Xue, S. Uchida, B. P. Rand, and S. R. Forrest, “4.2% efficient organic photovoltaic cells with low series resistances,” *Applied Physics Letters*, vol. 84, no. 16, pp. 3013–3015, Apr. 2004.
- [118] A. K. Pandey, J. M. Nunzi, B. Ratier, and A. Moliton, “Size effect on organic optoelectronics devices: Example of photovoltaic cell efficiency,” *Physics Letters A*, vol. 372, no. 8, pp. 1333–1336, Feb. 2008.
- [119] W.-I. Jeong, J. Lee, S.-Y. Park, J.-W. Kang, and J.-J. Kim, “Reduction of Collection Efficiency of Charge Carriers with Increasing Cell Size in Polymer Bulk Heterojunction Solar Cells,” *Advanced Functional Materials*, vol. 21, no. 2, pp. 343–347, Jan. 2011.
- [120] L. Lucera, P. Kubis, F. W. Fecher, C. Bronnbauer, M. Turbiez, K. Forberich, T. Ameri, H.-J. Egelhaaf, and C. J. Brabec, “Guidelines for Closing the Efficiency Gap between Hero Solar Cells and Roll-To-Roll Printed Modules,” *Energy Technology*, vol. 3, no. 4, pp. 373–384, Apr. 2015.
- [121] T. Miyadera, H. Ogo, T. Taima, T. Yamanari, and Y. Yoshida, “Analytical model for the design principle of large-area solar cells,” *Solar Energy Materials and Solar Cells*, vol. 97, pp. 127–131, Feb. 2012.
- [122] H. Hoppe, M. Seeland, and B. Muhsin, “Optimal geometric design of monolithic thin-film solar modules: Architecture of polymer solar cells,” *Solar Energy Materials and Solar Cells*, vol. 97, pp. 119–126, Feb. 2012.

## References

---

- [123] W. Qin, X. Xu, D. Liu, C. Ma, L. Yang, S. Yin, F. Zhang, and J. Wei, "Surface states of ZnO nanoparticles effect on the performance of inverted-organic solar cells," *Journal of Renewable and Sustainable Energy*, vol. 5, no. 5, p. 053106, Sep. 2013.
- [124] C. Waldauf, M. C. Scharber, P. Schilinsky, J. A. Hauch, and C. J. Brabec, "Physics of organic bulk heterojunction devices for photovoltaic applications," *Journal of Applied Physics*, vol. 99, no. 10, p. 104503, May 2006.
- [125] M.-H. Jao, H.-C. Liao, and W.-F. Su, "Achieving a high fill factor for organic solar cells," *Journal of Materials Chemistry A*, vol. 4, no. 16, pp. 5784–5801, 2016.
- [126] A. Wagenpfahl, D. Rauh, M. Binder, C. Deibel, and V. Dyakonov, "S-shaped current-voltage characteristics of organic solar devices," *Physical Review B*, vol. 82, no. 11, p. 115306, Sep. 2010.
- [127] W. Tress, A. Petrich, M. Hummert, M. Hein, K. Leo, and M. Riede, "Imbalanced mobilities causing S-shaped IV curves in planar heterojunction organic solar cells," *Applied Physics Letters*, vol. 98, no. 6, p. 063301, Feb. 2011.
- [128] M. Zhang, H. Wang, and C. W. Tang, "Hole-transport limited S-shaped I-V curves in planar heterojunction organic photovoltaic cells," *Applied Physics Letters*, vol. 99, no. 21, p. 213506, Nov. 2011.
- [129] Y.-J. Cheng, S.-H. Yang, and C.-S. Hsu, "Synthesis of Conjugated Polymers for Organic Solar Cell Applications," *Chemical Reviews*, vol. 109, no. 11, pp. 5868–5923, Nov. 2009.
- [130] P.-L. T. Boudreault, A. Najari, and M. Leclerc, "Processable Low-Bandgap Polymers for Photovoltaic Applications †," *Chemistry of Materials*, vol. 23, no. 3, pp. 456–469, Feb. 2011.
- [131] Y. Li, "Molecular Design of Photovoltaic Materials for Polymer Solar Cells: Toward Suitable Electronic Energy Levels and Broad Absorption," *Accounts of Chemical Research*, vol. 45, no. 5, pp. 723–733, May 2012.
- [132] H. Kang, G. Kim, J. Kim, S. Kwon, H. Kim, and K. Lee, "Bulk-Heterojunction Organic Solar Cells: Five Core Technologies for Their Commercialization," *Advanced Materials*, vol. 28, no. 36, pp. 7821–7861, Sep. 2016.
- [133] H. Zhou, L. Yang, and W. You, "Rational Design of High Performance Conjugated Polymers for Organic Solar Cells," *Macromolecules*, vol. 45, no. 2, pp. 607–632, Jan. 2012.
- [134] N. Blouin, A. Michaud, and M. Leclerc, "A Low-Bandgap Poly(2,7-Carbazole) Derivative for Use in High-Performance Solar Cells," *Advanced Materials*, vol. 19, no. 17, pp. 2295–2300, Sep. 2007.
- [135] C. Zhan, X. Zhang, and J. Yao, "New advances in non-fullerene acceptor based organic solar cells," *RSC Advances*, vol. 5, no. 113, pp. 93002–93026, 2015.
- [136] W. Chen and Q. Zhang, "Recent progress in non-fullerene small molecule acceptors in organic solar cells (OSCs)," *Journal of Materials Chemistry C*, vol. 5, no. 6, pp. 1275–1302, 2017.
- [137] H. W. Kroto, A. W. Allaf, and S. P. Balm, "C60: Buckminsterfullerene," *Chemical Reviews*, vol. 91, no. 6, pp. 1213–1235, Sep. 1991.
- [138] R. F. Curl and R. E. Smalley, "Probing C60," *Science*, vol. 242, no. 4881, pp. 1017–1022, Nov. 1988.
- [139] R. Taylor, J. P. Hare, A. K. Abdul-Sada, and H. W. Kroto, "Isolation, separation and characterisation of the fullerenes C60 and C70: the third form of carbon," *Journal of the Chemical Society, Chemical Communications*, no. 20, p. 1423, 1990.
- [140] M. T. Dang, L. Hirsch, G. Wantz, and J. D. Wuest, "Controlling the Morphology and Performance of Bulk Heterojunctions in Solar Cells. Lessons Learned from the

## References

---

- Benchmark Poly(3-hexylthiophene):[6,6]-Phenyl-C<sub>61</sub>-butyric Acid Methyl Ester System,” *Chemical Reviews*, vol. 113, no. 5, pp. 3734–3765, May 2013.
- [141] A. Kumar, S. Sista, and Y. Yang, “Dipole induced anomalous S-shape I-V curves in polymer solar cells,” *Journal of Applied Physics*, vol. 105, no. 9, p. 094512, May 2009.
- [142] F. Wudl, “The chemical properties of buckminsterfullerene (C<sub>60</sub>) and the birth and infancy of fullerenes,” *Accounts of Chemical Research*, vol. 25, no. 3, pp. 157–161, Mar. 1992.
- [143] J. C. Hummelen, B. W. Knight, F. LePeq, F. Wudl, J. Yao, and C. L. Wilkins, “Preparation and Characterization of Fulleroid and Methanofullerene Derivatives,” *The Journal of Organic Chemistry*, vol. 60, no. 3, pp. 532–538, Feb. 1995.
- [144] X. Liu, H. Chen, and S. Tan, “Overview of high-efficiency organic photovoltaic materials and devices,” *Renewable and Sustainable Energy Reviews*, vol. 52, pp. 1527–1538, Dec. 2015.
- [145] M. M. Wienk, J. M. Kroon, W. J. H. Verhees, J. Knol, J. C. Hummelen, P. A. van Hal, and R. A. J. Janssen, “Efficient Methano[70]fullerene/MDMO-PPV Bulk Heterojunction Photovoltaic Cells,” *Angewandte Chemie International Edition*, vol. 42, no. 29, pp. 3371–3375, Jul. 2003.
- [146] R. Steim, F. R. Kogler, and C. J. Brabec, “Interface materials for organic solar cells,” *Journal of Materials Chemistry*, vol. 20, no. 13, p. 2499, 2010.
- [147] H.-L. Yip and A. K.-Y. Jen, “Recent advances in solution-processed interfacial materials for efficient and stable polymer solar cells,” *Energy & Environmental Science*, vol. 5, no. 3, p. 5994, 2012.
- [148] J. Meyer, S. Hamwi, M. Kröger, W. Kowalsky, T. Riedl, and A. Kahn, “Transition Metal Oxides for Organic Electronics: Energetics, Device Physics and Applications,” *Advanced Materials*, vol. 24, no. 40, pp. 5408–5427, Oct. 2012.
- [149] A. K. K. Kyaw, X. W. Sun, C. Y. Jiang, G. Q. Lo, D. W. Zhao, and D. L. Kwong, “An inverted organic solar cell employing a sol-gel derived ZnO electron selective layer and thermal evaporated MoO<sub>3</sub> hole selective layer,” *Applied Physics Letters*, vol. 93, no. 22, p. 221107, Dec. 2008.
- [150] J. Gilot, I. Barbu, M. M. Wienk, and R. A. J. Janssen, “The use of ZnO as optical spacer in polymer solar cells: Theoretical and experimental study,” *Applied Physics Letters*, vol. 91, no. 11, p. 113520, Sep. 2007.
- [151] M. S. White, D. C. Olson, S. E. Shaheen, N. Kopidakis, and D. S. Ginley, “Inverted bulk-heterojunction organic photovoltaic device using a solution-derived ZnO underlayer,” *Applied Physics Letters*, vol. 89, no. 14, p. 143517, Oct. 2006.
- [152] S. K. Hau, H.-L. Yip, N. S. Baek, J. Zou, K. O’Malley, and A. K.-Y. Jen, “Air-stable inverted flexible polymer solar cells using zinc oxide nanoparticles as an electron selective layer,” *Applied Physics Letters*, vol. 92, no. 25, p. 253301, Jun. 2008.
- [153] J.-H. Huang, T.-Y. Huang, H.-Y. Wei, K.-C. Ho, and C.-W. Chu, “Wet-milled transition metal oxide nanoparticles as buffer layers for bulk heterojunction solar cells,” *RSC Advances*, vol. 2, no. 19, p. 7487, 2012.
- [154] J.-C. Wang, W.-T. Weng, M.-Y. Tsai, M.-K. Lee, S.-F. Horng, T.-P. Perng, C.-C. Kei, C.-C. Yu, and H.-F. Meng, “Highly efficient flexible inverted organic solar cells using atomic layer deposited ZnO as electron selective layer,” *J. Mater. Chem.*, vol. 20, no. 5, pp. 862–866, 2010.
- [155] J. Huang, Z. Yin, and Q. Zheng, “Applications of ZnO in organic and hybrid solar cells,” *Energy & Environmental Science*, vol. 4, no. 10, p. 3861, 2011.
- [156] L. Znaidi, “Sol-gel-deposited ZnO thin films: A review,” *Materials Science and Engineering: B*, vol. 174, no. 1–3, pp. 18–30, Oct. 2010.

## References

---

- [157] T. Kirchartz, J. Mattheis, and U. Rau, "Detailed balance theory of excitonic and bulk heterojunction solar cells," *Physical Review B*, vol. 78, no. 23, p. 235320, Dec. 2008.
- [158] M. N. Kamalasanan and S. Chandra, "Sol-gel synthesis of ZnO thin films," *Thin Solid Films*, vol. 288, no. 1–2, pp. 112–115, Nov. 1996.
- [159] C. E. Small, S. Chen, J. Subbiah, C. M. Amb, S.-W. Tsang, T.-H. Lai, J. R. Reynolds, and F. So, "High-efficiency inverted dithienogermole–thienopyrrolodione-based polymer solar cells," *Nature Photonics*, vol. 6, no. 2, pp. 115–120, Feb. 2012.
- [160] P. de Bruyn, D. J. D. Moet, and P. W. M. Blom, "A facile route to inverted polymer solar cells using a precursor based zinc oxide electron transport layer," *Organic Electronics*, vol. 11, no. 8, pp. 1419–1422, Aug. 2010.
- [161] M. Lu, P. de Bruyn, H. T. Nicolai, G.-J. A. H. Wetzelaer, and P. W. M. Blom, "Hole-enhanced electron injection from ZnO in inverted polymer light-emitting diodes," *Organic Electronics*, vol. 13, no. 9, pp. 1693–1699, Sep. 2012.
- [162] K. Lee, J. Y. Kim, S. H. Park, S. H. Kim, S. Cho, and A. J. Heeger, "Air-Stable Polymer Electronic Devices," *Advanced Materials*, vol. 19, no. 18, pp. 2445–2449, Sep. 2007.
- [163] R. Steim, S. A. Choulis, P. Schilinsky, and C. J. Brabec, "Interface modification for highly efficient organic photovoltaics," *Applied Physics Letters*, vol. 92, no. 9, p. 093303, Mar. 2008.
- [164] K. Shankar, J. Bandara, M. Paulose, H. Wietasch, O. K. Varghese, G. K. Mor, T. J. LaTempa, M. Thelakkat, and C. A. Grimes, "Highly Efficient Solar Cells using TiO<sub>2</sub> Nanotube Arrays Sensitized with a Donor-Antenna Dye," *Nano Letters*, vol. 8, no. 6, pp. 1654–1659, Jun. 2008.
- [165] C.-Y. Li, T.-C. Wen, T.-H. Lee, T.-F. Guo, J.-C.-A. Huang, Y.-C. Lin, and Y.-J. Hsu, "An inverted polymer photovoltaic cell with increased air stability obtained by employing novel hole/electron collecting layers," *Journal of Materials Chemistry*, vol. 19, no. 11, p. 1643, 2009.
- [166] J. Y. Kim, S. H. Kim, H.-H. Lee, K. Lee, W. Ma, X. Gong, and A. J. Heeger, "New Architecture for High-Efficiency Polymer Photovoltaic Cells Using Solution-Based Titanium Oxide as an Optical Spacer," *Advanced Materials*, vol. 18, no. 5, pp. 572–576, Mar. 2006.
- [167] G. Wang, W. Xing, and S. Zhuo, "Application of mesoporous carbon to counter electrode for dye-sensitized solar cells," *Journal of Power Sources*, vol. 194, no. 1, pp. 568–573, Oct. 2009.
- [168] A. Hayakawa, O. Yoshikawa, T. Fujieda, K. Uehara, and S. Yoshikawa, "High performance polythiophene/fullerene bulk-heterojunction solar cell with a TiO<sub>x</sub> hole blocking layer," *Applied Physics Letters*, vol. 90, no. 16, p. 163517, Apr. 2007.
- [169] H. Schmidt, K. Zilberberg, S. Schmale, H. Flügge, T. Riedl, and W. Kowalsky, "Transient characteristics of inverted polymer solar cells using titaniumoxide interlayers," *Applied Physics Letters*, vol. 96, no. 24, p. 243305, Jun. 2010.
- [170] Y.-S. He, J. C. Campbell, R. C. Murphy, M. F. Arendt, and J. S. Swinnea, "Electrical and optical characterization of Sb : SnO<sub>2</sub>," *Journal of Materials Research*, vol. 8, no. 12, pp. 3131–3134, Dec. 1993.
- [171] C. Terrier, J. P. Chatelon, and J. A. Roger, "Electrical and optical properties of Sb:SnO<sub>2</sub> thin films obtained by the sol-gel method," *Thin Solid Films*, vol. 295, no. 1–2, pp. 95–100, Feb. 1997.
- [172] S.-Y. Park, Y.-J. Kang, S. Lee, D.-G. Kim, J.-K. Kim, J. H. Kim, and J.-W. Kang, "Spray-coated organic solar cells with large-area of 12.25cm<sup>2</sup>," *Solar Energy Materials and Solar Cells*, vol. 95, no. 3, pp. 852–855, Mar. 2011.
- [173] M. BATZILL and U. DIEBOLD, "The surface and materials science of tin oxide," *Progress in Surface Science*, vol. 79, no. 2–4, pp. 47–154, 2005.

## References

---

- [174] K. Hamada, N. Murakami, T. Tsubota, and T. Ohno, "Solution-processed amorphous niobium oxide as a novel electron collection layer for inverted polymer solar cells," *Chemical Physics Letters*, vol. 586, pp. 81–84, Oct. 2013.
- [175] K. Galatsis, Y. X. Li, W. Wlodarski, E. Comini, G. Sberveglieri, C. Cantalini, S. Santucci, and M. Passacantando, "Comparison of single and binary oxide MoO<sub>3</sub>, TiO<sub>2</sub> and WO<sub>3</sub> sol-gel gas sensors," *Sensors and Actuators B: Chemical*, vol. 83, no. 1–3, pp. 276–280, Mar. 2002.
- [176] C. Giroto, E. Voroshazi, D. Cheyns, P. Heremans, and B. P. Rand, "Solution-Processed MoO<sub>3</sub> Thin Films As a Hole-Injection Layer for Organic Solar Cells," *ACS Applied Materials & Interfaces*, vol. 3, no. 9, pp. 3244–3247, Sep. 2011.
- [177] L. Boudaoud, N. Benramdane, R. Desfeux, B. Khelifa, and C. Mathieu, "Structural and optical properties of MoO<sub>3</sub> and V<sub>2</sub>O<sub>5</sub> thin films prepared by Spray Pyrolysis," *Catalysis Today*, vol. 113, no. 3–4, pp. 230–234, Apr. 2006.
- [178] S. Murase and Y. Yang, "Solution Processed MoO<sub>3</sub> Interfacial Layer for Organic Photovoltaics Prepared by a Facile Synthesis Method," *Advanced Materials*, vol. 24, no. 18, pp. 2459–2462, May 2012.
- [179] S. R. Hammond, J. Meyer, N. E. Widjonarko, P. F. Ndione, A. K. Sigdel, A. Garcia, A. Miedaner, M. T. Lloyd, A. Kahn, D. S. Ginley, J. J. Berry, and D. C. Olson, "Low-temperature, solution-processed molybdenum oxide hole-collection layer for organic photovoltaics," *Journal of Materials Chemistry*, vol. 22, no. 7, p. 3249, 2012.
- [180] J. Meyer, R. Khalandovsky, P. Görrn, and A. Kahn, "MoO<sub>3</sub> Films Spin-Coated from a Nanoparticle Suspension for Efficient Hole-Injection in Organic Electronics," *Advanced Materials*, vol. 23, no. 1, pp. 70–73, Jan. 2011.
- [181] X. Li, W. C. H. Choy, F. Xie, S. Zhang, and J. Hou, "Room-temperature solution-processed molybdenum oxide as a hole transport layer with Ag nanoparticles for highly efficient inverted organic solar cells," *Journal of Materials Chemistry A*, vol. 1, no. 22, p. 6614, 2013.
- [182] K. Zilberberg, H. Gharbi, A. Behrendt, S. Trost, and T. Riedl, "Low-Temperature, Solution-Processed MoO<sub>x</sub> for Efficient and Stable Organic Solar Cells," *ACS Applied Materials & Interfaces*, vol. 4, no. 3, pp. 1164–1168, Mar. 2012.
- [183] M. Benmouss, A. Outzourhit, R. Jourdani, A. Bennouna, and E. L. Ameziane, "STRUCTURAL, OPTICAL AND ELECTROCHROMIC PROPERTIES OF SOL-GEL V<sub>2</sub>O<sub>5</sub> THIN FILMS Films," *Active and Passive Electronic Components*, vol. 26, no. 4, pp. 245–256, 2003.
- [184] Z. Tan, W. Zhang, C. Cui, Y. Ding, D. Qian, Q. Xu, L. Li, S. Li, and Y. Li, "Solution-processed vanadium oxide as a hole collection layer on an ITO electrode for high-performance polymer solar cells," *Physical Chemistry Chemical Physics*, vol. 14, no. 42, p. 14589, 2012.
- [185] K. Zilberberg, S. Trost, H. Schmidt, and T. Riedl, "Solution Processed Vanadium Pentoxide as Charge Extraction Layer for Organic Solar Cells," *Advanced Energy Materials*, vol. 1, no. 3, pp. 377–381, May 2011.
- [186] T. T. Larsen-Olsen, E. Bundgaard, K. O. Sylvester-Hvid, and F. C. Krebs, "A solution process for inverted tandem solar cells," *Organic Electronics*, vol. 12, no. 2, pp. 364–371, Feb. 2011.
- [187] J. W. Shim, C. Fuentes-Hernandez, A. Dindar, Y. Zhou, T. M. Khan, and B. Kippelen, "Polymer solar cells with NiO hole-collecting interlayers processed by atomic layer deposition," *Organic Electronics*, vol. 14, no. 11, pp. 2802–2808, Nov. 2013.
- [188] M. D. Irwin, D. B. Buchholz, A. W. Hains, R. P. H. Chang, and T. J. Marks, "p-Type semiconducting nickel oxide as an efficiency-enhancing anode interfacial layer in

## References

---

- polymer bulk-heterojunction solar cells,” *Proceedings of the National Academy of Sciences*, vol. 105, no. 8, pp. 2783–2787, Feb. 2008.
- [189] H. Choi, B. Kim, M. J. Ko, D.-K. Lee, H. Kim, S. H. Kim, and K. Kim, “Solution processed WO<sub>3</sub> layer for the replacement of PEDOT:PSS layer in organic photovoltaic cells,” *Organic Electronics*, vol. 13, no. 6, pp. 959–968, Jun. 2012.
- [190] K. Walzer, B. Maennig, M. Pfeiffer, and K. Leo, “Highly Efficient Organic Devices Based on Electrically Doped Transport Layers,” *Chemical Reviews*, vol. 107, no. 4, pp. 1233–1271, Apr. 2007.
- [191] Y.-Y. Lai, Y.-J. Cheng, and C.-S. Hsu, “Applications of functional fullerene materials in polymer solar cells,” *Energy & Environmental Science*, vol. 7, no. 6, p. 1866, 2014.
- [192] J. Huang, M. Pfeiffer, A. Werner, J. Blochwitz, K. Leo, and S. Liu, “Low-voltage organic electroluminescent devices using pin structures,” *Applied Physics Letters*, vol. 80, no. 1, pp. 139–141, Jan. 2002.
- [193] C. Badre, L. Marquant, A. M. Alsayed, and L. A. Hough, “Highly Conductive Poly(3,4-ethylenedioxythiophene):Poly (styrenesulfonate) Films Using 1-Ethyl-3-methylimidazolium Tetracyanoborate Ionic Liquid,” *Advanced Functional Materials*, vol. 22, no. 13, pp. 2723–2727, Jul. 2012.
- [194] D. Alemu, H.-Y. Wei, K.-C. Ho, and C.-W. Chu, “Highly conductive PEDOT:PSS electrode by simple film treatment with methanol for ITO-free polymer solar cells,” *Energy & Environmental Science*, vol. 5, no. 11, p. 9662, 2012.
- [195] Y. H. Kim, C. Sachse, M. L. Machala, C. May, L. Müller-Meskamp, and K. Leo, “Highly Conductive PEDOT:PSS Electrode with Optimized Solvent and Thermal Post-Treatment for ITO-Free Organic Solar Cells,” *Advanced Functional Materials*, vol. 21, no. 6, pp. 1076–1081, Mar. 2011.
- [196] F. Huang, H. Wu, and Y. Cao, “Water/alcohol soluble conjugated polymers as highly efficient electron transporting/injection layer in optoelectronic devices,” *Chemical Society Reviews*, vol. 39, no. 7, p. 2500, 2010.
- [197] C. Duan, K. Zhang, C. Zhong, F. Huang, and Y. Cao, “Recent advances in water/alcohol-soluble  $\pi$ -conjugated materials: new materials and growing applications in solar cells,” *Chemical Society Reviews*, vol. 42, no. 23, p. 9071, 2013.
- [198] Z. He, H. Wu, and Y. Cao, “Recent Advances in Polymer Solar Cells: Realization of High Device Performance by Incorporating Water/Alcohol-Soluble Conjugated Polymers as Electrode Buffer Layer,” *Advanced Materials*, vol. 26, no. 7, pp. 1006–1024, Feb. 2014.
- [199] W. Zhang, B. Zhao, Z. He, X. Zhao, H. Wang, S. Yang, H. Wu, and Y. Cao, “High-efficiency ITO-free polymer solar cells using highly conductive PEDOT:PSS/surfactant bilayer transparent anodes,” *Energy & Environmental Science*, vol. 6, no. 6, p. 1956, 2013.
- [200] Z. He, C. Zhong, S. Su, M. Xu, H. Wu, and Y. Cao, “Enhanced power-conversion efficiency in polymer solar cells using an inverted device structure,” *Nature Photonics*, vol. 6, no. 9, pp. 591–595, Sep. 2012.
- [201] S.-H. Liao, Y.-L. Li, T.-H. Jen, Y.-S. Cheng, and S.-A. Chen, “Multiple Functionalities of Polyfluorene Grafted with Metal Ion-Intercalated Crown Ether as an Electron Transport Layer for Bulk-Heterojunction Polymer Solar Cells: Optical Interference, Hole Blocking, Interfacial Dipole, and Electron Conduction,” *Journal of the American Chemical Society*, vol. 134, no. 35, pp. 14271–14274, Sep. 2012.
- [202] S.-H. L. Hsin-Hung Lu Yun-Chung Wu Yun-Sheng Ma Show-An Chen, “Composite material of hole-blocking polymer and electron-injection/electron-transport conjugated polymer grafted with crown ether into which metal ion is intercalated, and uses thereof in OLED and organic solar cell.” .

## References

---

- [203] Y. Zhou, C. Fuentes-Hernandez, J. Shim, J. Meyer, A. J. Giordano, H. Li, P. Winget, T. Papadopoulos, H. Cheun, J. Kim, M. Fenoll, A. Dindar, W. Haske, E. Najafabadi, T. M. Khan, H. Sojoudi, S. Barlow, S. Graham, J.-L. Bredas, S. R. Marder, A. Kahn, and B. Kippelen, "A Universal Method to Produce Low-Work Function Electrodes for Organic Electronics," *Science*, vol. 336, no. 6079, pp. 327–332, Apr. 2012.
- [204] H. Kang, S. Hong, J. Lee, and K. Lee, "Electrostatically Self-Assembled Nonconjugated Polyelectrolytes as an Ideal Interfacial Layer for Inverted Polymer Solar Cells," *Advanced Materials*, vol. 24, no. 22, pp. 3005–3009, Jun. 2012.
- [205] K. Sun, B. Zhao, V. Murugesan, A. Kumar, K. Zeng, J. Subbiah, W. W. H. Wong, D. J. Jones, and J. Ouyang, "High-performance polymer solar cells with a conjugated zwitterion by solution processing or thermal deposition as the electron-collection interlayer," *Journal of Materials Chemistry*, vol. 22, no. 45, p. 24155, 2012.
- [206] S. Khodabakhsh, B. M. Sanderson, J. Nelson, and T. S. Jones, "Using Self-Assembling Dipole Molecules to Improve Charge Collection in Molecular Solar Cells," *Advanced Functional Materials*, vol. 16, no. 1, pp. 95–100, Jan. 2006.
- [207] J. S. Kim, J. H. Park, J. H. Lee, J. Jo, D.-Y. Kim, and K. Cho, "Control of the electrode work function and active layer morphology via surface modification of indium tin oxide for high efficiency organic photovoltaics," *Applied Physics Letters*, vol. 91, no. 11, p. 112111, Sep. 2007.
- [208] H. Choi, H.-B. Kim, S.-J. Ko, J. Y. Kim, and A. J. Heeger, "An Organic Surface Modifier to Produce a High Work Function Transparent Electrode for High Performance Polymer Solar Cells," *Advanced Materials*, vol. 27, no. 5, pp. 892–896, Feb. 2015.
- [209] X. Ouyang, R. Peng, L. Ai, X. Zhang, and Z. Ge, "Efficient polymer solar cells employing a non-conjugated small-molecule electrolyte," *Nature Photonics*, vol. 9, no. 8, pp. 520–524, Aug. 2015.
- [210] J. Liu, S. Shao, B. Meng, G. Fang, Z. Xie, L. Wang, and X. Li, "Enhancement of inverted polymer solar cells with solution-processed ZnO-TiO<sub>2</sub> X composite as cathode buffer layer," *Applied Physics Letters*, vol. 100, no. 21, p. 213906, May 2012.
- [211] A. Savva and S. A. Choulis, "Cesium-doped zinc oxide as electron selective contact in inverted organic photovoltaics," *Applied Physics Letters*, vol. 102, no. 23, p. 233301, Jun. 2013.
- [212] M. J. Beliatis, K. K. Gandhi, L. J. Rozanski, R. Rhodes, L. McCafferty, M. R. Alenezi, A. S. Alshammari, C. A. Mills, K. D. G. I. Jayawardena, S. J. Henley, and S. R. P. Silva, "Hybrid Graphene-Metal Oxide Solution Processed Electron Transport Layers for Large Area High-Performance Organic Photovoltaics," *Advanced Materials*, vol. 26, no. 13, pp. 2078–2083, Apr. 2014.
- [213] H. Woo Lee, J. Young Oh, T. Il Lee, W. Soon Jang, Y. Bum Yoo, S. Sang Chae, J. Ho Park, J. Min Myoung, K. Moon Song, and H. Koo Baik, "Highly efficient inverted polymer solar cells with reduced graphene-oxide-zinc-oxide nanocomposites buffer layer," *Applied Physics Letters*, vol. 102, no. 19, p. 193903, May 2013.
- [214] P. Xu, L. Shen, F. Meng, J. Zhang, W. Xie, W. Yu, W. Guo, X. Jia, and S. Ruan, "The role of Ag nanoparticles in inverted polymer solar cells: Surface plasmon resonance and backscattering centers," *Applied Physics Letters*, vol. 102, no. 12, p. 123301, Mar. 2013.
- [215] E.-K. Park, M. Choi, J.-H. Jeun, K.-T. Lim, J.-M. Kim, and Y.-S. Kim, "The effect of metal oxide nanoparticle concentrations in PEDOT:PSS layer on the performance of P3HT:PCBM organic solar cells," *Microelectronic Engineering*, vol. 111, pp. 166–169, Nov. 2013.

## References

---

- [216] S.-W. Baek, J. Noh, C.-H. Lee, B. Kim, M.-K. Seo, and J.-Y. Lee, “Plasmonic Forward Scattering Effect in Organic Solar Cells: A Powerful Optical Engineering Method,” *Scientific Reports*, vol. 3, no. 1, p. 1726, Dec. 2013.
- [217] N. Kalfagiannis, P. G. Karagiannidis, C. Pitsalidis, N. T. Panagiotopoulos, C. Gravalidis, S. Kassavetis, P. Patsalas, and S. Logothetidis, “Plasmonic silver nanoparticles for improved organic solar cells,” *Solar Energy Materials and Solar Cells*, vol. 104, pp. 165–174, Sep. 2012.
- [218] D. D. S. Fung, L. Qiao, W. C. H. Choy, C. Wang, W. E. I. Sha, F. Xie, and S. He, “Optical and electrical properties of efficiency enhanced polymer solar cells with Au nanoparticles in a PEDOT–PSS layer,” *Journal of Materials Chemistry*, vol. 21, no. 41, p. 16349, 2011.
- [219] M. H. Kumar, N. Yantara, S. Dharani, M. Graetzel, S. Mhaisalkar, P. P. Boix, and N. Mathews, “Flexible, low-temperature, solution processed ZnO-based perovskite solid state solar cells,” *Chemical Communications*, vol. 49, no. 94, p. 11089, 2013.
- [220] L. Lu, Z. Luo, T. Xu, and L. Yu, “Cooperative Plasmonic Effect of Ag and Au Nanoparticles on Enhancing Performance of Polymer Solar Cells,” *Nano Letters*, vol. 13, no. 1, pp. 59–64, Jan. 2013.
- [221] M. W. Rowell and M. D. McGehee, “Transparent electrode requirements for thin film solar cell modules,” *Energy Environ. Sci.*, vol. 4, no. 1, pp. 131–134, 2011.
- [222] X. Liu, A. Ng, Y. H. Ng, A. B. Djurišić, A. M. C. Ng, and W. K. Chan, “Effect of electrical properties, transmittance, and morphology of ITO electrode on polymer solar cells characteristics,” 2013, p. 86261W.
- [223] M. W. Rowell, M. A. Topinka, M. D. McGehee, H.-J. Prall, G. Dennler, N. S. Sariciftci, L. Hu, and G. Gruner, “Organic solar cells with carbon nanotube network electrodes,” *Applied Physics Letters*, vol. 88, no. 23, p. 233506, Jun. 2006.
- [224] Y.-C. Huang, F.-H. Hsu, H.-C. Cha, C.-M. Chuang, C.-S. Tsao, and C.-Y. Chen, “High-performance ITO-free spray-processed polymer solar cells with incorporating ink-jet printed grid,” *Organic Electronics*, vol. 14, no. 11, pp. 2809–2817, Nov. 2013.
- [225] M. Neophytou, F. Hermerschmidt, A. Savva, E. Georgiou, and S. A. Choulis, “Highly efficient indium tin oxide-free organic photovoltaics using inkjet-printed silver nanoparticle current collecting grids,” *Applied Physics Letters*, vol. 101, no. 19, p. 193302, Nov. 2012.
- [226] U. N. Maiti, W. J. Lee, J. M. Lee, Y. Oh, J. Y. Kim, J. E. Kim, J. Shim, T. H. Han, and S. O. Kim, “25th Anniversary Article: Chemically Modified/Doped Carbon Nanotubes & Graphene for Optimized Nanostructures & Nanodevices,” *Advanced Materials*, vol. 26, no. 1, pp. 40–67, Jan. 2014.
- [227] B. Ratier, J.-M. Nunzi, M. Aldissi, T. M. Kraft, and E. Buncel, “Organic solar cell materials and active layer designs-improvements with carbon nanotubes: a review,” *Polymer International*, vol. 61, no. 3, pp. 342–354, Mar. 2012.
- [228] K. Rana, J. Singh, and J.-H. Ahn, “A graphene-based transparent electrode for use in flexible optoelectronic devices,” *J. Mater. Chem. C*, vol. 2, no. 15, pp. 2646–2656, 2014.
- [229] E. Singh and H. S. Nalwa, “Graphene-Based Bulk-Heterojunction Solar Cells: A Review,” *Journal of nanoscience and nanotechnology*, vol. 15, no. 9, pp. 6237–78, Sep. 2015.
- [230] Z. Liu, S. P. Lau, and F. Yan, “Functionalized graphene and other two-dimensional materials for photovoltaic devices: device design and processing,” *Chemical Society Reviews*, vol. 44, no. 15, pp. 5638–5679, 2015.
- [231] T. R. Andersen, H. F. Dam, M. Hösel, M. Helgesen, J. E. Carlé, T. T. Larsen-Olsen, S. A. Gevorgyan, J. W. Andreasen, J. Adams, N. Li, F. Machui, G. D. Spyropoulos, T.

- Ameri, N. Lemaître, M. Legros, A. Scheel, D. Gaiser, K. Kreul, S. Berny, O. R. Lozman, S. Nordman, M. Välimäki, M. Vilkmann, R. R. Søndergaard, M. Jørgensen, C. J. Brabec, and F. C. Krebs, "Scalable, ambient atmosphere roll-to-roll manufacture of encapsulated large area, flexible organic tandem solar cell modules," *Energy & Environmental Science*, vol. 7, no. 9, p. 2925, Jun. 2014.
- [232] M. Janani, P. Srikrishnarka, S. V. Nair, and A. S. Nair, "An in-depth review on the role of carbon nanostructures in dye-sensitized solar cells," *Journal of Materials Chemistry A*, vol. 3, no. 35, pp. 17914–17938, 2015.
- [233] H. Wang and Y. H. Hu, "Graphene as a counter electrode material for dye-sensitized solar cells," *Energy & Environmental Science*, vol. 5, no. 8, p. 8182, 2012.
- [234] C. Zhu, H. Min, F. Xu, J. Chen, H. Dong, L. Tong, Y. Zhu, and L. Sun, "Ultrafast electrochemical preparation of graphene/CoS nanosheet counter electrodes for efficient dye-sensitized solar cells," *RSC Advances*, vol. 5, no. 104, pp. 85822–85830, 2015.
- [235] J. Huo, J. Wu, M. Zheng, Y. Tu, and Z. Lan, "A transparent cobalt sulfide/reduced graphene oxide nanostructure counter electrode for high efficient dye-sensitized solar cells," *Electrochimica Acta*, vol. 187, pp. 210–217, Jan. 2016.
- [236] M. Jørgensen, K. Norrman, and F. C. Krebs, "Stability/degradation of polymer solar cells," *Solar Energy Materials and Solar Cells*, vol. 92, no. 7, pp. 686–714, Jul. 2008.
- [237] M. Wu and T. Ma, "Platinum-free catalysts as counter electrodes in dye-sensitized solar cells," *ChemSusChem*, vol. 5, no. 8, pp. 1343–57, Aug. 2012.
- [238] P. Joshi, L. Zhang, Q. Chen, D. Galipeau, H. Fong, and Q. Qiao, "Electrospun Carbon Nanofibers as Low-Cost Counter Electrode for Dye-Sensitized Solar Cells," *ACS Applied Materials & Interfaces*, vol. 2, no. 12, pp. 3572–3577, Dec. 2010.
- [239] K. S. Lee, W. J. Lee, N.-G. Park, S. O. Kim, and J. H. Park, "Transferred vertically aligned N-doped carbon nanotube arrays: use in dye-sensitized solar cells as counter electrodes," *Chemical Communications*, vol. 47, no. 14, p. 4264, 2011.
- [240] T. N. Murakami, S. Ito, Q. Wang, M. K. Nazeeruddin, T. Bessho, I. Cesar, P. Liska, R. Humphry-Baker, P. Comte, P. Péchy, and M. Grätzel, "Highly Efficient Dye-Sensitized Solar Cells Based on Carbon Black Counter Electrodes," *Journal of The Electrochemical Society*, vol. 153, no. 12, p. A2255, 2006.
- [241] M. Wu, X. Lin, T. Wang, J. Qiu, and T. Ma, "Low-cost dye-sensitized solar cell based on nine kinds of carbon counter electrodes," *Energy & Environmental Science*, vol. 4, no. 6, p. 2308, 2011.
- [242] A. Kay and M. Grätzel, "Low cost photovoltaic modules based on dye sensitized nanocrystalline titanium dioxide and carbon powder," *Solar Energy Materials and Solar Cells*, vol. 44, no. 1, pp. 99–117, Oct. 1996.
- [243] E. Ramasamy, W. J. Lee, D. Y. Lee, and J. S. Song, "Spray coated multi-wall carbon nanotube counter electrode for tri-iodide (I<sub>3</sub><sup>-</sup>) reduction in dye-sensitized solar cells," *Electrochemistry Communications*, vol. 10, no. 7, pp. 1087–1089, Jul. 2008.
- [244] J. G. Nam, Y. J. Park, B. S. Kim, and J. S. Lee, "Enhancement of the efficiency of dye-sensitized solar cell by utilizing carbon nanotube counter electrode," *Scripta Materialia*, vol. 62, no. 3, pp. 148–150, Feb. 2010.
- [245] P. V. Kamat, "Graphene-Based Nanoassemblies for Energy Conversion," *The Journal of Physical Chemistry Letters*, vol. 2, no. 3, pp. 242–251, Feb. 2011.
- [246] L. Kavan, J.-H. Yum, M. K. Nazeeruddin, and M. Grätzel, "Graphene Nanoplatelet Cathode for Co(III)/(II) Mediated Dye-Sensitized Solar Cells," *ACS Nano*, vol. 5, no. 11, pp. 9171–9178, Nov. 2011.
- [247] J. D. Roy-Mayhew, D. J. Bozym, C. Punckt, and I. A. Aksay, "Functionalized Graphene as a Catalytic Counter Electrode in Dye-Sensitized Solar Cells," *ACS Nano*, vol. 4, no. 10, pp. 6203–6211, Oct. 2010.

## References

---

- [248] A. Kaniyoor and S. Ramaprabhu, "Soft functionalization of graphene for enhanced tri-iodide reduction in dye sensitized solar cells," *Journal of Materials Chemistry*, vol. 22, no. 17, p. 8377, 2012.
- [249] S. Das, P. Sudhagar, E. Ito, D. Lee, S. Nagarajan, S. Y. Lee, Y. S. Kang, and W. Choi, "Effect of HNO<sub>3</sub> functionalization on large scale graphene for enhanced tri-iodide reduction in dye-sensitized solar cells," *Journal of Materials Chemistry*, vol. 22, no. 38, p. 20490, 2012.
- [250] Q. Luo, F. Hao, S. Wang, H. Shen, L. Zhao, J. Li, M. Grätzel, and H. Lin, "Highly Efficient Metal-Free Sulfur-Doped and Nitrogen and Sulfur Dual-Doped Reduced Graphene Oxide Counter Electrodes for Dye-Sensitized Solar Cells," *The Journal of Physical Chemistry C*, vol. 118, no. 30, pp. 17010–17018, Jul. 2014.
- [251] S. Das, P. Sudhagar, V. Verma, D. Song, E. Ito, S. Y. Lee, Y. S. Kang, and W. Choi, "Amplifying Charge-Transfer Characteristics of Graphene for Triiodide Reduction in Dye-Sensitized Solar Cells," *Advanced Functional Materials*, vol. 21, no. 19, pp. 3729–3736, Oct. 2011.
- [252] L. Song, Q. Luo, F. Zhao, Y. Li, H. Lin, L. Qu, and Z. Zhang, "Dually functional, N-doped porous graphene foams as counter electrodes for dye-sensitized solar cells," *Phys. Chem. Chem. Phys.*, vol. 16, no. 39, pp. 21820–21826, 2014.
- [253] H.-J. Ahn, I.-H. Kim, J.-C. Yoon, S.-I. Kim, and J.-H. Jang, "p-Doped three-dimensional graphene nano-networks superior to platinum as a counter electrode for dye-sensitized solar cells," *Chem. Commun.*, vol. 50, no. 19, pp. 2412–2415, 2014.
- [254] S.-M. Jung, I. T. Choi, K. Lim, J. Ko, J. C. Kim, J.-J. Lee, M. J. Ju, H. K. Kim, and J.-B. Baek, "B-Doped Graphene as an Electrochemically Superior Metal-Free Cathode Material As Compared to Pt over a Co(II)/Co(III) Electrolyte for Dye-Sensitized Solar Cell," *Chemistry of Materials*, vol. 26, no. 11, pp. 3586–3591, Jun. 2014.
- [255] H. Fang, C. Yu, T. Ma, and J. Qiu, "Boron-doped graphene as a high-efficiency counter electrode for dye-sensitized solar cells," *Chemical Communications*, vol. 50, no. 25, p. 3328, 2014.
- [256] P. Zhai, T.-C. Wei, Y.-H. Chang, Y.-T. Huang, W.-T. Yeh, H. Su, and S.-P. Feng, "High Electrocatalytic and Wettable Nitrogen-Doped Microwave-Exfoliated Graphene Nanosheets as Counter Electrode for Dye-Sensitized Solar Cells," *Small*, vol. 10, no. 16, pp. 3347–3353, Aug. 2014.
- [257] A. G. Kannan, J. Zhao, S. G. Jo, Y. S. Kang, and D.-W. Kim, "Nitrogen and sulfur co-doped graphene counter electrodes with synergistically enhanced performance for dye-sensitized solar cells," *J. Mater. Chem. A*, vol. 2, no. 31, pp. 12232–12239, 2014.
- [258] Y. Xue, J. Liu, H. Chen, R. Wang, D. Li, J. Qu, and L. Dai, "Nitrogen-Doped Graphene Foams as Metal-Free Counter Electrodes in High-Performance Dye-Sensitized Solar Cells," *Angewandte Chemie International Edition*, vol. 51, no. 48, pp. 12124–12127, Nov. 2012.
- [259] A. Yella, H.-W. Lee, H. N. Tsao, C. Yi, A. K. Chandiran, M. K. Nazeeruddin, E. W.-G. Diau, C.-Y. Yeh, S. M. Zakeeruddin, and M. Gratzel, "Porphyrin-Sensitized Solar Cells with Cobalt (II/III)-Based Redox Electrolyte Exceed 12 Percent Efficiency," *Science*, vol. 334, no. 6056, pp. 629–634, Nov. 2011.
- [260] W. Kubo, S. Kambe, S. Nakade, T. Kitamura, K. Hanabusa, Y. Wada, and S. Yanagida, "Photocurrent-Determining Processes in Quasi-Solid-State Dye-Sensitized Solar Cells Using Ionic Gel Electrolytes," *The Journal of Physical Chemistry B*, vol. 107, no. 18, pp. 4374–4381, May 2003.
- [261] G. Boschloo and A. Hagfeldt, "Characteristics of the Iodide/Triiodide Redox Mediator in Dye-Sensitized Solar Cells," *Accounts of Chemical Research*, vol. 42, no. 11, pp. 1819–1826, Nov. 2009.

## References

---

- [262] T. W. Hamann, R. A. Jensen, A. B. F. Martinson, H. Van Ryswyk, and J. T. Hupp, "Advancing beyond current generation dye-sensitized solar cells," *Energy & Environmental Science*, vol. 1, no. 1, p. 66, 2008.
- [263] M. Stefik, J.-H. Yum, Y. Hu, and M. Grätzel, "Carbon-graphene nanocomposite cathodes for improved Co(ii/iii) mediated dye-sensitized solar cells," *Journal of Materials Chemistry A*, vol. 1, no. 16, p. 4982, 2013.
- [264] M. J. Ju, J. C. Kim, H.-J. Choi, I. T. Choi, S. G. Kim, K. Lim, J. Ko, J.-J. Lee, I.-Y. Jeon, J.-B. Baek, and H. K. Kim, "N-Doped Graphene Nanoplatelets as Superior Metal-Free Counter Electrodes for Organic Dye-Sensitized Solar Cells," *ACS Nano*, vol. 7, no. 6, pp. 5243–5250, Jun. 2013.
- [265] M. J. Ju, I.-Y. Jeon, J. C. Kim, K. Lim, H.-J. Choi, S.-M. Jung, I. T. Choi, Y. K. Eom, Y. J. Kwon, J. Ko, J.-J. Lee, H. K. Kim, and J.-B. Baek, "Graphene Nanoplatelets Doped with N at its Edges as Metal-Free Cathodes for Organic Dye-Sensitized Solar Cells," *Advanced Materials*, vol. 26, no. 19, pp. 3055–3062, May 2014.
- [266] V.-D. Dao, L. V. Nang, E.-T. Kim, J.-K. Lee, and H.-S. Choi, "Pt Nanoparticles Immobilized on CVD-Grown Graphene as a Transparent Counter Electrode Material for Dye-Sensitized Solar Cells," *ChemSusChem*, vol. 6, no. 8, pp. 1316–1319, Aug. 2013.
- [267] P.-T. Shih, R.-X. Dong, S.-Y. Shen, R. Vittal, J.-J. Lin, and K.-C. Ho, "Transparent graphene-platinum nanohybrid films for counter electrodes in high efficiency dye-sensitized solar cells," *Journal of Materials Chemistry A*, vol. 2, no. 23, p. 8742, 2014.
- [268] Y. Sun, X. Hu, W. Luo, F. Xia, and Y. Huang, "Reconstruction of conformal nanoscale MnO on graphene as a high-capacity and long-life anode material for lithium ion batteries," *Advanced Functional Materials*, vol. 23, no. 19, pp. 2436–2444, 2013.
- [269] B. Li, H. Cao, J. Shao, G. Li, M. Qu, and G. Yin, "Co<sub>3</sub>O<sub>4</sub>@graphene Composites as Anode Materials for High-Performance Lithium Ion Batteries," *Inorganic Chemistry*, vol. 50, no. 5, pp. 1628–1632, 2011.
- [270] Z. Yang, M. Liu, C. Zhang, W. W. Tjiu, T. Liu, and H. Peng, "Carbon Nanotubes Bridged with Graphene Nanoribbons and Their Use in High-Efficiency Dye-Sensitized Solar Cells," *Angewandte Chemie International Edition*, vol. 52, no. 14, pp. 3996–3999, Apr. 2013.
- [271] K. Yu, Z. Wen, H. Pu, G. Lu, Z. Bo, H. Kim, Y. Qian, E. Andrew, S. Mao, and J. Chen, "Hierarchical vertically oriented graphene as a catalytic counter electrode in dye-sensitized solar cells," *J. Mater. Chem. A*, vol. 1, no. 2, pp. 188–193, 2013.
- [272] Y. Xu, H. Bai, G. Lu, C. Li, and G. Shi, "Flexible Graphene Films via the Filtration of Water-Soluble Noncovalent Functionalized Graphene Sheets," *Journal of the American Chemical Society*, vol. 130, no. 18, pp. 5856–5857, May 2008.
- [273] W. Hong, Y. Xu, G. Lu, C. Li, and G. Shi, "Transparent graphene/PEDOT-PSS composite films as counter electrodes of dye-sensitized solar cells," *Electrochemistry Communications*, vol. 10, no. 10, pp. 1555–1558, Oct. 2008.
- [274] J.-Y. Lin, J.-H. Liao, and T.-C. Wei, "Honeycomb-like CoS Counter Electrodes for Transparent Dye-Sensitized Solar Cells," *Electrochemical and Solid-State Letters*, vol. 14, no. 4, p. D41, 2011.
- [275] H. Wang, K. Sun, F. Tao, D. J. Stacchiola, and Y. H. Hu, "3D Honeycomb-Like Structured Graphene and Its High Efficiency as a Counter-Electrode Catalyst for Dye-Sensitized Solar Cells," *Angewandte Chemie International Edition*, vol. 52, no. 35, pp. 9210–9214, Aug. 2013.
- [276] W. Wei, K. Sun, and Y. H. Hu, "Synthesis of 3D cauliflower-fungus-like graphene from CO<sub>2</sub> as a highly efficient counter electrode material for dye-sensitized solar cells," *J. Mater. Chem. A*, vol. 2, no. 40, pp. 16842–16846, Aug. 2014.

## References

---

- [277] Q. Chang, Z. Wang, J. Wang, Y. Yan, Z. Ma, J. Zhu, W. Shi, Q. Chen, Q. Yu, and L. Huang, "Graphene nanosheets inserted by silver nanoparticles as zero-dimensional nanopacers for dye sensitized solar cells," *Nanoscale*, vol. 6, no. 10, pp. 5410–5415, 2014.
- [278] R. Cruz, J. P. Araújo, L. Andrade, and A. Mendes, "Transparent graphene-based counter-electrodes for iodide/triiodide mediated dye-sensitized solar cells," *Journal of Materials Chemistry A*, vol. 2, no. 7, p. 2028, 2014.
- [279] R. Bajpai, S. Roy, N. Kulshrestha, J. Rafiee, N. Koratkar, and D. S. Misra, "Graphene supported nickel nanoparticle as a viable replacement for platinum in dye sensitized solar cells," *Nanoscale*, vol. 4, no. 3, pp. 926–930, 2012.
- [280] C. Y. Neo, N. K. Gopalan, and J. Ouyang, "Graphene oxide/multi-walled carbon nanotube nanocomposites as the gelator of gel electrolytes for quasi-solid state dye-sensitized solar cells," *Journal of Materials Chemistry A*, vol. 2, no. 24, p. 9226, 2014.
- [281] G. Zhu, L. Pan, T. Lu, T. Xu, and Z. Sun, "Electrophoretic deposition of reduced graphene-carbon nanotubes composite films as counter electrodes of dye-sensitized solar cells," *Journal of Materials Chemistry*, vol. 21, no. 38, p. 14869, 2011.
- [282] C. Chen, H. Jian, X. Fu, Z. Ren, M. Yan, G. Qian, and Z. Wang, "Facile synthesis of graphene-supported mesoporous Mn<sub>3</sub>O<sub>4</sub> nanosheets with a high-performance in Li-ion batteries," *RSC Advances*, vol. 4, no. 11, pp. 5367–5370, 2014.
- [283] H. W. Kroto, J. R. Heath, S. C. O'Brien, R. F. Curl, and R. E. Smalley, "C<sub>60</sub>: Buckminsterfullerene," *Nature*, vol. 318, no. 6042, pp. 162–163, Nov. 1985.
- [284] J. H. Davies, *The Physics of Low-Dimensional Semiconductors*. Cambridge: Cambridge University Press, 1997.
- [285] N. Bohr, "I. On the constitution of atoms and molecules," *The London, Edinburgh, and Dublin Philosophical Magazine and Journal of Science*, vol. 26, no. 151, pp. 1–25, Jul. 1913.
- [286] A. Pisanty, "The electronic structure of graphite: A chemist's introduction to band theory," *Journal of Chemical Education*, vol. 68, no. 10, p. 804, Oct. 1991.
- [287] K. K. N. S. M. Sze, *Physics of Semiconductor Devices*, 3rd Editio. John Wiley & Sons, 2006, 2006.
- [288] A. K. Geim and K. S. Novoselov, "The rise of graphene," *Nature Materials*, vol. 6, no. 3, pp. 183–191, Mar. 2007.
- [289] M. Z. Jacobson, M. A. Delucchi, G. Bazouin, Z. A. F. Bauer, C. C. Heavey, E. Fisher, S. B. Morris, D. J. Y. Piekutowski, T. A. Vencill, and T. W. Yeskoo, "Fine structure constant defines visual transparency of graphene.," *Energy Environ. Sci.*, vol. 8, no. 7, pp. 2093–2117, Jun. 2015.
- [290] C. Lee, X. Wei, J. W. Kysar, and J. Hone, "Measurement of the Elastic Properties and Intrinsic Strength of Monolayer Graphene," *Science*, vol. 321, no. 5887, pp. 385–388, Jul. 2008.
- [291] J. Chen, M. Duan, and G. Chen, "Continuous mechanical exfoliation of graphene sheets via three-roll mill," *Journal of Materials Chemistry*, vol. 22, no. 37, p. 19625, 2012.
- [292] A. H. R. Palser, "Interlayer interactions in graphite and carbon nanotubes," *Physical Chemistry Chemical Physics*, vol. 1, no. 18, pp. 4459–4464, 1999.
- [293] E.-Y. Choi, W. S. Choi, Y. B. Lee, and Y.-Y. Noh, "Production of graphene by exfoliation of graphite in a volatile organic solvent," *Nanotechnology*, vol. 22, no. 36, p. 365601, Sep. 2011.
- [294] U. Khan, H. Porwal, A. O'Neill, K. Nawaz, P. May, and J. N. Coleman, "Solvent-Exfoliated Graphene at Extremely High Concentration," *Langmuir*, vol. 27, no. 15, pp. 9077–9082, Aug. 2011.

## References

---

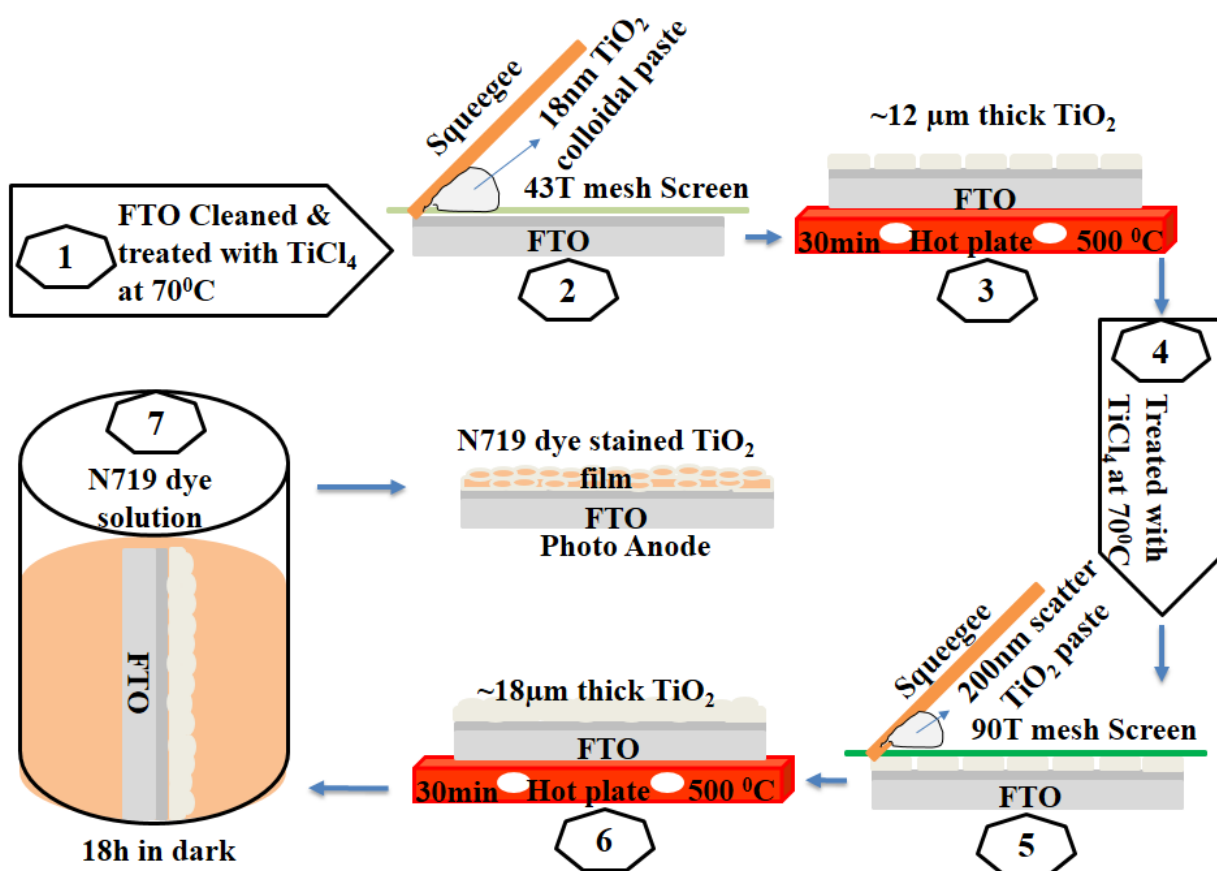
- [295] C. Y. Zhao, D. Zhou, and Z. G. Wu, "Heat Transfer Enhancement of Phase Change Materials (PCMs) in Low and High Temperature Thermal Storage by Using Porous Materials," in *2010 14th International Heat Transfer Conference, Volume 7*, 2010, pp. 435–441.
- [296] N. Behabtu, J. R. Lomeda, M. J. Green, A. L. Higginbotham, A. Sinitskii, D. V. Kosynkin, D. Tsentelovich, A. N. G. Parra-Vasquez, J. Schmidt, E. Kesselman, Y. Cohen, Y. Talmon, J. M. Tour, and M. Pasquali, "Spontaneous high-concentration dispersions and liquid crystals of graphene," *Nature Nanotechnology*, vol. 5, no. 6, pp. 406–411, Jun. 2010.
- [297] M. Lotya, Y. Hernandez, P. J. King, R. J. Smith, V. Nicolosi, L. S. Karlsson, F. M. Blighe, S. De, Z. Wang, I. T. McGovern, G. S. Duesberg, and J. N. Coleman, "Liquid Phase Production of Graphene by Exfoliation of Graphite in Surfactant/Water Solutions," *Journal of the American Chemical Society*, vol. 131, no. 10, pp. 3611–3620, Mar. 2009.
- [298] M. Z. Jacobson, M. A. Delucchi, G. Bazouin, Z. A. F. Bauer, C. C. Heavey, E. Fisher, S. B. Morris, D. J. Y. Piekutowski, T. A. Vencill, and T. W. Yeskoo, "Scalable production of large quantities of defect-free few-layer graphene by shear exfoliation in liquids.," *Energy Environ. Sci.*, vol. 8, no. 7, pp. 2093–2117, Jun. 2015.
- [299] S. Stankovich, D. A. Dikin, R. D. Piner, K. A. Kohlhaas, A. Kleinhammes, Y. Jia, Y. Wu, S. T. Nguyen, and R. S. Ruoff, "Synthesis of graphene-based nanosheets via chemical reduction of exfoliated graphite oxide," *Carbon*, vol. 45, no. 7, pp. 1558–1565, Jun. 2007.
- [300] J. Qu, Y. Yin, Y. Wang, Y. Yan, Y. Guo, and W. Song, "Layer Structured  $\alpha\text{-Fe}_2\text{O}_3$  Nanodisk/Reduced Graphene Oxide Composites as High-Performance Anode Materials for Lithium-Ion Batteries," 2013.
- [301] K. D. G. I. Jayawardena, R. Rhodes, K. K. Gandhi, M. R. R. Prabhath, G. D. M. R. Dabera, M. J. Beliatas, L. J. Rozanski, S. J. Henley, and S. R. P. Silva, "Solution processed reduced graphene oxide/metal oxide hybrid electron transport layers for highly efficient polymer solar cells," *Journal of Materials Chemistry A*, vol. 1, no. 34, p. 9922, 2013.
- [302] C. Nagavolu, K. Susmitha, M. Raghavender, L. Giribabu, K. Bhanu Sankara Rao, C. T. G. Smith, C. A. Mills, S. R. P. Silva, and V. V. S. S. Srikanth, "Pt-free spray coated reduced graphene oxide counter electrodes for dye sensitized solar cells," *Solar Energy*, vol. 137, pp. 143–147, Nov. 2016.
- [303] M. A. Armani, A. Abu-Taleb, N. Remalli, M. Abdullah, V. V. S. S. Srikanth, and N. K. Labhasetwar, "Dragon's blood-aided synthesis of Ag/Ag<sub>2</sub>O core/shell nanostructures and Ag/Ag<sub>2</sub>O decorated multi-layered graphene for efficient As(III) uptake from water and antibacterial activity," *RSC Advances*, vol. 6, no. 50, pp. 44145–44153, 2016.
- [304] R. K. Jammula, S. Pittala, S. Srinath, and V. V. S. S. Srikanth, "Strong interfacial polarization in ZnO decorated reduced-graphene oxide synthesized by molecular level mixing," *Phys. Chem. Chem. Phys.*, vol. 17, no. 26, pp. 17237–17245, 2015.
- [305] S. Petnikota, N. K. Rotte, V. V. S. S. Srikanth, B. S. R. Kota, M. V. Reddy, K. P. Loh, and B. V. R. Chowdari, "Electrochemical studies of few-layered graphene as an anode material for Li ion batteries," *Journal of Solid State Electrochemistry*, vol. 18, no. 4, pp. 941–949, Apr. 2014.
- [306] M. A. Armani, A. Abu-Taleb, N. Remalli, M. Abdullah, V. V. S. S. Srikanth, and N. K. Labhasetwar, "Dragon's blood-aided synthesis of Ag/Ag<sub>2</sub>O core/shell nanostructures and Ag/Ag<sub>2</sub>O decorated multi-layered graphene for efficient As(III) uptake from water and antibacterial activity," *RSC Advances*, vol. 6, no. 50, pp. 44145–44153, 2016.

## References

---

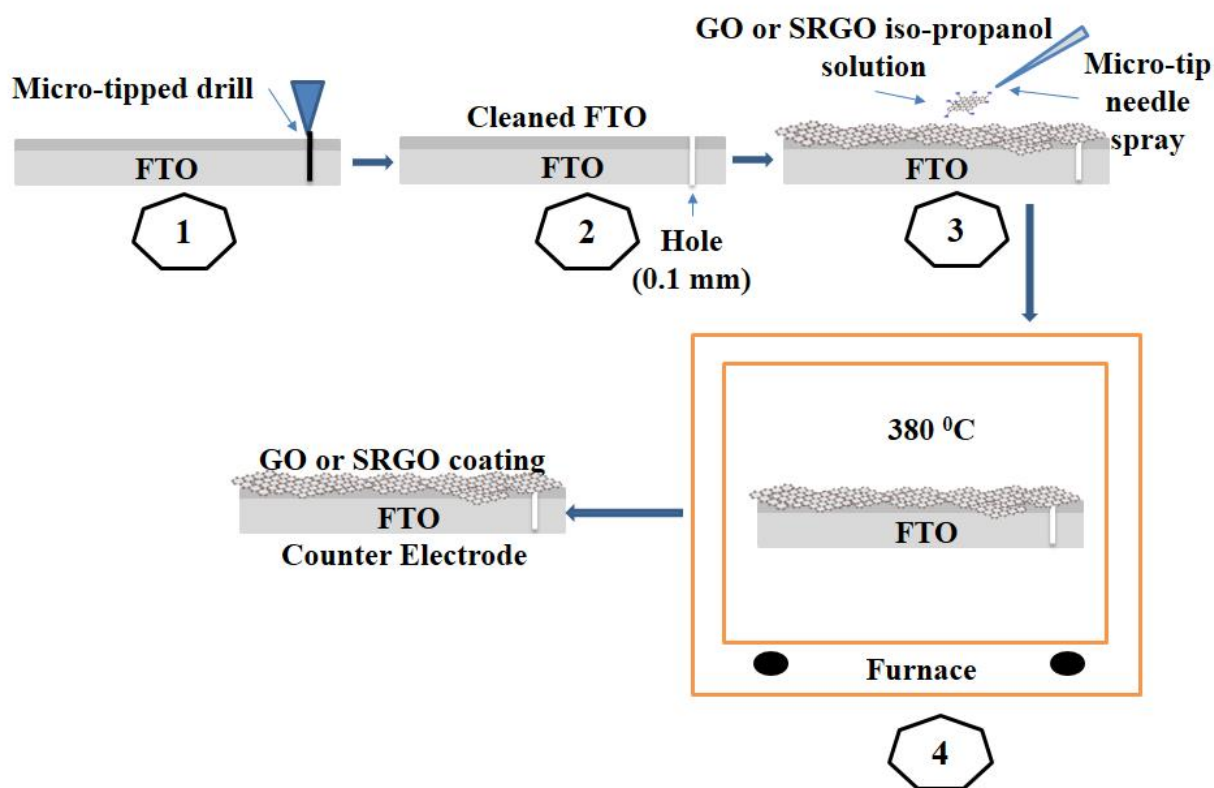
- [307] R. K. Jammula, S. Pittala, S. Srinath, and V. V. S. S. Srikanth, "Strong interfacial polarization in ZnO decorated reduced-graphene oxide synthesized by molecular level mixing," *Phys. Chem. Chem. Phys.*, vol. 17, no. 26, pp. 17237–17245, 2015.
- [308] X. Sun, Z. Liu, K. Welsher, J. T. Robinson, A. Goodwin, S. Zaric, and H. Dai, "Nano-graphene oxide for cellular imaging and drug delivery," *Nano Research*, vol. 1, no. 3, pp. 203–212, Sep. 2008.
- [309] A. Teichler, J. Perelaer, and U. S. Schubert, "Inkjet printing of organic electronics – comparison of deposition techniques and state-of-the-art developments," *Journal of Materials Chemistry C*, vol. 1, no. 10, p. 1910, 2013.
- [310] D. B. Hall, P. Underhill, and J. M. Torkelson, "Spin coating of thin and ultrathin polymer films," *Polymer Engineering & Science*, vol. 38, no. 12, pp. 2039–2045, Dec. 1998.
- [311] K. Norrman, A. Ghanbari-Siahkali, and N. B. Larsen, "6 Studies of spin-coated polymer films," *Annual Reports Section "C" (Physical Chemistry)*, vol. 101, p. 174, 2005.
- [312] V. Gedela, S. K. Puttapati, C. Nagavolu, and V. V. S. S. Srikanth, "A unique solar radiation exfoliated reduced graphene oxide/polyaniline nanofibers composite electrode material for supercapacitors," *Materials Letters*, vol. 152, pp. 177–180, Aug. 2015.
- [313] H. Wang and Y. H. Hu, "Graphene as a counter electrode material for dye-sensitized solar cells," *Energy & Environmental Science*, vol. 5, no. 8, p. 8182, 2012.
- [314] C. Zhu, H. Min, F. Xu, J. Chen, H. Dong, L. Tong, Y. Zhu, and L. Sun, "Ultrafast electrochemical preparation of graphene/CoS nanosheet counter electrodes for efficient dye-sensitized solar cells," *RSC Advances*, vol. 5, no. 104, pp. 85822–85830, 2015.
- [315] J. Huo, J. Wu, M. Zheng, Y. Tu, and Z. Lan, "A transparent cobalt sulfide/reduced graphene oxide nanostructure counter electrode for high efficient dye-sensitized solar cells," *Electrochimica Acta*, vol. 187, pp. 210–217, Jan. 2016.
- [316] G. Li, R. Zhu, and Y. Yang, "Polymer solar cells," *Nature Photonics*, vol. 6, no. 3, pp. 153–161, Mar. 2012.
- [317] F. Liu, T. Tang, Q. Feng, M. Li, Y. Liu, N. Tang, W. Zhong, and Y. Du, "Tuning photoluminescence of reduced graphene oxide quantum dots from blue to purple," vol. 164307, pp. 1–5, 2014.
- [318] A. Mathkar, D. Tozier, P. Cox, P. Ong, C. Galande, K. Balakrishnan, A. Leela Mohana Reddy, and P. M. Ajayan, "Controlled, stepwise reduction and band gap manipulation of graphene oxide," *Journal of Physical Chemistry Letters*, vol. 3, no. 8, pp. 986–991, 2012.

## Appendix 1



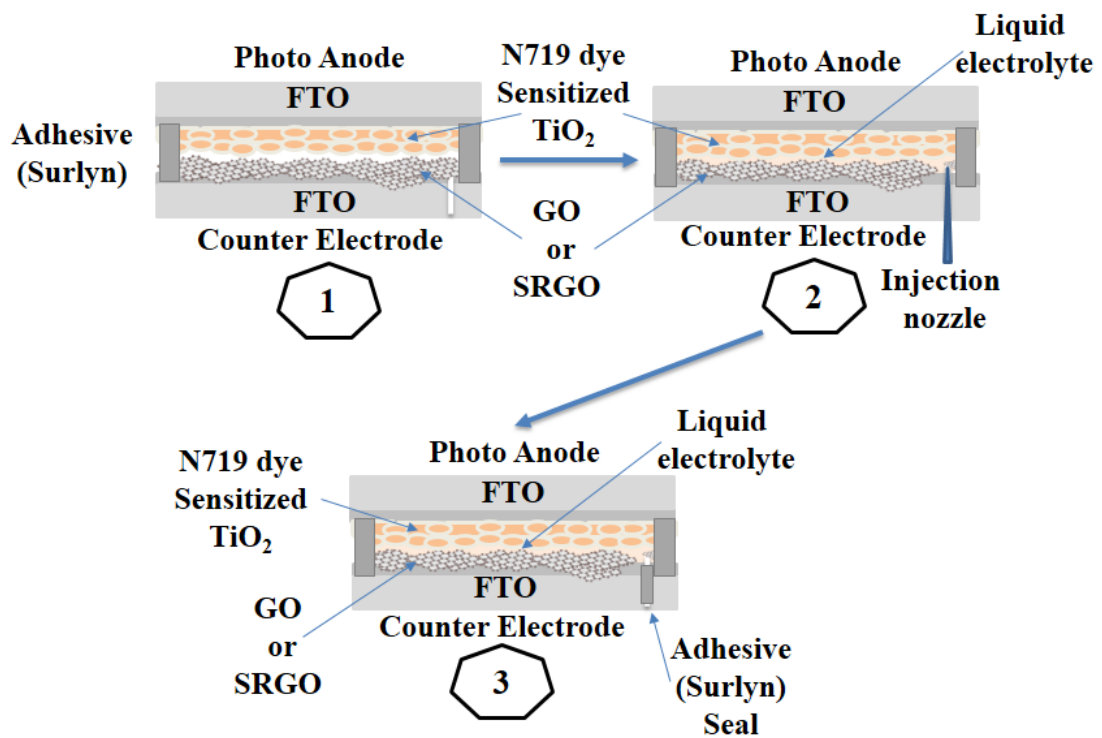
Schematic deposition procedure of photo anode for DSSC depicted in 7 steps: (2) Screen printing of 18 nm  $\text{TiO}_2$  colloidal paste on cleaned and pretreated FTO (1), (3) sintering at  $500^\circ\text{C}$  for 30 min, (5) screen printing of 200 nm  $\text{TiO}_2$  colloidal paste on cleaned and pretreated FTO (4), (6) further sintering at  $500^\circ\text{C}$  for 30 min to prepare FTO coated with  $\text{TiO}_2$  electrode and (7) staining the electrode in N719 dye.

## Appendix 2



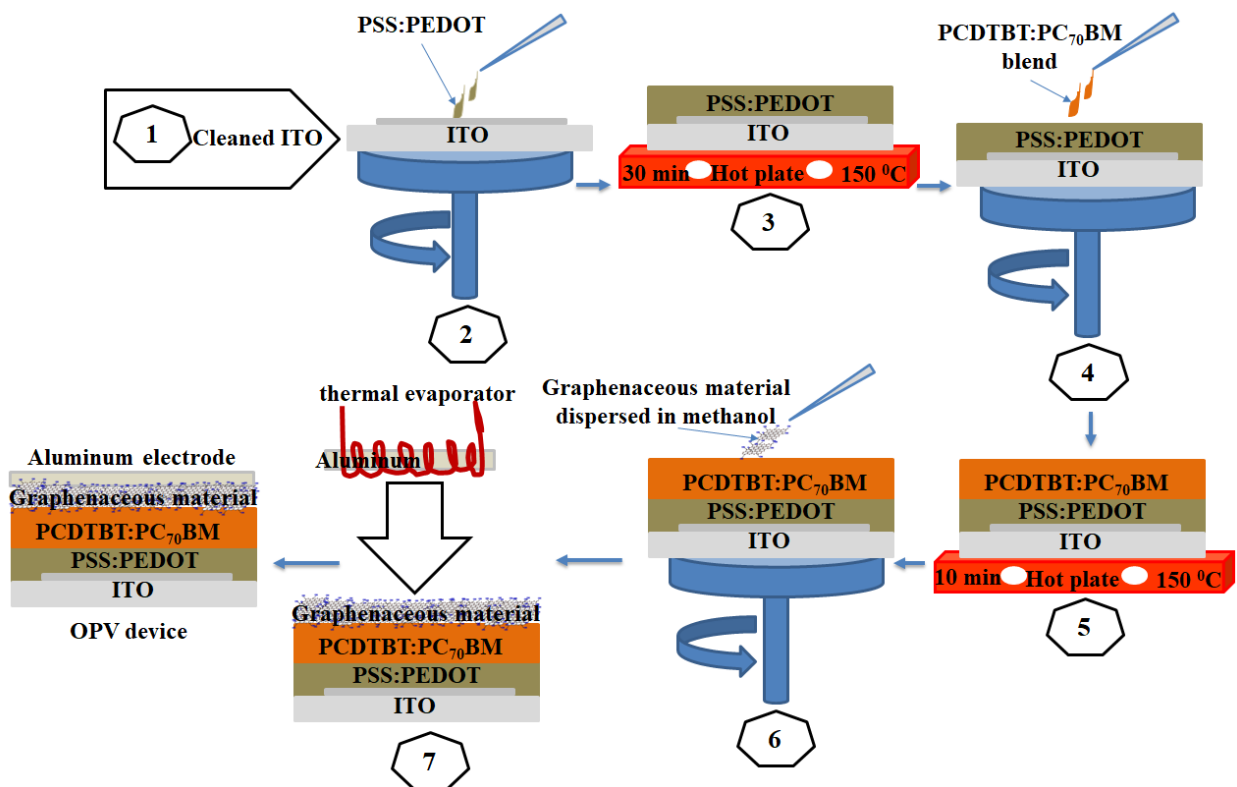
Schematic deposition procedure of counter electrode for DSSC depicted in 4 steps: (1) drilling 0.1 mm hole into the FTO glass plate, (2) washed and ultrasonicated FTO glass substrate with hole, (3) spray coating of GO or SRGO solution, and (4) heat treating the GO or SRGO coated FTO at 380 °C to prepare counter electrode.

## Appendix 3



Schematic showing fabrication of DSSC in 4 steps: (1) Assembling photo anode and counter electrode using thermal adhesive (Surlyn, Solaronix) as a spacer, (2) injection of electrolyte through the counter electrode's hole and (3) sealing counter electrode's hole with thermal adhesive to finally produce DSSC.

## Appendix 4



Schematic showing fabrication of OPV in 7 steps: (2) PEDOT:PSS deposition on cleaned substrate (1) on spin coater, (3) annealing, (4) PCDTBT:PC<sub>70</sub>BM blend deposition, (5) annealing for BHJ formation, (6) Graphenaceous solution deposition on BHJ as ETL and (7) vacuum thermal evaporation of Al as electrode to complete the device.